Numerical Radiation Hydrodynamics of Protostellar Collapse: An Application to the Formation of Brown Dwarfs

(重力崩壊と原始星形成過程の数値的輻射流体力学：褐色矮星形成過程への応用)

Torsten Stamer

Laboratory for Theoretical Astronomy & Astrophysics (TA-Lab)
Nagoya University
Furō-chō, Chikusa-ku, 464-8602 Nagoya, Japan

July 5, 2018

Abstract

Our galaxy is continuously forming new stars. The nuclear fusion processes within those stars create elements heavier than hydrogen and helium, many of which are returned to the interstellar medium once the star ends its life as a red giant or a supernova. New generations of stars then form with different levels of heavy elements, and in this way stars drive the evolution of the galaxy, and ultimately the universe as a whole, over cosmological timescales. Therefore, a profound understanding of stars and their formation is essential for the field of astrophysics as a whole.

Star formation is a complex process which involves physical scales ranging from the size of whole galaxies to that of interstellar dust particles. The focus of this thesis is the process by which an individual star forms from the gravitational collapse of a cloud of gas, i.e. a molecular cloud core. We are especially interested in the formation of very low-mass objects such as brown dwarfs and sub-brown dwarfs, since this mass regime has so far been underexplored and presents a number of scientific questions and challenges.

In order to investigate this so-called "protostellar collapse", we first develop a new numerical scheme for solving the radiative transfer equation in a spherically symmetric system. This scheme does not rely on any kind of diffusion approximation and it is accurate for optically thin, thick, and intermediate systems. We then perform various test calculations with this method, including a simplified protostellar collapse simulation.

In the next step, we apply our scheme to the numerical simulation of brown dwarf formation by turbulent compression. In this scenario, brown dwarfs are formed as a result of an external turbulent pressure acting on the molecular cloud core, which would otherwise be stable to gravitational collapse. We investigate the possibility of this mechanism and the necessary conditions for it to occur.

Finally, we expand our method to include a more realistic equation of state that allows us to model the whole collapse process from the initial cloud core to the formation of the protostar. We perform a number of simulations mainly of the brown dwarf mass regime and discuss the results.

Contents

Chapter 1

Introduction

This chapter provides a general introduction to the physics of star formation, from molecular clouds to the formation of a protostar. The process of protostellar collapse and the formation of brown dwarfs are discussed in some more detail.

1.1 Molecular Clouds and Filaments

Stars form in molecular clouds - regions of the interstellar medium which are very dense ($> 10^2/\mathrm{cm}^3$) and cold (10 K), allowing for the hydrogen gas of which they consist to be present in molecular form (H_2). Molecular clouds can have sizes of tens to hundreds of light years, and contain hundreds of thousands of solar masses. Within these clouds, there exist regions of especially high density, usually called "prestellar cores" (or "protostellar cores" if a protostar is present within). It is believed that star formation occurs where such cloud cores become massive enough to collapse under their own gravity in a process called "protostellar collapse", which we shall describe in section 1.2 and which is the main focus of this work.

Before we consider cloud core collapse, however, we must first discuss how these cores form in the first place. It has been firmly established by the *Herschel* survey (e.g. André et al. (2014)) that the internal structure of molecular clouds is dominated by filaments, and that the majority of prestellar and protostellar cores in star-forming regions are found within them (see Figure 1.1 for an example). Filaments are elongated regions of higher gas density, with a characteristic width of 0.1 pc and lengths of a few to tens of parsec. Their formation is believed to be the result of MHD turbulence within the cloud (Padoan et al. (2001); Pudritz & Kevlahan (2013)), of which there are many different sources in the interstellar medium, among them supernovae, galactic spiral shocks, or gravitational and other instabilities. Simulations of supersonic turbulence consistently show the formation of filaments, but the details are still under investigation. For example, Padoan et al. (2001) focuses on filament formation due to colliding sheets, while Hennebelle (2013) concentrates on the importance of shear. In any case, filaments are created even without the inclusion of gravity, but once they have formed, gravity becomes the decisive factor: Theoretical consideration of an isothermal, self-gravitating cylinder (Inutsuka & Miyama (1992, 1997)) shows that filaments are gravitationally stable only if their line mass (i.e. mass per length) does not exceed a certain critical value $M_{\mathrm{line,crit}} \approx 16 M_\odot \mathrm{pc}^{-1} \times (T_{\mathrm{gas}}/10\mathrm{K})$. It is evident from Figure 1.1 that pre- and protostellar cores are found almost exclusively in regions where this stability criterion is violated. Intersections between different filaments may create the regions most conducive to star formation, and especially star cluster formation, due to localized higher density (Myers (2009, 2011); Schneider et al. (2012)).

Qualitatively, we may therefore state that star formation occurs in regions of overdense, radially collapsing filaments. More quantitatively, any star formation theory must predict the

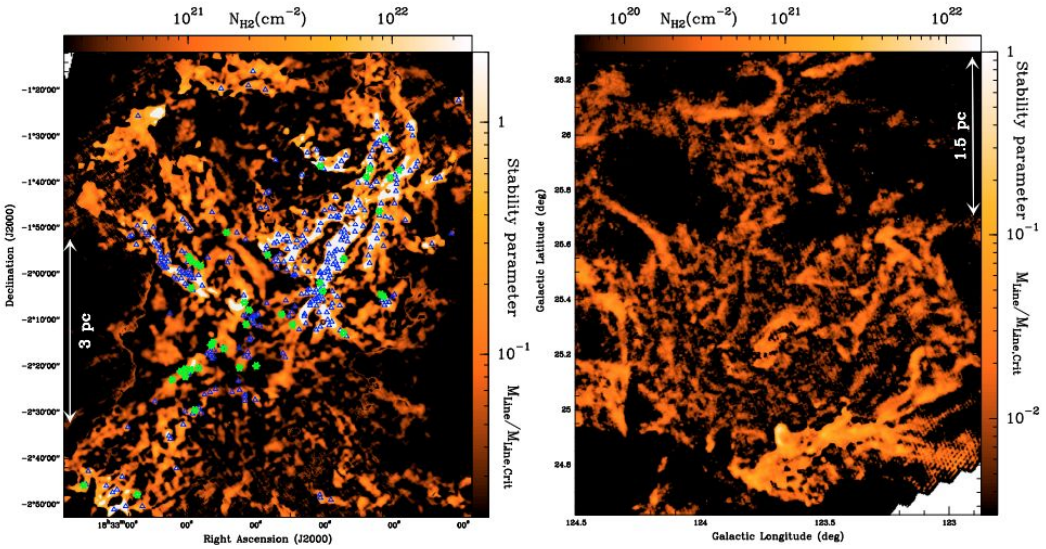

Figure 1.1: Column density maps of two regions in Aquila (left panel) and Polaris (right panel) (from André et al. (2010)). The color scale shows the corresponding line mass in units of the critical line mass derived by Inutsuka & Miyama (1997), with supercritical regions highlighted in white. There is good agreement between these supercritical regions and the observation of candidate protostars (green stars) and prestellar cores (blue triangles) identified by Bontemps et al. (2010) and Könyves et al. (2010), respectively. There are no supercritical regions in Polaris, suggesting that this region is stable and not forming any stars.

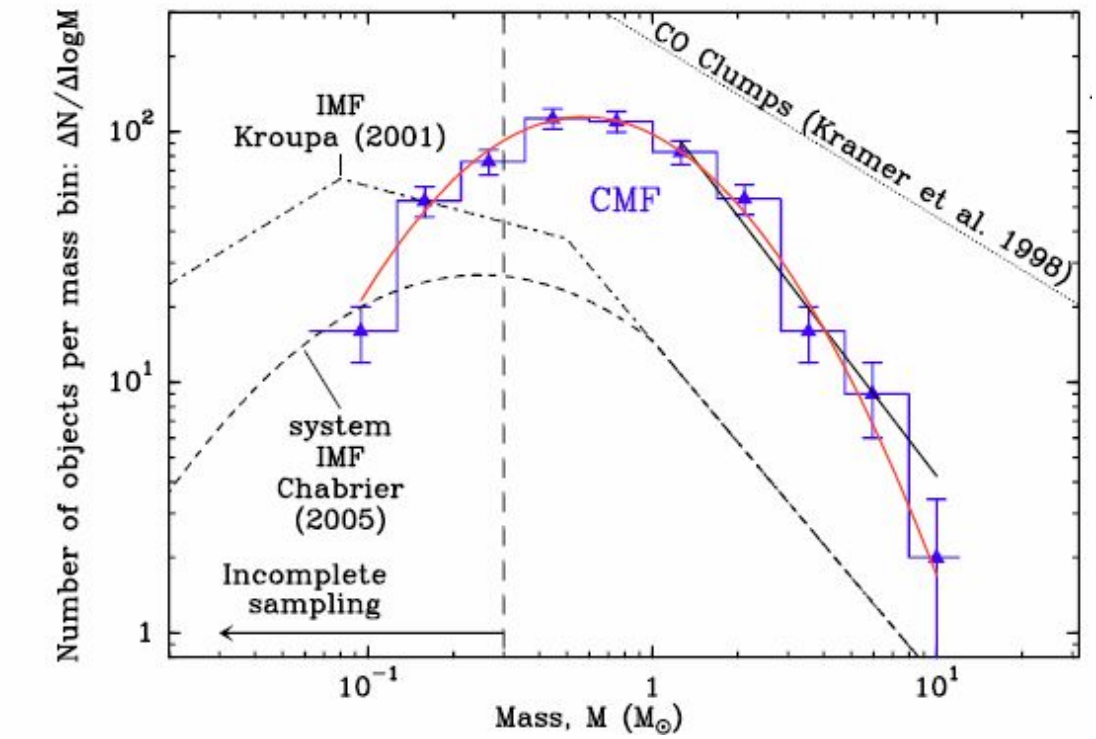

Figure 1.2: Core mass function (blue histogram) from the observation of Aquila by André et al. (2010). The solid red and black curves are fits using a lognormal distribution and a power law, respectively. The IMFs by Kroupa (2001) (for single stars) and by Chabrier (2005) (star systems) and the typical mass function of CO clumps (Kramer et al. (1998)) are included for comparison.

number of cores of a certain mass, that is to say it must include a mechanism to produce the core mass function (CMF) shown in Figure 1.2. Inutsuka & Miyama (1992, 1997) studied the stability of self-gravitating cylindrical structures and found that filaments are unstable to longitudinal perturbations, which grow and cause the filament to fragment into a number of prestellar cores. Inutsuka (2001) further developed a formalism to predict the resulting CMF from the power spectrum of the initial perturbations, and recent *Herschel* observations of nearby filaments (Roy et al. (2015)) find a power spectrum slope of -1.6 ± 0.3, which is very close to the value of -1.5 required by Inutsuka (2001) to produce a Saltpeter-like CMF.

1.2 Protostellar Collapse

Once a prestellar core has formed, the next step on the way to creating a star is for this core to collapse. Under isothermal conditions, the only requirement for such a collapse is that the core's mass should be larger than its thermal Jeans mass. In reality, however, after sufficient compression the system ceases to be isothermal and instead behaves closer to adiabatic. We must therefore consider the importance of thermodynamics: Is the increase in pressure strong enough to halt the gravitational collapse?

For simplicity, let us model the cloud core as a homogeneous sphere with total mass M, radius R and density ρ. We express the pressure using a polytropic equation of state, i.e. $P \propto \rho^{\gamma_{\text{eff}}}$, where γ_{eff} is the effective ratio of specific heats. The gravitational and pressure forces are then given by:

$$F_{\text{G}} = \frac{GM}{R^2} \tag{1.1}$$

$$F_{\text{P}} = \frac{1}{\rho}\frac{\partial P}{\partial R} \propto \frac{\rho^{\gamma_{\text{eff}}-1}}{R} \tag{1.2}$$

For a homologous collapse, $\rho \propto R^{-3}$, so the relationship between pressure and radius is $F_{\text{P}} \propto R^{2-3\gamma_{\text{eff}}}$. The ratio between the two forces then scales as:

$$\frac{F_{\text{P}}}{F_{\text{G}}} \propto R^{4-3\gamma_{\text{eff}}} \tag{1.3}$$

It follows that there is a critical value of γ_{eff}, namely 4/3. If γ_{eff} is larger than this value, pressure becomes stronger relative to gravity as the radius decreases, which inevitably leads to a stabilization and stop of the collapse. On the other hand, if it is smaller than this value, gravity becomes ever more dominant over pressure as the radius decreases, leading to an accelerating collapse.

We describe the evolution (summarized in Figure 1.3): Initially, the cloud core is essentially isothermal ($\gamma_{\text{eff}} = 1$), since it is optically thin so that any heat gained through compression is efficiently radiated away and the gas is kept at the temperature of the surrounding molecular cloud, which is typically around 10 K. The temperature actually drops slightly since the core becomes opaque to the high-frequency heating radiation of background stars while the low-frequency cooling radiation is still able to escape, an effect which we will discuss further in sections 5.5.1 and 5.5.5.

As the collapse progresses, compressional heating becomes ever stronger and the efficiency of the radiative cooling diminishes. Once the heating overtakes the cooling, the system's behavior transitions from isothermal to adiabatic. γ_{eff} then becomes 5/3 (for temperatures below a few hundred Kelvin) and 7/5 above that. The difference is due to the fact that for low temperatures, the rotational degree of freedom of the hydrogen molecule is "frozen out", preventing it from contributing to the heat capacity. In any case, both of these values are larger than the critical

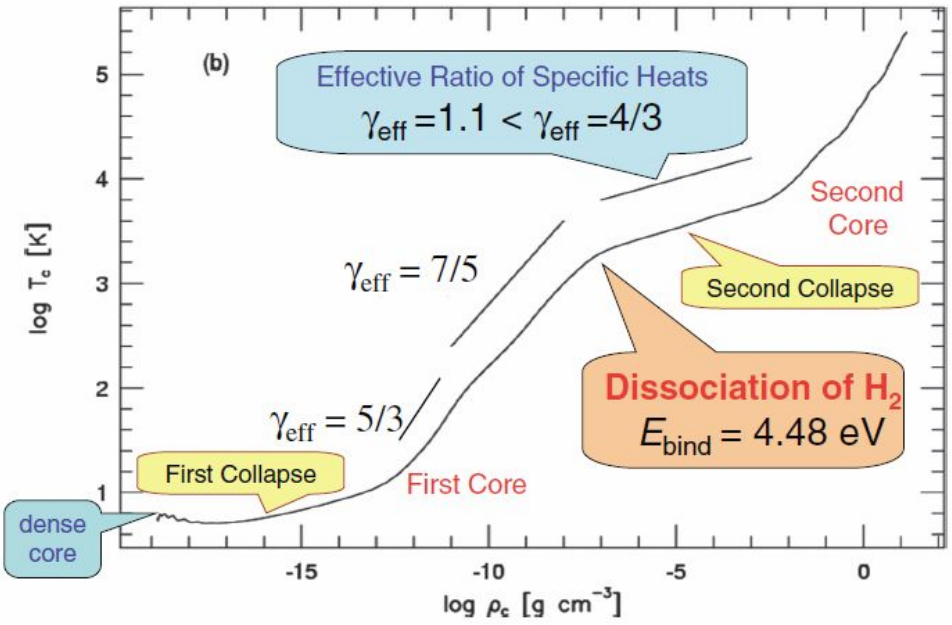

Figure 1.3: Evolution of temperature and density at the center of a collapsing cloud core, from Inutsuka (2012). An initial isothermal phase is followed by adiabatic contraction until the formation of the first hydrostatic core. The dissociation of hydrogen molecules triggers the second collapse, which results in the formation of the second core (protostar).

value of 4/3, which means that the pressure force ultimately stops the gravitational contraction and a hydrostatic object with a typical size of a few AU, the so-called "first hydrostatic core", is formed. Its surface is marked by a shock in which the infalling material is decelerated. At this point, roughly one free-fall time has passed, which in the case of a solar-mass cloud core corresponds to about 10^5 years. The first core then continues to increase in mass and temperature as it accretes material from the surrounding gas envelope. Once the temperature reaches $\approx 10^3$ K, hydrogen molecules begin to dissociate. This is a strong cooling effect, which acts to reduce the effective ratio of specific heats to about 1.1 and thereby triggers a second collapse. Because of this, the first core is generally thought to exist for no more than a few thousand years, although theoretical considerations and the surprisingly large number of candidate objects observed suggest that it may live much longer in some cases. We will discuss this question in detail in section 5.5.3. The second collapse continues until all the hydrogen has been dissociated, so that $\gamma_{\rm eff}$ increases again to 5/3 and a second hydrostatic core forms, which is also known as a protostar. The collapse phase ends here and the system's pre-main sequence (PMS) evolution begins.

The theoretical and numerical investigation of a spherical collapse such as we described above is the main focus of our work. We will discuss the numerical scheme and more detailed physics (opacities, equation of state...) in detail in the introductions to sections 4 and 5.

The above description of protostellar collapse is considerably simplified since it assumes spherical symmetry and ignores magnetic fields and rotation. We will continue to make these assumptions throughout this work, since we focus on 1-D radiation-hydrodynamical simulations.

1.3 Pre-Main Sequence Evolution

Once a protostar has formed, the system evolves on a much slower timescale (about 10^7 years compared to the free fall time's 10^5). During the PMS phase, the gas envelope surrounding the protostar forms into a circumstellar disk of gas and dust in which planet formation can take place. At the same time, the protostar slowly continues to increase in mass and temperature

as it undergoes Kelvin-Helmholtz-contraction and accretes material from the disk. In the HR diagram, it moves along the Hayashi or Henyey track during this time (Figure 1.4). However, this simple picture of formation and contraction is now being questioned, and there appears to be a larger variety of PMS evolutionary tracks than was assumed previously. For example, Kunitomo et al. (2012) found that PMS evolution depends strongly on the efficiency of mass accretion (i.e. how much of the gravitational energy of the infalling material is transformed into internal energy), as well as on the deuterium mass mixing ratio and on the initial entropy/radius of the protostar. The latter is of course determined by the details of the collapse process described in the preceding section, which is an important motivation for our work. Generally speaking, the results of protostellar collapse simulations such as ours are important to determine the initial conditions for work dealing with the following PMS phase.

PMS evolution ends once the central temperature exceeds 10^7 K and nuclear fusion sets in, so that the protostar becomes a fully developed main sequence star (except in the case of brown dwarfs - see below). The circumstellar disk dissipates, typically after about 10^7 years, due to a combination of accreting onto the star and being blown away by its radiation pressure.

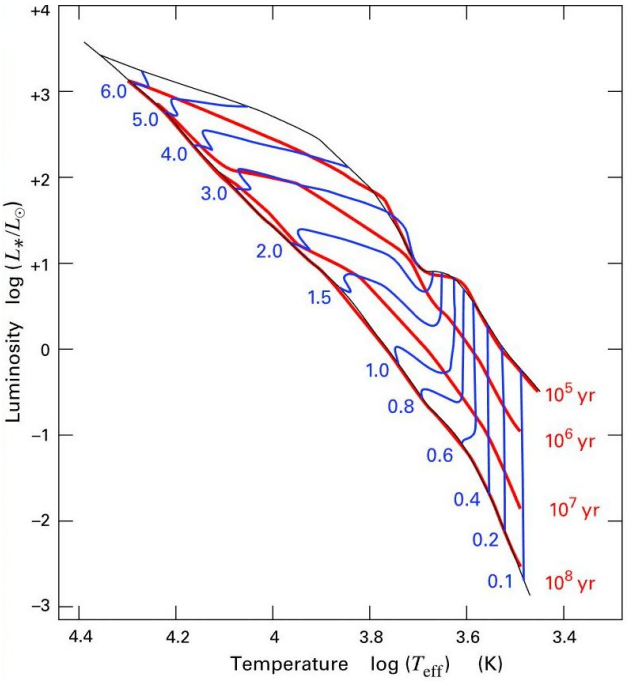

Figure 1.4: Pre-main sequence evolutionary tracks in the HR diagram, from the calculations of Stahler & Palla (2008). The numbers in blue show the object's mass in units of $M_\odot$.

1.4 Theory of Brown Dwarf Formation

We have outlined the star formation process as it applies to solar type stars. However, in this work, our main focus will be on brown dwarfs. These are substellar objects with masses between about 1 and 8 % of the solar mass. They are similar to very low-mass stars in many ways, but the defining difference is that brown dwarfs have such low mass that their core temperature never becomes hot enough to sustain hydrogen fusion (although deuterium fusion may occur in some cases). This means that brown dwarfs lack an internal energy source; after their formation they simply cool down over time, so unlike in the case of stars there is a direct relationship between age and temperature (Figure 1.5).

Observations suggests that the number of brown dwarfs is comparable to that of low-mass stars, but their formation has puzzled researchers for some time. The problem is easily understood by considering the Jeans stability criterion: It is believed that star formation takes place

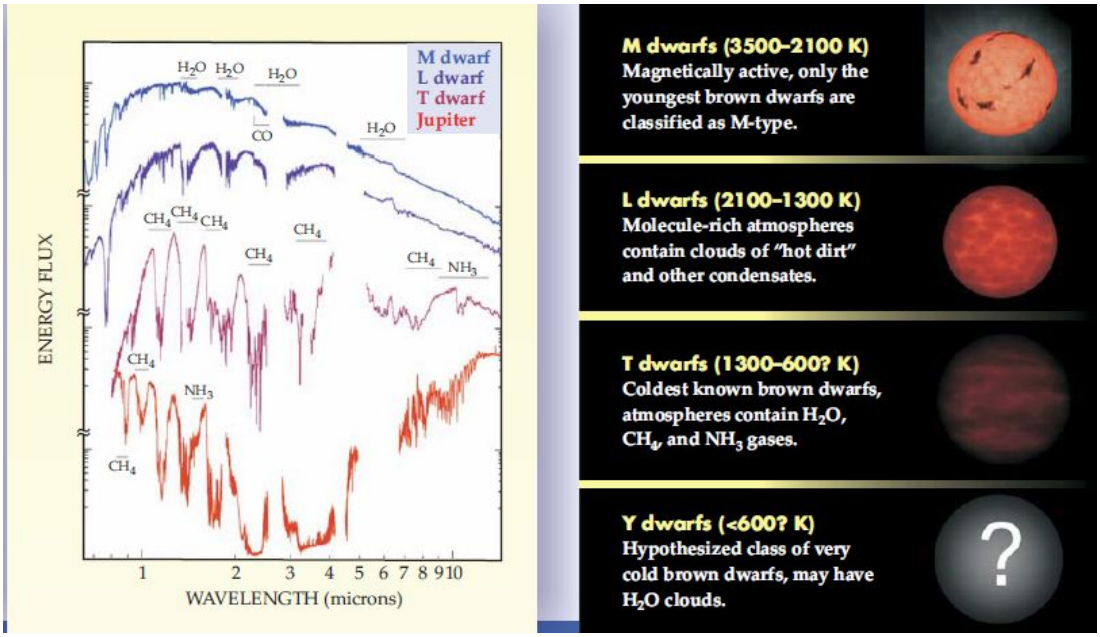

Figure 1.5: Spectral classes of brown dwarfs, from Burgasser (2008). Since brown dwarfs have no internal heating source, the sequence from hotter to colder objects corresponds to an evolutionary sequence from younger to older.

when a molecular cloud core exceeds its Jeans mass $M_{\rm J} = c_{\rm s}^3 G^{-3/2} \rho^{-1/2}$. Given the typical temperature of a molecular cloud (10 K), and assuming that the mass of the star that is formed ($M_\star$) is similar to the Jeans mass, we can calculate the density that the original cloud core must have in order to be unstable:

$$\rho = \left(\frac{c_{\rm s}^3 G^{-3/2}}{M_\star}\right)^2 \tag{1.4}$$

For $M_\star = M_\odot$, this evaluates to roughly $10^4 {\rm cm}^{-3}$, which is in line with typical observations of high-density star-forming regions. But the required number density increases to $10^6 {\rm cm}^{-3}$ for $M_\star = 0.1 M_\odot$ (slightly above the brown dwarf/star boundary) and $10^8 {\rm cm}^{-3}$ for $M_\star = 0.01 M_\odot$ (a low mass brown dwarf). This far exceeds the observed densities in molecular clouds. Hence the question arises: Which mechanism is responsible for creating such extremely high density regions as are necessary for brown dwarf formation? Broadly speaking, there are two possibilities:

1. The same mechanism that creates "normal" prestellar cores also produces pre-brown dwarf cores.

2. One or more other mechanisms are important, and possibly even dominant, in brown dwarf formation.

The core mass function and initial mass function in the very low-mass regime are poorly known (see Figures 1.2 and 1.6), so it is still unclear whether the CMF and IMF are universal (i.e. apply to all mass ranges from brown dwarfs to massive stars). The former case would imply that brown dwarf formation is simply a scaled down version of low-mass star formation; the latter would imply that alternative mechanisms are at play.

A number of such alternative scenarios have been proposed to explain brown dwarf formation. One possibility is the gravitational fragmentation of protostellar disks (Stamatellos, Hubber & Whitworth (2007); Stamatellos & Whitworth (2008)). While it is known that disks can become unstable (and this mechanism, alongside the core accretion model, is often invoked for giant planet formation), it is unclear whether sufficiently massive accretion disks can commonly form. Given the comparable number of brown dwarfs and low-mass stars, on average

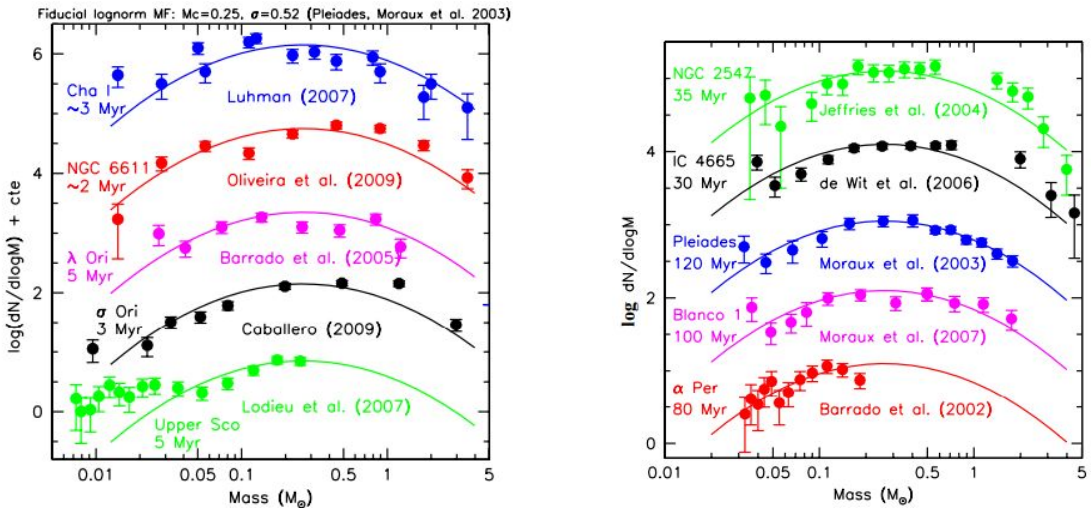

Figure 1.6: Measurements of the IMF in various star clusters, offset for clarity (Jeffries (2012)). The solid lines correspond to the log-normal function that best fits the Pleiades. Overall agreement is quite good, but there are differences and a general lack of data in the very low mass regime.

about one brown dwarf should form in the disk of every low-mass star, which at this point seems very unlikely.

Another possibility is so-called "competitive accretion and ejection", investigated by e.g. Reipurth & Clarke (2001); Bate (2008): In this scenario, a higher mass prestellar core results in the formation of multiple protostars. Gravitational interactions between these can then cause some to be ejected from the parent cloud, so that they lose their accretion reservoir and can no longer grow in mass. The main problem is that this scenario predicts a large velocity dispersion for brown dwarfs, but so far observations such as those by Joergens (2006) and Kurosawa, Harries & Littlefair (2006) suggest no significant difference between stars and brown dwarfs in this regard.

Furthermore, Whitworth & Zinnecker (2004) have suggested that a brown dwarf can be created when a core that is originally more massive has part of its material eroded due to ionizing radiation from nearby OB stars (photo-erosion). However, there are no observations showing an excess of brown dwarfs in the vicinity of massive stars, and brown dwarf formation is certainly possible without any massive stars nearby, so this mechanism does not appear to be dominant either.

In contrast to the filament paradigm we described in section 1.1, which is dominated by gravity, in works like Padoan et al. (2001) and Tilley & Pudritz (2004) the formation of prestellar cores - pre-brown dwarfs included - is described as a process dominated by turbulence. In this paradigm, stars form wherever the collision of turbulent flows creates a sufficiently dense (i.e. Jeans-unstable) condensation. However, these calculations are isothermal, so they do not consider the stabilizing effect of the temperature/pressure increase in a collapsing core. This is especially problematic for very low-mass (brown dwarf) cores, which are inherently more difficult to collapse due to the extreme densities required. Lomax (2016) used SPH calculations of colliding flows to simulate brown dwarf formation in this way, and they found that an unrealistically high degree of convergence of the initial flow field is required in order to create a gravitationally bound object (see Figure 1.7).

In chapter 4 of this thesis, we adopt a different model to tackle a similar problem, using the radiative transfer scheme developed in section 2. Our approach does not require any assumption about the flow field, and it allows us to estimate the scale of turbulence necessary to form brown dwarfs by turbulent compression. On the other hand, in chapter 5 we investigate the properties of brown dwarfs formed from initial conditions that are unstable even without any external compression, as we would expect from the filament paradigm.

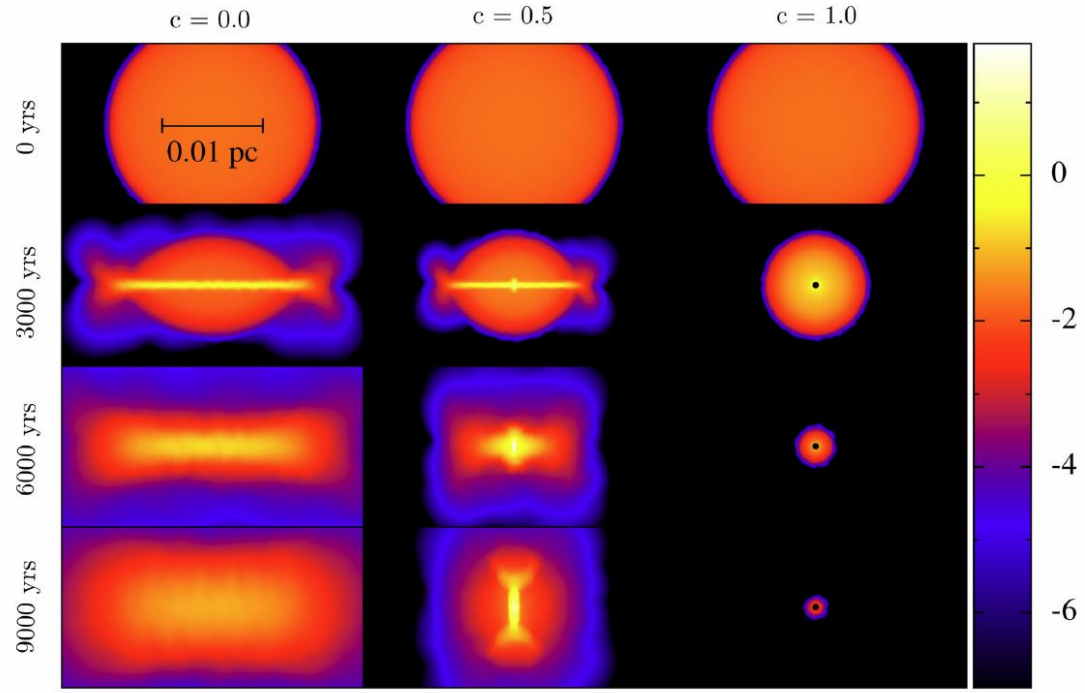

Figure 1.7: Colliding flow simulations by Lomax (2016). The color shows column density, and different points in time are shown along the vertical. The three columns correspond to three different calculations. They all have total mass $0.02 M_\odot$ and initial radius 0.01pc, and the initial flow field is given by $\boldsymbol{v} = -v_0 \frac{c\hat{r}+(1-c)\hat{z}}{|c\hat{r}+(1-c)\hat{z}|}$, with $v_0 = 2\mathrm{kms}^{-1}$ and $\hat{r}$ and $\hat{z}$ the unit position vector and unit vector in z-direction. The convergence parameter c controls how strongly the flow converges radially towards the center. Therefore, in the left column ($c = 0$), the initial flows are antiparallel in z-direction and collide in the midplane; in the right column ($c = 1$), they converge perfectly. Only in this case a bound object forms, but in real molecular clouds there is no reason to assume that flows should commonly be so strongly convergent.

As a final note, it should be mentioned that these various theories for brown dwarf formation are not mutually exclusive. It is likely that all of them can and do occur in nature, but it is unclear how important they are relative to each other. For instance, in a study of brown dwarfs orbiting solar-type stars, Ma & Ge (2014) find evidence of two distinct populations (see Figure 1.8). Based on different eccentricity distributions, they suggest that objects below $\approx 43 M_\mathrm{J}$ in their sample have mostly formed from disk instabilities, making them similar to giant planets. On the other hand, the heavier objects are the result of molecular cloud core collapse, meaning these systems are better characterized as binaries. More detailed observations, as well as numerical simulations, are necessary to better estimate the contribution of the various possible formation channels.

1.5 Thesis Structure

This thesis is structured in the following way: In chapter 2, we develop a new radiative transfer scheme for spherically symmetric systems. We perform various test calculations for our method in chapter 3 and also mention some ideas for possible future improvements. We apply our method to an actual physical problem - the formation of brown dwarfs - in chapter 4. At that point, we still employ several simplifications and only follow the evolution until the formation of the first core. This is followed in chapter 5 by calculations with an expanded version of our program which includes the second collapse, and we analyze the results of collapse calculations in the brown dwarf regime. Finally, a summary of our work and future prospects are given in chapter 6.

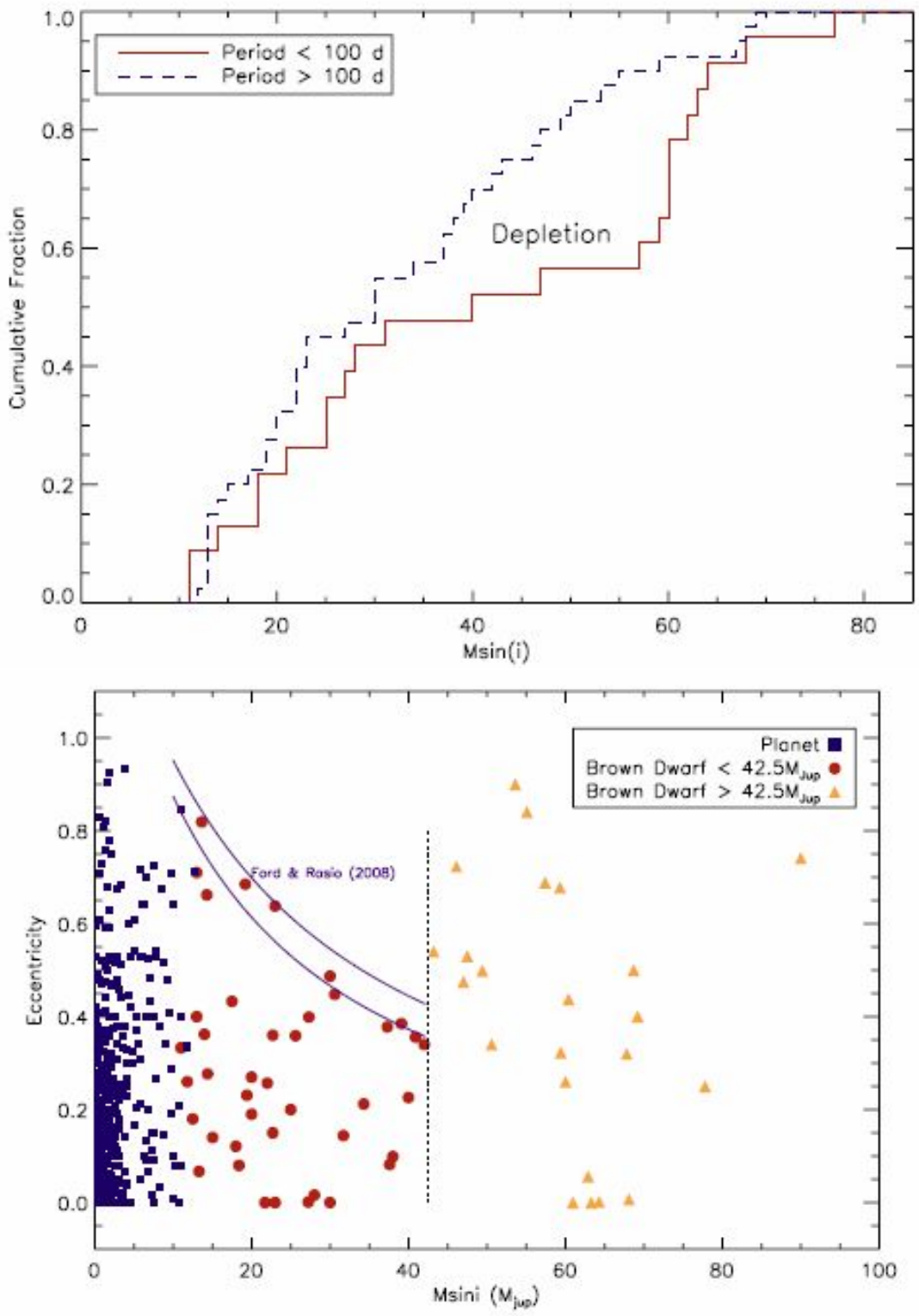

Figure 1.8: Evidence for two distinct populations of brown dwarfs orbiting solar-type stars, from Ma & Ge (2014).
Upper panel: The distribution shows a paucity of objects with a period of less than 100 days in the mass range between about 40 and 60 $M_{\rm J}$, suggesting two different populations.
Lower panel: The eccentricity distribution of brown dwarfs below $\approx 43 M_{\rm J}$ is similar to that of known exoplanets, showing a decreasing trend with mass. On the other hand, heavier objects exhibit no such trend and are more suggestive of binaries. The purple lines show the theoretical prediction for the eccentricity distribution resulting from scattering with a 20 (lower line) and 25 (upper line) $M_{\rm J}$ object (Ford & Rasio (2008)).

Chapter 2

Method Development

This chapter is dedicated to the development of our radiative transfer scheme. We begin with a brief introduction to radiative transfer in general and protostellar collapse calculations in particular (section 2.1). In section 2.2, we derive the equations on which our method is based, followed by a description of the numerical implementation.

The contents of chapters 2 and 3 have been previously compiled into a paper (Stamer & Inutsuka (2018)), which has been accepted for publication by *The Astronomical Journal* and is also available on arXiv.

2.1 Method Introduction

2.1.1 On Radiative Transfer and Protostellar Collapse Simulations

Theoretical investigations of many astrophysical problems require an accurate treatment of radiative transfer. Since analytic solutions of the transfer equation are generally unavailable except in trivial systems, numerical methods are employed. However, the complexity of the problem typically means that a realistic treatment is computationally expensive. One example of such an expensive problem is the simulation of protostellar collapse, that is the process by which a molecular cloud core contracts under its own gravity to form a star, investigated in a seminal paper by Larson (1969) and by others such as Winkler & Newman (1980), Masunaga, Miyama, & Inutsuka (1998) and Vaytet & Haugbølle (2017).

Numerical simulations of protostellar collapse are challenging, which is in part due to the extremely wide range of size and density: When forming a solar-type star, typical values for the initial cloud core are 10^4AU and $10^{-19}\mathrm{g\,cm^{-3}}$, while the protostar is 10^{-3}AU and $10^{-1}\mathrm{g\,cm^{-3}}$. Radiative transfer presents another difficulty: While the early, isothermal phase can be approximated by simple optically thin cooling, and the optically thick regions in the later stage by radiative diffusion, neither of these approximations is valid in the optically intermediate region near the photosphere. However, this is the most important region for the exchange with the outer medium, which determines the temperature structure and ultimately the entropy of the protostar. The latter determines the initial location in the HR-diagram and the subsequent evolution.

In recent years, numerical simulations have become more and more sophisticated. The number of physical processes included keeps increasing, among them magnetic field effects (Tomisaka (2002); Machida et al. (2006); Commerçon et al. (2010); Federrath (2015)), protoplanetary disk formation (Inutsuka et. al (2010); Stamatellos & Whitworth (2008); Machida et al. (2011); Tomida, Okuzumi & Machida (2015); Seifried et al. (2016); González et al. (2015); Nordlund et al. (2014)), chemical evolution (Visser, Bergin, & Jørgensen (2015); Dzyurkevich et al. (2016); Hincelin et al. (2016)), and non-ideal MHD (Tsukamoto et al.

(2015a,b); Wurster, Price, & Bate (2016); Masson et al. (2016)). There are now also synthetic observations comparable with actual data (Commerçon et al. (2012); Frimann, Jørgensen, & Haugbølle (2016); Seifried et al. (2016)).

At the same time, much more simplified, spherically symmetric RHD simulations such as those by Masunaga, Miyama, & Inutsuka (1998); Masunaga & Inutsuka (2000) and, more recently, Vaytet et al. (2011, 2012, 2013); Vaytet & Haugbølle (2017), are still valuable: This one-dimensional modeling is still the only method to describe the evolution of the entire process of protostellar collapse, since multi-dimensional modeling has to mask the central region that requires extremely short timesteps. In this context, we aim to develop a radiative hydrodynamics scheme for spherical systems that is both fast and accurate, so that it can be used for a detailed exploration of the parameter space to investigate the effects of the initial conditions on properties such as protostellar mass, radius, and entropy. Note also that the present method can be combined with multi-dimensional modeling. In addition, even though collapse simulations are the primary motivation for this work, the method is not limited to this and may well be used in other systems that can be approximated as spherical.

Radiative transfer is often treated using either the flux-limited diffusion approximation, for example in works such as Bodenheimer et al. (1990) and Yorke, Bodenheimer & Laughlin (1993), or a method based on solving the moment equations of radiation (Castor (1972); Buchler (1979)). The latter requires a closure relation, which commonly appears in the form of the Eddington approximation, which assumes that the Eddington factor f, the ratio between the second and the zeroth moment of radiation, is equal to 1/3. This is exactly correct only in the case of isotropic radiation. An improvement upon this is the variable Eddington factor method (Tscharnuter & Winkler (1979)), in which the Eddington factor is no longer constant, but instead is calculated depending on the degree of anisotropy of the radiation field. Details of the numerical implementation can be found for instance in Mihalas & Mihalas (1984) or Stone, Mihalas & Norman (1992), the basis for the "ZEUS" RHD-code.

Both the diffusion and Eddington approximation are very fast, but also somewhat crude, since they are only exact in optically thin / isotropic regions. On the other hand, the variable Eddington factor method is very accurate, but requires considerable computational effort. In this work, we develop a method that aims to combine the advantages of both. Our approach is different in the sense that it uses neither the diffusion approximation nor the moment equations. Instead, it is based on the radiative exchange between pairs of spherically symmetric shells. It does have some resemblance to ray-tracing schemes, especially in the case of the numerical angle integration discussed in section 2.3.3.

2.1.2 Aims

We develop a method to solve the radiation transport in a spherically symmetric fluid system. The aim is to calculate the rate of energy gain or loss due to radiation at any radius, i.e. $dU/dt\,(r)$, where U is the specific internal energy of the fluid. Therefore the unit of this "radiation term", as we shall call it from now on, is power per mass.

Ultimately, our method is intended to couple to a hydrodynamic simulation by including the radiation term in the hydrodynamic energy equation. To first order, this can be done by subdividing the system into a finite number of shells, calculating the radiation term at some radius representative of each shell (such as the shell center), and assuming that it does not vary over the shell. For higher order calculations, one may interpolate the value of the radiation term between neighboring shells.

The radiation term is the sum of radiative heating and cooling. The latter is trivial even in a 3-D system since it depends only on the local values of density, opacity and temperature at position $\boldsymbol{r}$. But heating is far more complicated, as it depends on the local radiation field,

which in turn is determined by the distribution of these variables across the entire system.

2.2 Derivation of the basic equations

2.2.1 General derivation

The monochromatic radiation transfer equation in three dimensions is

$$\frac{1}{c}\frac{dI_\nu}{dt} + \boldsymbol{n}\cdot\nabla I_\nu = \kappa_\nu\rho\left(S_\nu - I_\nu\right), \tag{2.1}$$

where I_ν, κ_ν and S_ν are the intensity, opacity and source function at frequency ν. In the following, we will leave out the index ν for convenience.

Equation (2.1) combines the effects of emission and absorption of radiation by the material. We shall neglect the explicitly time dependent term dI_ν/dt throughout this work. This is equivalent to assuming that the radiation field *instantaneously* adjusts to any changes in the hydrodynamic variables. This assumption is valid as long as the time for light to cross the system is much shorter than the time for the hydrodynamic variables to change significantly, which is the case in most astrophysical systems.

With the above assumption, the solution is

$$\begin{aligned} I\left(\boldsymbol{r},\boldsymbol{n}\right) = &\int_0^{D_\mathrm{B}} \kappa\left(\boldsymbol{r}+\boldsymbol{n}D\right)\rho\left(\boldsymbol{r}+\boldsymbol{n}D\right)S\left(\boldsymbol{r}+\boldsymbol{n}D\right)e^{-\tau\left(\boldsymbol{r},\boldsymbol{r}+\boldsymbol{n}D\right)}dD \\ &+ S_\mathrm{O}e^{-\tau_\mathrm{B}}, \end{aligned} \tag{2.2}$$

where $\tau\left(\boldsymbol{r},\boldsymbol{r}+\boldsymbol{n}D\right)$ is the optical depth between positions $\boldsymbol{r}$ and $\boldsymbol{r}+\boldsymbol{n}D$, while D_B and τ_B refer to the distance and optical depth between $\boldsymbol{r}$ and the outer boundary of the system in direction $\boldsymbol{n}$. The first term represents radiation emitted by other points within the system, while the second term represents radiation coming from outside. The latter's intensity is determined by S_O, the source function of the external radiation, which must be supplied as a boundary condition.

Equation (2.2) determines the direction-dependent intensity. The integral over all directions gives us the radiation energy density:

$$\epsilon\left(\boldsymbol{r}\right) = \frac{1}{c}\int_\Omega\left(\int_0^{D_\mathrm{B}}\kappa'\rho'S'e^{-\tau}dD + S_\mathrm{O}e^{-\tau_\mathrm{B}}\right)d\Omega. \tag{2.3}$$

A prime on a position-dependent quantity indicates that it is to be evaluated at $\boldsymbol{r}+\boldsymbol{n}D$ rather than $\boldsymbol{r}$.

Let us now consider the total radiation term (heating plus cooling). Assuming that each fluid element emits isotropically,

$$\frac{dU}{dt} = \kappa\left(c\epsilon - 4\pi S\right), \tag{2.4}$$

and inserting the previously derived expression for ϵ, we obtain

$$\frac{dU}{dt} = \kappa\left(\int_\Omega\left(\int_0^{D_\mathrm{B}}\kappa'\rho'S'e^{-\tau}dD + S_Oe^{-\tau_\mathrm{B}}\right)d\Omega - 4\pi S\right). \tag{2.5}$$

Assume a case where the temperature, and therefore the source function, is constant everywhere ($S = S' = S_\mathrm{O}$). In this case, $\frac{dU}{dt}$ must be zero and it follows that

$$\int_\Omega \left(\int_0^{D_\mathrm{B}} \kappa' \rho' e^{-\tau} dD + e^{-\tau_\mathrm{B}} \right) d\Omega = 4\pi. \tag{2.6}$$

We can now replace the 4π in equation (2.4) with this expression:

$$\frac{dU}{dt} = \kappa \int_\Omega \left(\int_0^{D_\mathrm{B}} \kappa' \rho' \left(S' - S \right) e^{-\tau} dD + \left(S_\mathrm{O} - S \right) e^{-\tau_\mathrm{B}} \right) d\Omega. \tag{2.7}$$

Consider the physical meaning of the integration in the first term: For all directions, we integrate outwards from a point $\boldsymbol{r}$ to the system's boundary. In other words, we are integrating over the volume of the physical system, but using a coordinate system whose origin lies at $\boldsymbol{r}$, so the volume element is $d\boldsymbol{r}' = D^2 d\Omega dD$, and we may write

$$\frac{dU}{dt} = \kappa \left(\int_V \kappa' \rho' \left(S' - S \right) \frac{e^{-\tau}}{D^2} d\boldsymbol{r}' + \int_\Omega \left(S_\mathrm{O} - S \right) e^{-\tau_\mathrm{B}} d\Omega \right). \tag{2.8}$$

As long as the integral is over the whole volume, we may use the usual coordinate system and volume element. From this point onward, we shall abbreviate the product $\kappa\rho$ as χ (the extinction/emission coefficient). The physical interpretation of this equation is as follows:

The volume integral represents the exchange of radiative energy between different positions within the system. Thus, the term with S (cooling term) is the radiation emitted at $\boldsymbol{r}$ and absorbed at some other point $\boldsymbol{r'}$, while the term with S' (heating term) is radiation emitted at $\boldsymbol{r'}$ and absorbed at $\boldsymbol{r}$.

Likewise, the S_O-term in the solid angle integral represents radiation coming from outside the system which is absorbed at $\boldsymbol{r}$, while the S-term represents radiation emitted at $\boldsymbol{r}$ which reaches the boundary and escapes from the system.

The factors $\kappa\chi' e^{-\tau}/D^2$ and $\kappa \int_\Omega e^{-\tau_\mathrm{B}} d\Omega$ can be regarded as exchange coefficients, quantifying the efficiency of the radiative exchange between $\boldsymbol{r}$ and $\boldsymbol{r'}$ and $\boldsymbol{r}$ and the outside radiation field, respectively. Furthermore, equation (2.6) tells us that the volume integral over all of these exchange coefficients, plus the exchange coefficient for the boundary, must be equal to $4\pi\kappa$. This is simply another way of saying that the radiative cooling is equal to $-4\pi\kappa S$.

2.2.2 Spherical Symmetry

In principle, equation (2.8) can be integrated numerically to obtain the radiation term, but in realistic problems the computational cost is prohibitively high.

Many hydrodynamical problems in astrophysics can be reasonably well approximated as spherically symmetric, so that all variables depend only on radius. While this reduces the computational cost, it is still quite slow because the equations include the distance and optical depth between different points. Even in spherical symmetry, these depend on all 3 coordinates. In this section, we shall manipulate the equation in such a way as to reduce this computational load for the case of a spherically symmetric system.

Consider the radiative exchange between a *point* $\boldsymbol{r}$ and an infinitesimally thin, spherical shell at radius r' (Figure 2.1). Calculating the radiation term at point $\boldsymbol{r}$ is sufficient, because spherical symmetry implies that it is the same for every point with radius r.

If we choose the coordinate system such that $\boldsymbol{r}$ lies on the cartesian y-axis, there is no longer any dependency on the azimuthal angle, essentially reducing the system to 2-D. Equation (2.8) tells us that the contribution of the (infinitesimal) shell r' to the radiation term at $\boldsymbol{r}$ is

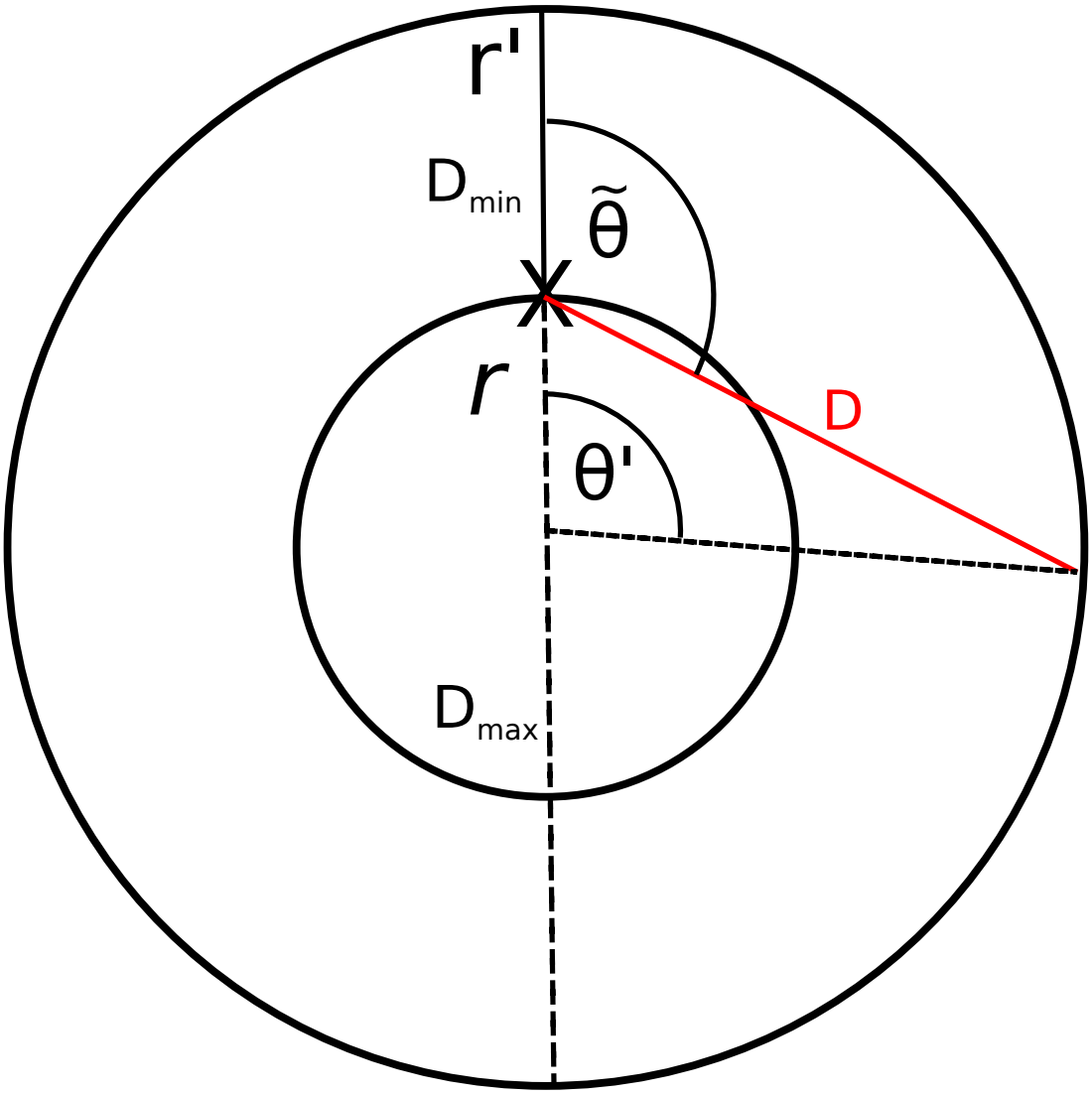

Figure 2.1: A schematic illustration of the situation in spherical symmetry, for the case $r' > r$. The idea is to calculate the radiative exchange between the point $\boldsymbol{r}$ and the infinitesimal shell r'. The red line represents a single ray between $\boldsymbol{r}$ and a point on r'. The full calculation requires an integration over all such rays.
The picture shows the meaning of a number of important variables: The distance between the points D, the polar angle θ', the direction angle $\tilde{\theta}$, and the minimum and maximum distances between shells r and r', which occur at $\tilde{\theta} = \theta' = 0$ and $\tilde{\theta} = \theta' = \pi$, respectively. The optical depth τ is proportional to the distance, but unless χ is constant throughout the system, the proportionality constant depends on the direction of the ray.

$$
\begin{aligned}
R_{\mathrm{r}\leftarrow\mathrm{r}'} &= \kappa\chi' \left(S' - S\right) \int_{\theta'} \int_{\phi'} \frac{e^{-\tau}}{D^2} r'^2 \sin\left(\theta'\right) d\theta' d\phi' dr' \\
&= 2\pi\kappa\chi' \left(S' - S\right) \int_{\theta'} \frac{e^{-\tau}}{D^2} r'^2 \sin\left(\theta'\right) d\theta' dr' \\
&= 2\pi\kappa\chi' \left(S' - S\right) A_{\mathrm{r}\leftarrow\mathrm{r}'}.
\end{aligned}
\tag{2.9}
$$

Numerical integration over r' is of course unavoidable. The main challenge is the calculation of the angle integral:

$$
A_{\mathrm{r}\leftarrow\mathrm{r}'} = r'^2 \int_0^{\pi} \frac{e^{-\tau(\theta')}}{D^2\left(\theta'\right)} \sin\left(\theta'\right) d\theta' dr'
$$

Figure 2.1 illustrates the physical meaning of the variables in this equation. The next section deals with methods of calculating $A_{\mathrm{r}\leftarrow\mathrm{r}'}$.

2.3 Numerical Implementation

2.3.1 General Considerations

In order to perform numerical simulations, we subdivide our system into a finite number of spherically symmetric shells. Within each shell, density, opacity and temperature are assumed to be constant. The contribution of shell j to the radiation term at radius r is determined by:

$$
A_{\mathrm{r}\leftarrow\mathrm{j}} = \int_{r_{\mathrm{jL}}}^{r_{\mathrm{jR}}} r'^2 \int_0^{\pi} \frac{e^{-\tau}}{D^2} \sin\left(\theta'\right) d\theta' dr'. \tag{2.10}
$$

r_{jL} and r_{jR} are the inner and outer boundaries of shell j, respectively. In order to obtain the exchange coefficient between shells i and j, the above expression would have to be integrated over shell i, i.e.

$$
A_{\mathrm{i}\leftarrow\mathrm{j}} = \frac{\int_{m_{\mathrm{iL}}}^{m_{\mathrm{iR}}} A_{\mathrm{r}\leftarrow\mathrm{j}}\left(m\right) dm}{M_{\mathrm{i}}}.
$$

m is the mass coordinate, M_{i} the mass contained within shell i.

Unfortunately, the integration over shell i can only be done numerically, so this method is slow. In addition, if we numerically integrate over j as well (as in section 2.3.3), there are large inaccuracies for neighboring shells near the singularity that occurs at $r = r'$ for $\theta' = 0$. For these reasons, we do not integrate over shell i, but instead we set $A_{\mathrm{i}\leftarrow\mathrm{j}} = A_{\mathrm{r_i}\leftarrow\mathrm{j}}$, where r_{i} is the radius of shell i's center. This definition allows us to accurately calculate the radiation term at radius r_{i}, but note that energy conservation between shells requires that $R_{\mathrm{i}\leftarrow\mathrm{j}} = -R_{\mathrm{j}\leftarrow\mathrm{i}}$. Since the radiation term is power per mass, this implies that $A_{\mathrm{i}\leftarrow\mathrm{j}} M_{\mathrm{i}} = A_{\mathrm{j}\leftarrow\mathrm{i}} M_{\mathrm{j}}$. With this definition, this is generally not fulfilled since the radiation term at the shell center is not equal to the shell average. In other words, when updating shell i, we calculate the effect of *shell* j on *radius* r_{i}, but when updating shell j, we calculate the effect of *shell* i on *radius* r_{j}. This is not symmetric between i and j, which ultimately causes a violation of energy conservation.

Alternatively, it is possible to use the following definition:

$$
A_{\mathrm{i}\leftarrow\mathrm{j}} = \frac{A_{\mathrm{r_i}\leftarrow\mathrm{j}} M_{\mathrm{i}} + A_{\mathrm{r_j}\leftarrow\mathrm{i}} M_{\mathrm{j}}}{2M_{\mathrm{i}}}
$$

The radiation term is now defined as an average between the two directions of transfer. This means the radiation term at r_{i} is no longer calculated as accurately, but this expression is symmetric to exchanging i and j and therefore conserves energy.

The method we develop in the following sections is able to calculate the radiation term at a specific radius exactly in the limit of infinite resolution. Therefore, for the test calculations in this work and to investigate the effect of different resolutions, we use the non-symmetrized definition and from now on we will refer to $A_{\mathrm{r_i}\leftarrow\mathrm{j}}$ simply as $A_{\mathrm{i}\leftarrow\mathrm{j}}$. In a real application, the symmetrized definition may be preferred since it guarantees energy conservation.

2.3.2 Homogeneous Extinction Approximation

The fastest way of calculating $A_{\mathrm{i}\leftarrow\mathrm{j}}$ is to substitute $\tau = \overline{\chi}_{\mathrm{ij}} D$. This is an approximation: It assumes that $\overline{\chi}_{\mathrm{ij}}$, the proportionality constant between distance and optical depth, is a constant independent of θ'. But unless χ is actually constant throughout the whole system, this is clearly not true. Consider again Figure 2.1: If χ increases towards the center, as is usually the case, then rays going through the inner region will have larger values of χ_{ij} than those who move only outwards.

It is ultimately up to the user which value to choose for $\overline{\chi}_{\mathrm{ij}}$; the simplest method, which we adopt here, is to take the value for $\theta' = 0$. If χ increases towards the center, we expect this to cause an overestimation of $A_{\mathrm{i}\leftarrow\mathrm{j}}$ especially for the case $i < j$, and a somewhat smaller overestimation for $i > j$. Despite this inaccuracy, this method can be useful, because it allows us to solve the angle integral analytically and is therefore very fast. We start by expressing the distance D as a function of r_{i}, r_{j} and θ':

$$\begin{aligned} & D^2 = {r_{\mathrm{i}}}^2 + {r_{\mathrm{j}}}^2 - 2 r_{\mathrm{i}} r_{\mathrm{j}} \cos(\theta'), \\ \Rightarrow & 2D\frac{dD}{d\theta'} = 2 r_{\mathrm{i}} r_{\mathrm{j}} \sin(\theta'), \\ \Rightarrow & \sin(\theta')\, d\theta' = \frac{D}{r_{\mathrm{i}} r_{\mathrm{j}}} dD. \end{aligned} \tag{2.11}$$

We insert this into the definition of $A_{\mathrm{i}\leftarrow\mathrm{j}}$ (equation 2.10), but ignore the integration over shell j for the moment and set $r' = r_{\mathrm{j}}$. Using $\tau = \overline{\chi}_{\mathrm{ij}} D$, we obtain

$$\begin{aligned} A_{\mathrm{i}\leftarrow\mathrm{j}} &= \frac{r_{\mathrm{j}}}{r_{\mathrm{i}}} \int_{D_{\min}}^{D_{\max}} \frac{e^{-\overline{\chi}_{\mathrm{ij}} D}}{D} dD \Delta r_{\mathrm{j}}, \\ &= \frac{r_{\mathrm{j}}}{r_{\mathrm{i}}} \int_{\tau_{\min}}^{\tau_{\max}} \frac{e^{-\tau}}{\tau} d\tau \Delta r_{\mathrm{j}}. \end{aligned} \tag{2.12}$$

The indices min and max refer to the minimum and maximum distances/optical depths between the radii r_{i} and r_{j} (see Figure 2.1). The integral over τ can be reformulated using exponential integrals. The exponential integral of order n is defined as

$$E_n(x) = \int_x^\infty \frac{e^- t}{t^n} dt.$$

Using this, equation 2.12 becomes

$$A_{\mathrm{i}\leftarrow\mathrm{j}} = \frac{r_{\mathrm{j}}}{r_{\mathrm{i}}} \left(E_1(\tau_{\min}) - E_1(\tau_{\max}) \right) \Delta r_{\mathrm{j}}. \tag{2.13}$$

We have avoided the numerical integration over θ', and instead have to solve two exponential integrals. This is much faster since analytic formulas are available for the latter. The $\tau_{\max}$-term is negligible in optically thick systems, since in that case $E_1(\tau_{\max}) << E_1(\tau_{\min})$.

We now consider the integration over shell j, so we replace the constant r_{j} with the variable r'. Based on equation (2.13), the dependency on r' is of the form $r' E_1(\tau(r'))$. This can be

integrated analytically using the relation between an exponential integral and its derivative, $\int E_{\mathrm{n}}(x)\,dx = -E_{\mathrm{n+1}}(x) + C$.

We express r' as a function of τ, assume $\frac{dr'}{d\tau}$ =const., and perform integration by parts:

$$\begin{aligned}
&\int r'(\tau)\,E_1(\tau)\,\frac{dr'}{d\tau}d\tau \\
=&\frac{dr'}{d\tau}\left(-r'E_2 + \frac{dr'}{d\tau}\int E_2 d\tau\right) + C \\
=&\frac{dr'}{d\tau}\left(-r'E_2 - \frac{dr'}{d\tau}E_3\right) + C.
\end{aligned} \tag{2.14}$$

The function $r'(\tau)$ differs depending on whether we are looking at $\tau_{\min}$ or $\tau_{\max}$, and whether shell i is inside or outside of shell j:

$$r' = r_{\mathrm{i}} \pm \frac{\tau_{\min}}{\overline{\chi}_{\mathrm{ij}}} = r_{\mathrm{i}} + \frac{\tau_{\max} - 2\overline{\chi}_{\mathrm{ij}} r_{\mathrm{i}}}{\overline{\chi}_{\mathrm{ij}}}. \tag{2.15}$$

Here, $\pm$ means + in the case of $r_{\mathrm{i}} < r'$ and - in the case of $r_{\mathrm{i}} > r'$. In every case, $\frac{dr'}{d\tau}$ is either $\overline{\chi}_{\mathrm{ij}}^{-1}$ or $-\overline{\chi}_{\mathrm{ij}}^{-1}$, validating the above assumption $\frac{dr'}{d\tau}$ =const.

To summarize, we have 3 different relations between r' and τ: $r'_{-}(\tau_{\min})$, $r'_{+}(\tau_{\min})$ and $r'(\tau_{\max})$.

This situation arises because the minimum optical depth (case $\theta' = 0$) either increases or decreases with r' depending on whether $r' > r_{\mathrm{i}}$ or $r' < r_{\mathrm{i}}$, but the maximum optical depth (case $\theta' = \pi$) always increases with r'.

2.3.3 Numerical Angle Integration

We now abandon the assumption of a constant $\overline{\chi}_{\mathrm{ij}}$, which makes it impossible to solve the angle integral analytically. For numerical integration, one may use either variant (2.7) or (2.8) of the basic equation. We choose the latter for consistency with the previous section, but the method discussed here is essentially independent of the formulation used.

Recall that our definition of $A_{\mathrm{i}\leftarrow\mathrm{j}}$ is

$$A_{\mathrm{i}\leftarrow\mathrm{j}} = \int_{r_{\mathrm{jL}}}^{r_{\mathrm{jR}}} r'^2 \int_0^{\pi} \frac{e^{-\tau}}{D^2}\sin(\theta')\,d\theta' dr'. \tag{2.16}$$

We consider rays emitted from point $\boldsymbol{r}$ in directions between $\tilde{\theta} = 0$ and π (see again Figure 2.1 for a visualization of the situation). It is important to note that, unless $r = 0$, the direction angle $\tilde{\theta}$ is different from the polar angle θ'. τ depends on D and $\tilde{\theta}$, so if we have a total of n shells and the number of direction angles considered is a, for each individual frequency we create 2-dimensional arrays of size $n * a$ in which to store the values of τ, D and θ' for each combination of j and $\tilde{\theta}$. Once that is done, the integral can be calculated numerically. In addition, implementing the numerical integration over the radius of shell j is straightforward: Instead of stopping only at each shell center and writing τ, D and θ' there, we do so multiple times within each shell.

The rest of this section describes how to obtain these arrays. For each direction angle $\tilde{\theta}$, we start from position $\boldsymbol{r}$ and then move along the ray from shell to shell until we reach the outer boundary. We will now summarize the algorithm for an individual direction:

First, we define variables representing the current position (initially $\boldsymbol{r}$), distance and optical depth (both initially 0). Then, we move along the ray from one shell to the next, all the while updating distance and optical depth and writing the results in our arrays. θ' can easily be

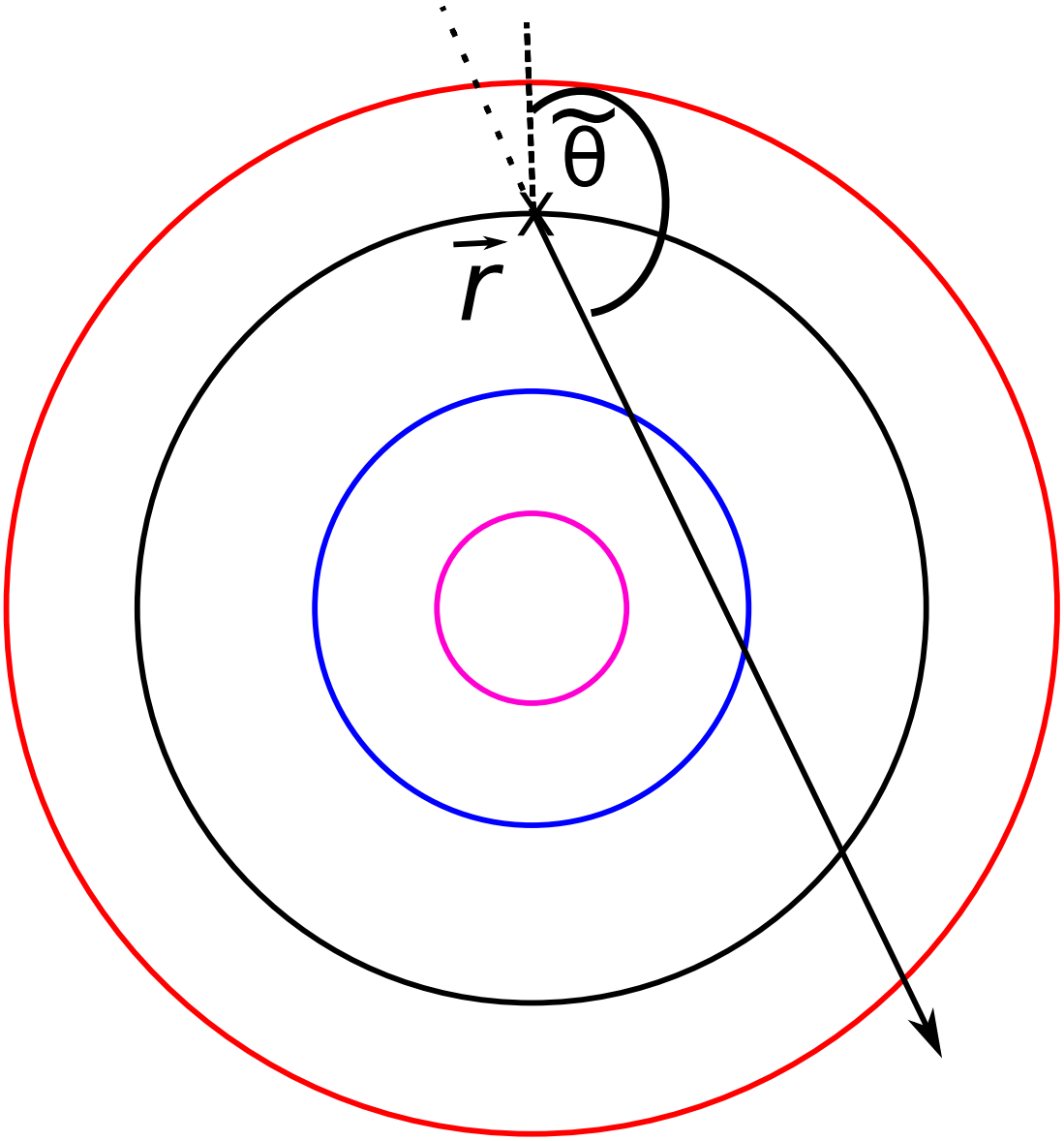

Figure 2.2: We see here a ray moving inward from position $\boldsymbol{r}$. The 4 different cases in section 2.3.3 are illustrated, with the colored shells representing different target radii:
Case 1: Two solutions: The ray crosses the shell once in the positive x-direction, and once more in the negative direction which we ignore.
Case 2: Two positive solutions: The ray crosses the shell once moving inwards, and once again coming out, both in the positive x-direction.
Case 3: No solution: The shell is too small for this ray to hit it at all.
Case 4: Current and target radius are equal so we have a trivial solution ($dx = 0$), and a second solution by moving through the inner region.

calculated from the position. This continues until reaching the outer boundary. This scheme is similar to the "impact parameter" method introduced by Hummer & Rybicki (1971), in the sense that we move from shell to shell along a ray. In that method, parallel rays at different distances (impact parameters) from the center are considered. The calculation then jumps from one intersection of such a ray with a discrete spherical shell to the next in order to track the changing intensity. This can then be used to calculate the moments of radiation and the Eddington factor. The main difference in our method is the fact that we do not follow the intensity, but instead we calculate the distance and optical depth between any two shells in a certain direction, in order to obtain our coefficients for the radiative exchange between those two.

To move along the ray, at every step we must define a "target radius" to reach with the next step. For outward-moving rays ($\tilde{\theta} < \frac{\pi}{2}$), the radial coordinate is always increasing, so the target radius is always larger than the current radius. For inward-moving rays, such as the one depicted in Figure 2.2, the situation is more complicated since the radius decreases down to a minimum before increasing again. In addition, the ray crosses smaller shells not once, but either twice or never (the blue and magenta shells in Figure 2.2).

If our current position is $(x_\mathrm{c}, y_\mathrm{c})$ at radius r_c, we wish to move along the direction of the ray by a distance ΔD until we reach the target radius r_t:

$$\Delta y = \frac{\Delta x}{tan\left(\tilde{\theta}\right)}, \qquad \Rightarrow r_\mathrm{t}^2 = (x_\mathrm{c} + \Delta x)^2 + \left(y_\mathrm{c} + \frac{\Delta x}{tan\left(\tilde{\theta}\right)}\right)^2. \tag{2.17}$$

Defining $g = 1/tan\left(\tilde{\theta}\right)$, after some manipulation we obtain the following quadratic equation for Δx:

$$\Delta x^2 + \frac{2x_\mathrm{c} + 2y_\mathrm{c} g}{1+g^2}\Delta x + \frac{r_\mathrm{c}^2 - r_\mathrm{t}^2}{1+g^2} = 0, \tag{2.18}$$

$$\Rightarrow \Delta x_{1,2} = -\frac{x_\mathrm{c} + y_\mathrm{c} g}{1+g^2} \pm \sqrt{\left(\frac{x_\mathrm{c} + y_\mathrm{c} g}{1+g^2}\right)^2 - \frac{r_\mathrm{c}^2 - r_\mathrm{t}^2}{1+g^2}}. \tag{2.19}$$

This equation tells us how far in x-direction we need to move along the ray to reach the target radius. There are 4 possible cases, whose geometric meaning is depicted in Figure 2.2:

1. $r_\mathrm{t} > r_\mathrm{c}$: There are 2 solutions, one positive and one negative. Since $0 \leq \tilde{\theta} \leq \pi$, all the rays we consider move in the positive x-direction, so we choose the positive solution.

2. $r_\mathrm{t} < r_\mathrm{c}$ and the value under the root is positive: There are 2 positive solutions. We choose the smaller of the two since otherwise we would go through the whole inner region in a single step.

3. $r_t < r_c$ and the value under the root is negative: There is no real solution. This means that the target radius is not reached by this ray. We set $r_\mathrm{t} = r_\mathrm{c}$ and recalculate.

4. $r_\mathrm{t} = r_\mathrm{c}$: One solution is 0 and the other one is $-\left(2x_\mathrm{c} + 2y_\mathrm{c} g\right) / \left(1+g^2\right)$. We choose the latter.

Note that for outward-moving rays ($\tilde{\theta} < \pi/2$), only case 1 occurs since the radius is always increasing.

2.3.4 The Boundary Term

We have not yet considered the second term in the basic equation (2.8). This 'boundary term' is given by

$$\begin{aligned}&\kappa \int_{\Omega} (S_{\mathrm{O}} - S)\, e^{-\tau_{\mathrm{B}}} d\Omega \\ =&2\pi\kappa \int_{\tilde{\theta}} (S_{\mathrm{O}} - S)\, e^{-\tau_{\mathrm{B}}} \sin\left(\tilde{\theta}\right) d\tilde{\theta}.\end{aligned} \tag{2.20}$$

The index O here means the value at the outer boundary, while the index B means "from radius r to the outer boundary". We shall not consider the possibility of a ϕ-dependent S_{O} here, so that we can eliminate the azimuthal angle and treat the system as 2-D. Including the boundary term in the numerical angle integration (2.3.3) is straightforward: We simply add an additional element to our array for τ at the radius of the outer boundary and integrate numerically.

For the constant-χ-method, we must numerically integrate as well since, even if S_{O} is isotropic, there is no analytic solution. τ_{B} can be expressed as $\overline{\chi}_{\mathrm{B}} D_{\mathrm{B}}$, and

$$D_{\mathrm{B}} = \sqrt{r^2 + r_{\mathrm{O}}^2 - 2 r r_{\mathrm{O}} \cos(\theta')}.$$

Here, the polar angle θ' appears again so we require a relation between θ' and $\tilde{\theta}$.

$\tilde{\theta}$ is simply the polar angle of a coordinate system centered at $\boldsymbol{r}$, and D is equivalent to the radial coordinate in that system. Since $\boldsymbol{r}$ lies on the y-axis, for any point (x',y'):

$$x' = D \sin\left(\tilde{\theta}\right), \tag{2.21}$$

$$y' = D \cos\left(\tilde{\theta}\right) + r, \tag{2.22}$$

$$\Rightarrow \tilde{\theta} = \operatorname{atan}\left(\frac{x'}{y' - r}\right). \tag{2.23}$$

Numerical integration is performed over θ'. For each θ', calculate D_{B}, x' and y', which leads to $\tilde{\theta}$ and ultimately $\Delta\tilde{\theta}(\theta')$, allowing numerical integration.

While the lack of an analytic solution makes this comparatively slow, it hardly affects the total calculation time because the boundary term only needs to be calculated once per shell, not n times per shell.

Nevertheless, it is possible to find an analytic solution by approximating $\tilde{\theta} = \theta'$. This approximation only holds if $r << r_{\mathrm{O}}$, but this can be reasonable if, for instance, one is interested in the behavior of a small object inside a large, optically thin envelope.

If S_{O} does not depend on $\tilde{\theta}$, we can use equation (2.11) and $\tau = \overline{\chi}_{\mathrm{B}} D_{\mathrm{B}}$ to write

$$\begin{aligned}&\int_{\tilde{\theta}} e^{-\tau_{\mathrm{B}}} \sin(\theta')\, d\theta' = \frac{1}{r r_{\mathrm{B}} \overline{\chi}_{\mathrm{B}}^2} \int_{\tau_{\mathrm{B}min}}^{\tau_{\mathrm{Bmax}}} e^{-\tau_{\mathrm{B}}} d\tau_{\mathrm{B}} \\ =&\frac{1}{r r_{\mathrm{O}} \overline{\chi}_{\mathrm{B}}^2} \left((1 + \tau_{\mathrm{Bmin}})\, e^{-\tau_{\mathrm{Bmin}}} - (1 + \tau_{\mathrm{Bmax}})\, e^{-\tau_{\mathrm{Bmax}}} \right).\end{aligned} \tag{2.24}$$

2.3.5 Optically Thick Shells

So far, we have implicitly assumed that the individual shells in our system are sufficiently optically thin that the radiative exchange between different points of the same shell is negligible.

The method outlined in the previous sections no longer works if that assumption does not hold. Most of the radiative exchange then should happen within a shell, but in our method, the temperature within each shell is constant, so this internal exchange is by definition zero. This section explains how to expand the method to overcome this problem.

We make use of the constant-χ-approximation and use the expression from equation (2.13) for $A_{\mathrm{i}\leftarrow\mathrm{j}}$. We modify the definition to include $(S'-S)$, which is no longer zero throughout the shell:

$$A_{\mathrm{i}\leftarrow\mathrm{i}} = \frac{1}{r}\int_{r_{\mathrm{iL}}}^{r_{\mathrm{iR}}} r'\,(S'-S)\,(E_1(\tau_{\min}) - E_1(\tau_{\max}))\,dr'.$$

Concerning the applicability of the constant-χ-approximation: If a single shell is optically intermediate or thick already, then the effect of rays which have to move through the interior region will generally be negligible. Because of this, assuming that the direction-independent $\overline{\chi}_{\mathrm{ii}}$ is equal to χ_{i} is generally a good approximation. However, we recognize that this can introduce some inaccuracy in certain atypical scenarios, such as an optically intermediate shell surrounding an optically thin interior region.

We abbreviate $(S'-S)$ as a function $f(r')$ and interpolate it within shell i. We consider here a second-order polynomial of the form

$$f(r') = a\,(r'-r_{\mathrm{i}})^2 + b\,(r'-r_{\mathrm{i}}) + c.$$

Since $f(r_{\mathrm{i}}) = 0$, it follows that $c = 0$, and the other two coefficients can be calculated from the known values $f(r_{\mathrm{i+1}})$ and $f(r_{\mathrm{i-1}})$.

To integrate, r' and f must be expressed as functions of $\tau_{\min}/\tau_{\max}$. We have already done this for r' in equation (2.15). Similarly for f, we obtain

$$f_{\pm}(\tau_{\min}) = \frac{a}{\chi_{\mathrm{i}}^2}\tau_{\min}^2 \pm \frac{b}{\chi_{\mathrm{i}}}\tau_{\min}, \tag{2.25}$$

$$\begin{aligned} f(\tau_{\max}) &= \frac{a}{\chi_{\mathrm{i}}^2}(\tau_{\max}-2\tau_{\mathrm{C}})^2 + \frac{b}{\chi_{\mathrm{i}}}(\tau_{\max}-2\tau_{\mathrm{C}}) \\ &= \frac{a}{\chi_{\mathrm{i}}^2}\tau_{\max}^2 + \left(\frac{b}{\chi_{\mathrm{i}}} - \frac{4a\tau_{\mathrm{C}}}{\chi_{\mathrm{i}}^2}\right)\tau_{\max} + \left(\frac{4a\tau_{\mathrm{C}}}{\chi_{\mathrm{i}}^2} - \frac{2b}{\chi_{\mathrm{i}}}\right)\tau_{\mathrm{C}}. \end{aligned} \tag{2.26}$$

Again, $\pm$ means + for $r' > r_{\mathrm{i}}$ and - for $r' < r_{\mathrm{i}}$, and $\tau_{\mathrm{C}} = \chi_{\mathrm{i}} r_{\mathrm{i}}$ is the optical depth from the center of shell i to the center of the system if χ were constant.

We split the integral into parts:

$$\begin{aligned} &\int_{r_{\mathrm{iL}}}^{r_{\mathrm{iR}}} r' f(r')\,(E_1(\tau_{\min}) - E_1(\tau_{\max}))\,dr' \\ &= +\frac{dr'_-}{d\tau_{\min}}\int_{\tau_{\mathrm{minL}}}^{0} r'_-(\tau_{\min})\,f_-(\tau_{\min})\,E_1(\tau_{\min})\,d\tau_{\min} \\ &\quad + \frac{dr'_+}{d\tau_{\min}}\int_{0}^{\tau_{\mathrm{minR}}} r'_+(\tau_{\min})\,f_+(\tau_{\min})\,E_1(\tau_{\min})\,d\tau_{\min} \\ &\quad - \frac{dr'}{d\tau_{\max}}\int_{\tau_{\mathrm{maxL}}}^{\tau_{\mathrm{maxR}}} r'(\tau_{\max})\,f(\tau_{\max})\,E_1(\tau_{\max})\,d\tau_{\max} \end{aligned} \tag{2.27}$$

The leading factors are χ_{i}^{-1} or $-\chi_{\mathrm{i}}^{-1}$. Since the shell-internal exchange only matters for optically thick systems, the third term is usually negligible unless the shell is optically intermediate and we are so close to the center that $E_1(\tau_{\max})$ is comparable to $E_1(\tau_{\min})$.

After inserting the expressions for the various functions r' and f', we see that these integrals all have the following form:

$$\begin{aligned}&\int \left(\overline{a}\tau^2 + \overline{b}\tau + \overline{c}\right)\left(\overline{d}\tau + \overline{e}\right) E_1(\tau)\, d\tau \\ &= \overline{a}\overline{d} I_{3,1} + \left(\overline{ae} + \overline{bd}\right) I_{2,1} + \left(\overline{b}\overline{e} + \overline{c}\overline{d}\right) I_{1,1} + \overline{ce} I_{0,1} d\tau.\end{aligned} \tag{2.28}$$

The coefficients $\overline{a}$ through $\overline{e}$ depend on the integral in question and

$$\begin{aligned}I_{\mathrm{n,m}}(\tau) &= \int \tau^n E_{\mathrm{m}} d\tau \\ &= -\tau^n E_{\mathrm{m+1}} + n \int \tau^{n-1} E_{\mathrm{m+1}} d\tau \\ &= -\tau^n E_{\mathrm{m+1}} + n I_{\mathrm{n-1,m+1}}\end{aligned} \tag{2.29}$$

This allows us to solve all of these integrals recursively, with $\int I_{0,\mathrm{m}}(\tau) = -E_{\mathrm{m+1}}(\tau) + C$.

2.3.6 Method Summary

In our method, there are three terms contributing to the total radiation term:

1. The radiative exchange between different shells ("External Term")
2. The radiative exchange within the same shell ("Internal Term")
3. The radiative exchange with the background radiation field ("Boundary Term")

The optical depth structure and the resolution determine which of these terms dominate and which are negligible. In a completely optically thin system, the boundary term dominates everywhere. When the system becomes optically thick, but individual shells are still optically thin, the external term dominates the optically thick region, while the boundary term is still important in the outer regions. Finally, if the optical depth becomes so large that individual shells become optically thick, the internal term dominates in that region.

In terms of computational effort, the external term is by far the slowest since even with the fast method (constant-χ-approximation, section 2.3.2), it is $O(n^2)$ for each frequency, while the other two are $O(n)$. With numerical integration over a angles as in section 2.3.3, it becomes $O(an^2)$, and if splitting shell j into x subshells for numerical integration, it increases to $O(axn^2)$.

The internal term could in theory be made obsolete by choosing a sufficiently high resolution that all shells remain optically thin. But in realistic simulations of astrophysical objects such as stars, the opacity and density in the inner region are so high that this is impossible in practice. In addition, it is not desirable since the internal term is much faster than the external term.

We summarize the main advantages of our method:

1. It is accurate for both optically thin and thick systems and smoothly transitions between the two.
2. It is fast, especially when using the constant-χ-approximation. Significant increases in speed can be achieved by neglecting terms (especially the external term) in regions where they are not relevant.
3. The constant-χ-method can be combined with numerical angle integration to achieve the best compromise between speed and accuracy (see section 3.2.4 for details on this).

4. If we ignore the weak temperature-dependency of κ_ν, then the $A_{\mathrm{i}\leftarrow\mathrm{j}}$ for the external and boundary term depend only on the density profile but not on the temperature. In systems where $\rho(r)$ changes much more slowly than $T(r)$, these $A_{\mathrm{i}\leftarrow\mathrm{j}}$ only need to be recalculated very rarely, making the method extremely fast.

Chapter 3

Test Calculations

In this chapter, we test the previously developed method using successively less idealized setups, beginning with cases where the assumption of a homogeneous extinction coefficient is correct (section 3.1) followed by the more realistic case (section 3.2).

3.1 Homogeneous Extinction Coefficient

3.1.1 Constant Temperature

We begin with the simplest possible case: A static, fully homogeneous medium with constant temperature. Of course, the radiation term is zero everywhere in this case, but nevertheless we can assess the accuracy of our method by looking at the radiative cooling only. Even in more complicated cases, the radiative cooling is known to be $4\pi\kappa S$, giving us an analytic result to compare our method to. Unfortunately, an analytic solution for the heating and therefore the total radiation term is generally not available except in this trivial case and in the thermal relaxation test (section 3.1.2).

The accuracy of our method depends on the optical depth structure of the system. In practice, this is different for every frequency, but for our test calculations, it is sufficient to look at a single optical depth array. We therefore employ the gray approximation, using the Planck opacity and expressing S as $\sigma T^4/\pi$.

Instead of the radiation term, we calculate the total radiative cooling by simply setting S' and S_O to zero in all the equations. The optical depth per shell and the number of shells determine which of the three terms in our method dominate. We consider optically thick systems with three different values of τ_S (the optical depth per shell in radial direction):

- $\tau_\mathrm{S} = 0.1$: The external term dominates most of the system, but the boundary term is important in the outer region.
- $\tau_\mathrm{S} = 1$: Internal and external terms are comparable. The boundary term is negligible except in the outermost shell.
- $\tau_\mathrm{S} = 10$: The internal term dominates everywhere.

We discuss the relative error in the cooling rates (Figure 3.1): As expected, the constant-χ method is nearly exact in this case, since the system's density and opacity are homogeneous. The only inaccuracy comes from the limited angular resolution of the boundary term (recall from section 2.3.4 that the boundary term is integrated numerically over all angles θ', even for the fast method). This resolution should be chosen for each shell individually, since for shells very close to the outer boundary, the dependency of distance and optical depth on θ' is much

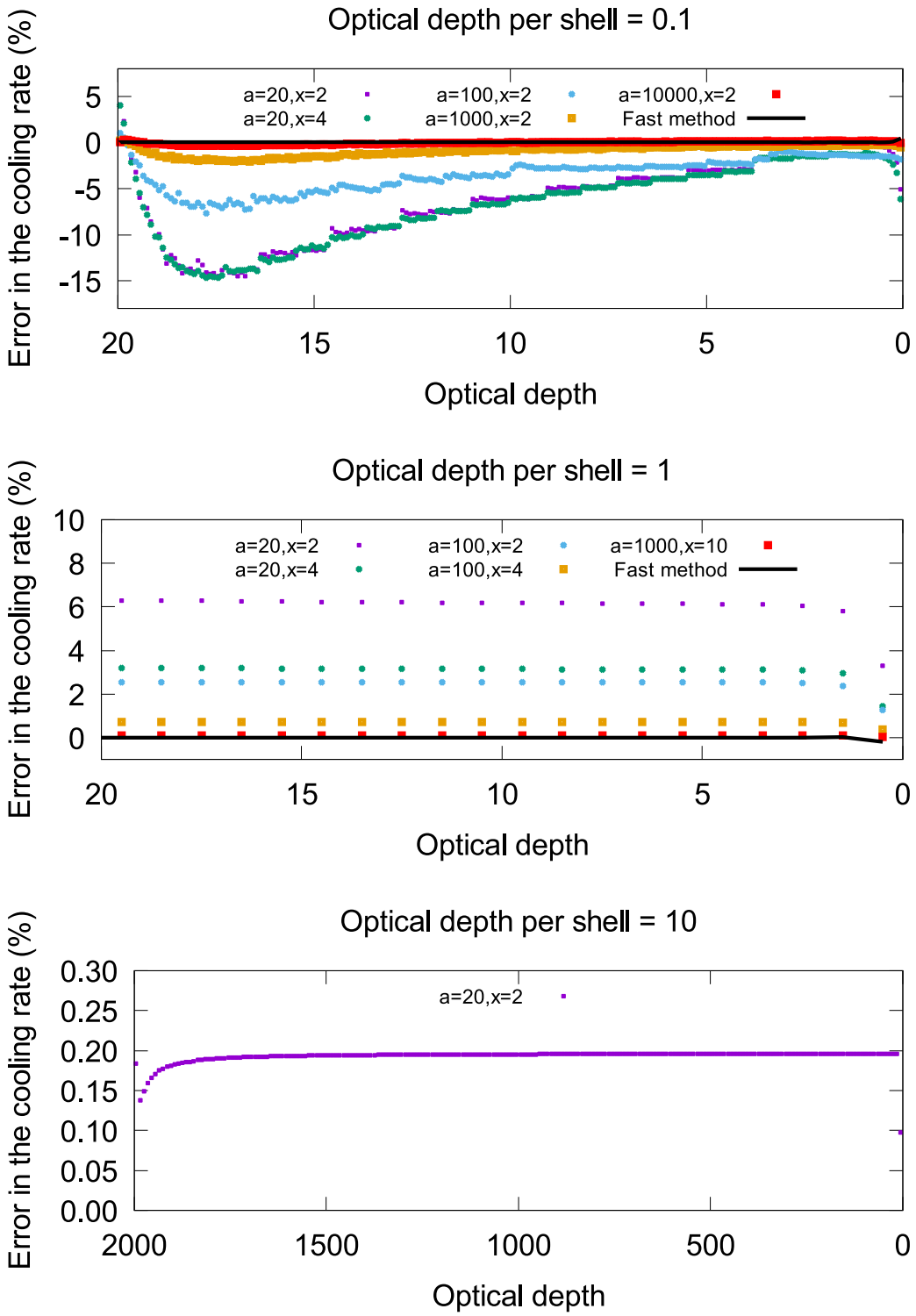

Figure 3.1: Homogeneous system: Relative error in the cooling rate for different optical depths per shell, and for various angular and sub-shell resolutions. The black line shows the result for the fast (constant-χ) method. For the numerical integration cases, a is the number of angles, x is the number of points per shell.

stronger than for shells further inside. We do not investigate the effect of this resolution in detail since its impact on the overall calculation time is very small.

Let us now turn to the numerical integration. We investigate the dependency of the error on two resolutions, namely the angular resolution (number of angles: a) and the radial resolution in shell j (number of points considered in shell j: x).

Consider first the upper two plots. Both have a total optical depth of 20 and a radial size of 1 per shell, but the optical depth per shell and the number of shells differ.

For $\tau_{\mathrm{S}} = 1$, in the lowest resolution case ($a = 20$, $x = 2$) the numerical integration overestimates the result by about 6%. Both increasing a and increasing x helps to reduce this error. In contrast, for $\tau_{\mathrm{S}} = 0.1$, the angular resolution alone determines the accuracy. This is expected since for optically thin shells, the exponential term $e^{-\tau}$ hardly changes between the inner and outer boundary of the shell, so once individual (sub)shells are optically thin, further increase of x has no effect.

We further notice that in the case of optically thin shells, the error is not constant but increases towards the system center up to a maximum, and then decreases again. In addition, higher angular resolution is required to achieve a similar accuracy as the $\tau_{\mathrm{S}} = 1$ case. To understand this behavior, refer to case 3 in Figure 2.2: When calculating the exchange between shell i and a smaller shell j, only a subset of all direction angles $\tilde{\theta}$ actually interact with shell j. This subset becomes smaller as the ratio of r_{j} to r_{i} becomes smaller, effectively decreasing the angular resolution, until it eventually becomes zero. In other words, the exchange with shells smaller than i becomes first inaccurate and then neglected, causing an underestimation of $A_{\mathrm{i}\leftarrow\mathrm{j}}$. This also explains why the error decreases again near the center, since shells there mainly interact with shells larger than themselves. In the case of $\tau_{\mathrm{S}} = 1$, this error does not appear since only the first few neighboring shells contribute, and their radius is very similar to r_{i}.

The magnitude of this error is limited by the fact that smaller shells also have a smaller surface area, decreasing their overall contribution, but care must be taken: Just because some shell j is negligible for the cooling (i.e. it only absorbs a very small amount of the radiation emitted by shell i), does not necessarily mean that it is negligible for the heating as well, since the shell may be very hot. In such a case, it must be ensured that the angular resolution is high enough to capture all shells that are relevant for the heating.

Finally, the case of $\tau_{\mathrm{S}} = 10$ shows only a tiny error even with very low angular and radial resolution. This is understandable since the internal term, which is the only term that matters in this case, depends on neither of these. It does not matter how accurately the external and boundary terms are calculated because they are negligible anyway.

3.1.2 Thermal Relaxation Test

A small temperature perturbation in an otherwise homogeneous system will be smoothed out over time by radiation ("thermal relaxation"), and in this special case an analytic solution can be found. This was first done by Spiegel (1957) for a plane wave, and Masunaga, Miyama, & Inutsuka (1998) showed that the thermal relaxation rate for a spherical wave is exactly the same, provided that the initial perturbation has the form of the zeroth-order spherical Bessel function $j_0(r) = \sin(kr)/(kr)$ (see Figure 3.2 for the concept). This was also confirmed by Stamatellos, Hubber & Whitworth (2007), in which they applied their radiative transfer scheme for SPH simulations to a spherical thermal relaxation test.

Similarly, we test our method by superimposing small perturbations on a base temperature of 10K. We then measure the decay rate for various values of k/χ. Figure 3.3 shows very good agreement with the analytic result, confirming that our method works in the case of a homogeneous system.

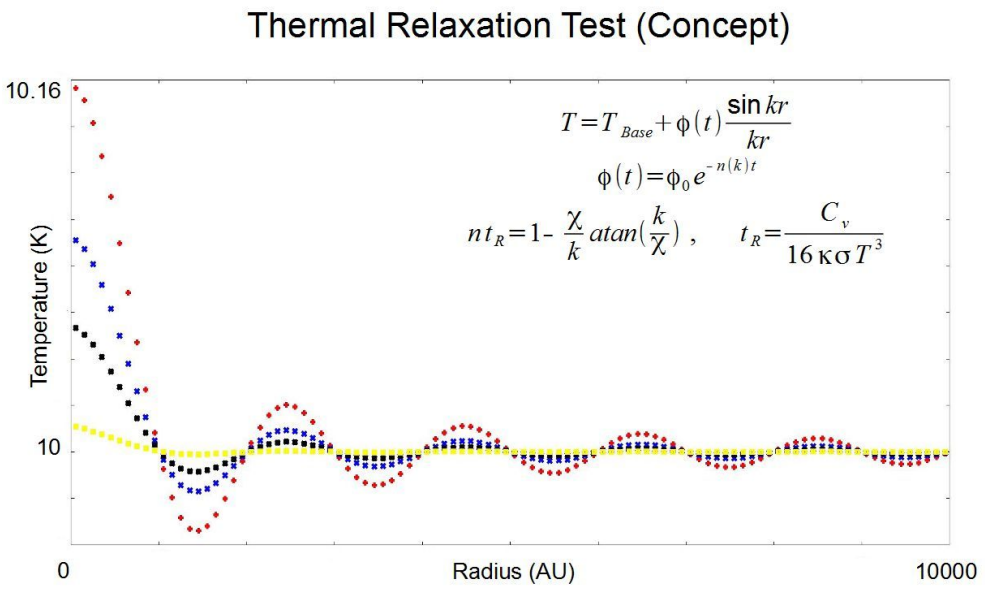

Figure 3.2: Concept of the thermal relaxation mode in spherical symmetry. An initial temperature perturbation with the shape of the zeroth-order spherical Bessel function decays over time (various time steps shown in different colors). The decay rate $n(k)$ can be calculated analytically. For a detailed derivation, see Masunaga, Miyama, & Inutsuka (1998).

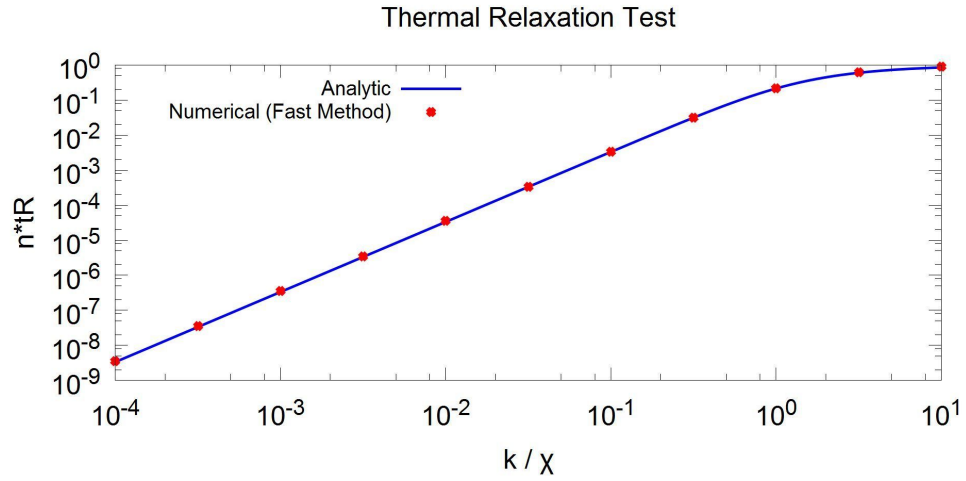

Figure 3.3: Result of the thermal relaxation test. This plot was obtained with the constant-χ-method, but results for the numerical angle integration are indistinguishable even at low resolutions. These results include both calculations with optically thin and optically thick shells. For very large values of k/χ, the result converges towards simple optically thin cooling.

3.2 Variable Extinction Coefficient: Protostellar Collapse Calculations

As an example for a system where χ is not constant, we consider the gravitational collapse of a molecular cloud core. This is the mechanism by which high-density cores within molecular clouds form into stars. From chapter 4, we will apply our method to detailed simulations of this process, but for now, we simply use it as a test for the method. The system transitions from an initially optically thin, constant-temperature, constant-χ state into a a system with a small, hot, optically thick core surrounded by a cold and thin envelope. Therefore, at different stages and different radii over the course of the collapse, all of the three terms in our method become important. For the hydrodynamics part of the simulation, we use an ideal gas equation of state with $\gamma = 5/3$ and a second order Godunov scheme based on Colella & Woodward (1984). We start from the following initial conditions:

- Core mass: $1M_*$
- Initial radius: 10^4 AU
- Initial and background temperature: 10 K
- Initial (constant) number density: $10^4\mathrm{cm}^{-3}$

Figure 3.4 shows the profiles of density and temperature in the late stage of the collapse, when the total (Planck) optical depth τ from the core to the outside has reached 2500.

At this point, we are not looking to provide a realistic simulation of protostellar collapse. We use optically thin cooling until the total optical depth reaches 0.1, and the constant-χ-method with the gray approximation after that. Whenever the system's total (Planck) optical depth crosses certain thresholds (τ=1, 5 , 1000 and 2500), we perform multiple calculations in a single time step (Constant-χ-method as well as numerical angle integration with various resolutions). This provides snapshots of the difference in the results at these time steps.

Since no analytic solution for the heating is available, we have to evaluate the accuracy by considering the total radiative cooling (same as in section 3.1.1). It must be mentioned that this is not unproblematic, because the error in the total cooling is not necessarily representative of the error in the heating and, therefore, in the total radiation term. This is because the radiative exchange between shells i and j is proportional to $A_{\mathrm{i}\leftarrow\mathrm{j}}\left(S_\mathrm{j} - S_\mathrm{i}\right)$, so the total cooling is proportional to $S_\mathrm{i}\sum_j A_{\mathrm{i}\leftarrow\mathrm{j}}$, but the total heating is proportional to $\sum_j A_{\mathrm{i}\leftarrow\mathrm{j}}S_\mathrm{j}$. This means that, depending on the temperature of shell j, a given error in the calculation of $A_{\mathrm{i}\leftarrow\mathrm{j}}$ may have a much larger or much smaller effect on the heating than on the cooling. In consequence, the error in the total radiation term may be quite different from the error in the cooling alone. We will consider the total radiation term in section 3.2.3, but in this section, we will only evaluate the relative error in the cooling.

3.2.1 Homogeneous Extinction Approximation

Consider first the results for the constant-χ-method (Figure 3.5). Recall that for this method, we took the average value of χ between i and j in the radial direction, and assumed that this same value can be used for every direction. Since in reality, χ near the center is now much larger than further outside, we expect this method to significantly overestimate the radiative exchange in the region where the external exchange is important. The plot confirms this: While the result is nearly exact close to the outer boundary, the overestimation increases towards the inside and reaches a maximum near the photosphere. After that, the error decreases again for

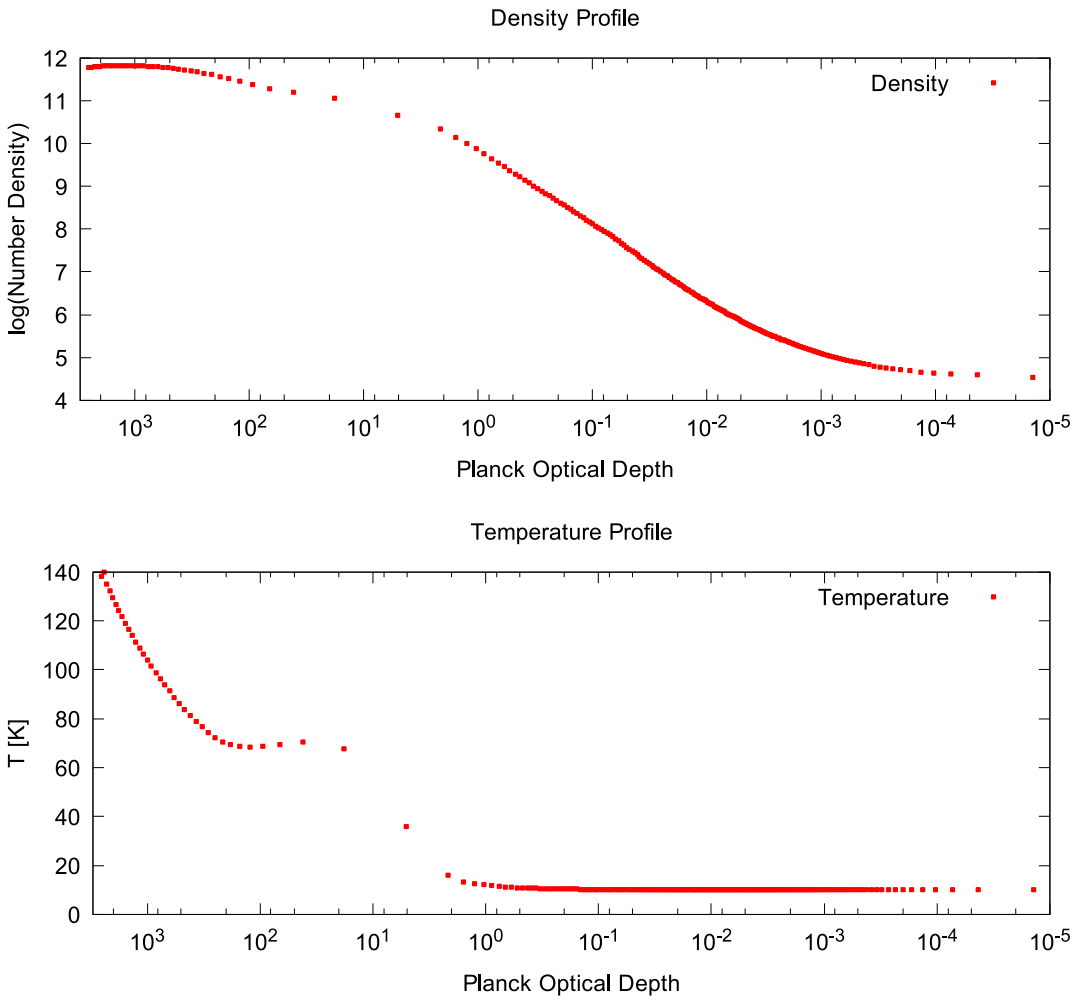

Figure 3.4: Density and temperature plotted against Planck optical depth, in the late stage of a simplified protostellar collapse simulation. A hot and dense interior region (the first hydrostatic core or Larson core) has formed, surrounded by a cold and thin envelope.

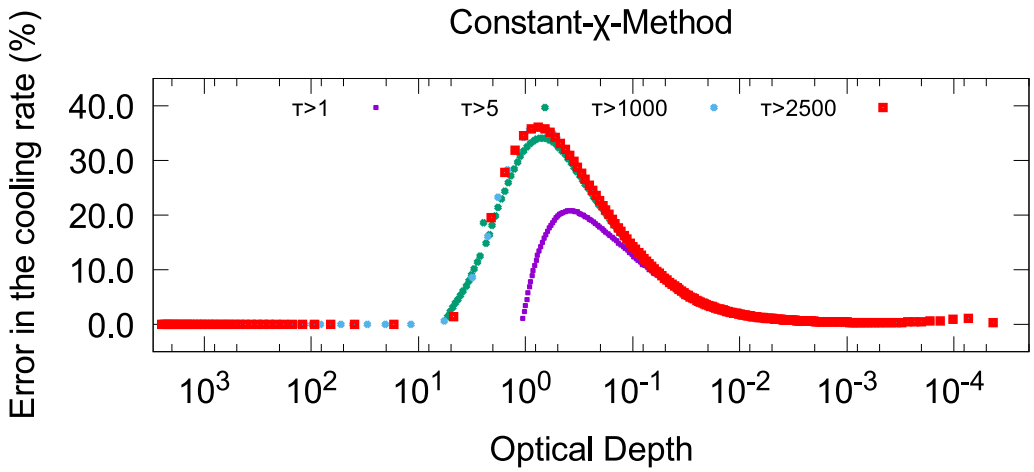

Figure 3.5: Relative error in the cooling rate for the constant-χ-method at different stages in the collapse.

several reasons: In the optically thick region, directions that are much different from the radial direction play a small role; near the center, χ does actually approach direction-independency due to symmetry; and for the very optically thick cases, the external term becomes negligible compared to the internal term.

The maximum error is about 20% in the optically intermediate ($\tau = 1$) case, but increases to 35% when the core is fully optically thick. At this point, the core's optical thickness is essentially infinite so further increases have no more effect.

3.2.2 Numerical Angle Integration

The error in the cooling rate at the same time steps as in section 3.2.1 is shown in Figure 3.6.

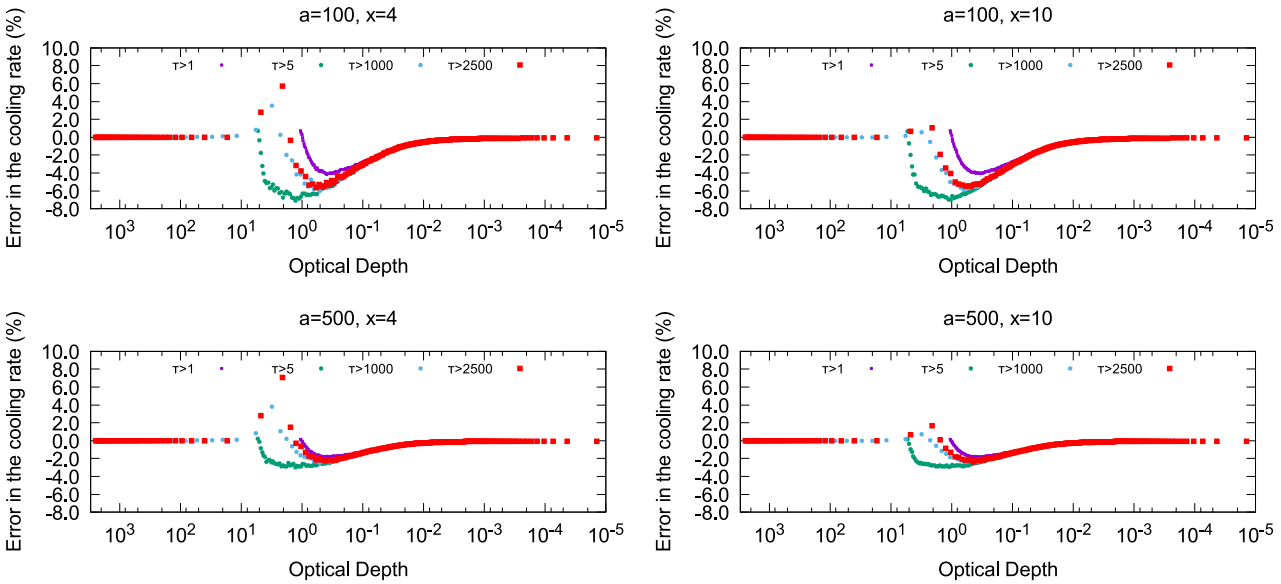

Figure 3.6: Relative error in the cooling rate for numerical angle integration at different stages in the collapse. Subshell resolutions $x = 4$ and $x = 10$, and angular resolutions $a = 100$ and $a = 500$ are shown.

As expected, there is no error in the far outer and deep inner regions. Near the photosphere, we see two different kinds of erroneous behavior: For all optical depths, there is an underestimation of the result reminiscent of Figure 3.1 's $\tau_S = 0.1$ case. The magnitude of this error depends on the angular resolution. In addition, for the very optically thick cases, there

is also an overestimation behind the photosphere. The magnitude of this error depends on the subshell resolution.

The latter error naturally increases with the optical depth per shell, but reaches a maximum at $\tau_S \approx 3$. At even larger values, the internal term starts to dominate the external term, so the error in the latter becomes irrelevant. The internal term does not suffer from this error since it integrates over the radius analytically.

3.2.3 Total Radiation Term

Except for the thermal relaxation test (section 3.1.2), up to this point, we have tried to evaluate our method by comparing the total radiative cooling to the analytic value. As was mentioned in section 3.2, unlike the radiative cooling, the error in the heating depends not only on the optical depth, but also on the temperature profile. This makes it difficult to predict how a given error in the cooling will translate to an error in the total.

Figure 3.7 compares the total radiation terms for different resolutions and for the constant-χ-method at various stages in the collapse. We also include a high-resolution calculation for the symmetric version of the method discussed in section 2.3.1.

We concentrate on the photospheric region since the differences are due to the external term, which is negligible in the deep interior and far outside. We notice several tendencies:

- The net effect of radiation is a radially outward transfer of energy, as should be expected (net cooling inside, net heating outside).
- The constant-χ-method consistently shows a smaller value than the numerical integration. This is understandable since, as was mentioned briefly in section 2.3.2, the overestimation of $A_{i\leftarrow j}$ is smaller for $i > j$ than for $i < j$. This leads to the relative overestimation in the heating being smaller than in the cooling, since the former comes mostly from the inside.
- As the total optical depth increases, so does the jump in χ at the boundary of the first core, which becomes more and more sharply defined. Because of this, the number of shells where the external term is relevant continues to decrease. This is advantageous for the computational speed; however, if a higher resolution of the (post-)photospheric region is desired, some kind of mesh refinement method is needed.
- The differences are most noticeable in the $\tau \approx 100$ case, when there is an optically thick region where individual shells are still optically thin. The error in the fast method is more significant here. Because of this, the pure constant-χ-method may not be a good choice for a realistic calculation.
- Concerning the resolution of the numerical integration: Similar to the results in Figure 3.6, we see that low angular resolution leads to an overall underestimation, while low subshell resolution leads to an overestimation in the optically thick region but has almost no effect further outside. The behaviour of the fast method essentially corresponds to a calculation with minimal angular and infinite subshell resolution. The differences between $a = 100$,$x = 4$ and $a = 500$,$x = 10$ are small, showing that the method has converged.
- The use of the symmetric definition of A_{ij} has only a small effect for optically thin shells, since there is little difference then between fixing the position in shell i and integrating over shell j or doing it the other way around. It also does not matter for very optically thick shells, where the internal term dominates. However, for the intermediate case (interior region of the middle panel in Figure 3.7) the result is significantly different from the non-symmetric case, despite using the same angular and subshell resolutions. Note that the

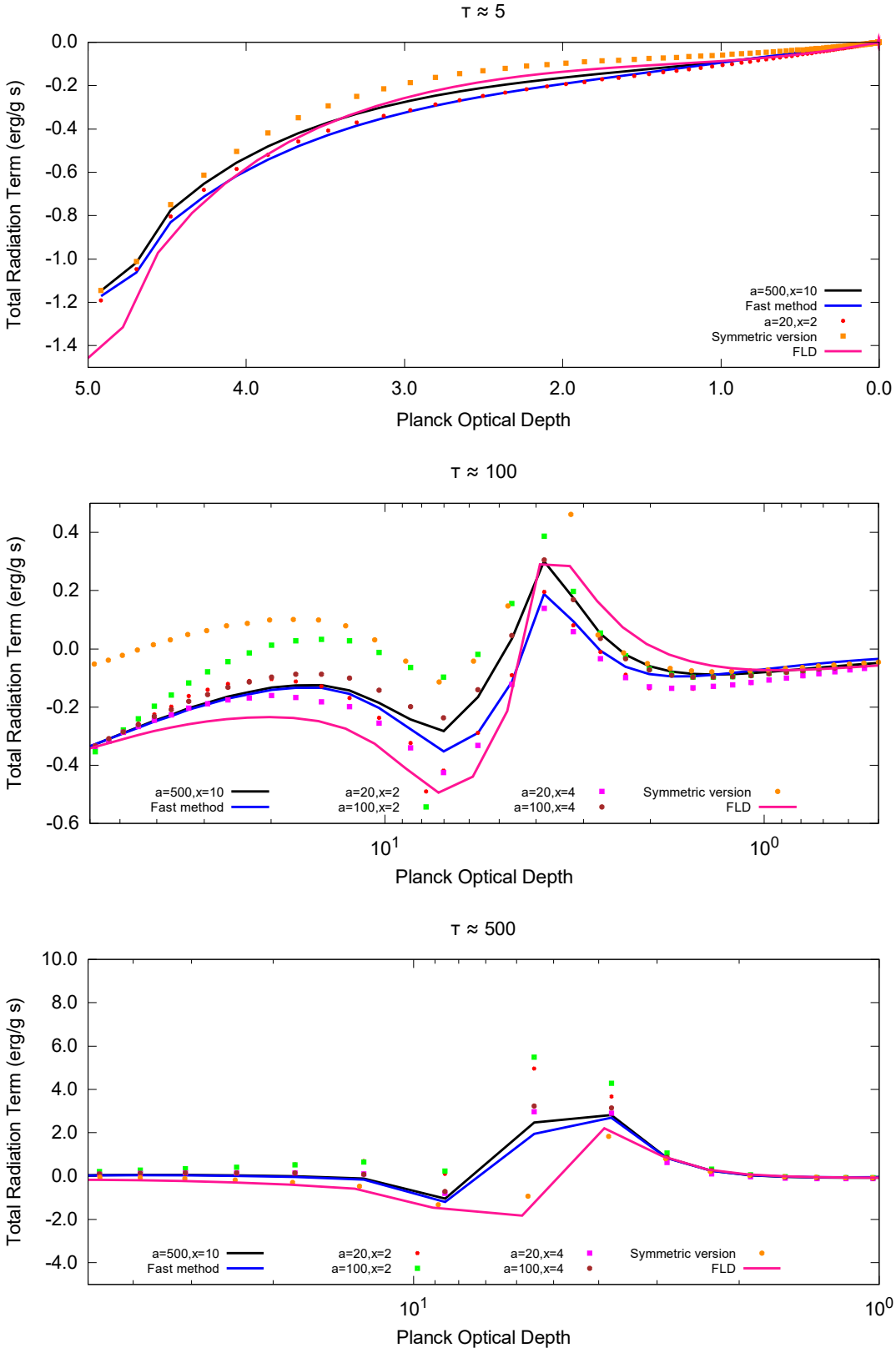

Figure 3.7: Total radiation terms for different resolutions at various stages during the collapse. Note that in the upper panel only, the x-axis is linear instead of logarithmic. The resolution for the symmetric version is a=500,x=10. The results for a flux-limited diffusion (FLD) calculation are also included for comparison.

differences here do not necessarily mean that the symmetric version is less accurate; it is rather that the two versions attempt to do different things. The non-symmetric version is designed to calculate the radiation term at the shell center as accurately as possible, while the symmetric version is intended to calculate a shell-average that guarantees energy conservation.

- As should be expected, the flux-limited diffusion approximation causes significant errors in the photospheric region where individual shells are not yet optically thick.

These results are specific for this particular optical depth and temperature profile, so when applying the method to a different system, the results may differ as well. However, the general situation of a hot, optically thick interior surrounded by a cold, thin envelope is a rather common state in astrophysics.

The differences between the symmetric and non-symmetric versions of the method are expected to disappear in the limit of optically thin shells, since in that case the variation of the radiation term within a shell should vanish. In principle, we could confirm this by performing a protostellar collapse calculation with sufficiently high resolution to keep all shells optically thin throughout the simulation. In practice, the computational cost makes this impossible: The system optical depth after first core formation is already larger than 10^3, so the required number of shells would be 10^4 at the very least, and 10^5 for truly optically thin shells. The presence of optically thick shells is not an issue since they are dominated by the internal term, which is the same for both variants of the methods. However, there will always be a region in which shells are neither fully thin nor fully thick. This is the problematic region in which the external term is important. Increasing the resolution will not make this region disappear, but only move it closer to the system center.

Therefore, we test the convergence of the two variants by using a simplified system in which the density is constant, the velocity is zero and all hydrodynamic calculations are switched off. We introduce a temperature gradient (temperature decreasing outwards from the center) to create a situation similar to the realistic simulation, and the (gray) opacity increases quadratically with temperature. The latter is important to introduce some asymmetry between the different shells: If density, opacity, and radial size of all shells are the same, then the asymmetry that causes the differences between the two variants of the method (section 2.3.1) disappears, and both variants give identical results irrespective of the temperature profile.

Figure 3.8 clearly shows that the two variants, whose results differ substantially in the low-resolution case (optically intermediate shells), are converged for sufficiently high resolution (optically thin shells). Interestingly, the high-resolution results are closer to the low-resolution results of the symmetric than of the non-symmetric method, which indicates that, at least for this setup, the former may be preferable. The flux-limited diffusion results are also included, but as should be expected in this region of optically thin/intermediate shells, they are quite different from the results of our method.

3.2.4 Combined Method

In section 3.2.3, we found that the constant-χ-method is too inaccurate to be used for the whole calculation, at least during the time when there is an optically thick region with optically thin shells. The numerical angle integration is much more accurate, but also much slower. In this section, we will attempt to combine the two in order to arrive at a compromise between speed and accuracy.

This can be done in the following way: At time step t, both slow and fast methods are used to calculate the $A_{\mathrm{i}\leftarrow\mathrm{j}}$. Then, the ratio of the two is written into an array of correction factors $C_{\mathrm{i}\leftarrow\mathrm{j}} = A_{\mathrm{i}\leftarrow\mathrm{j}}\,(fast)\,/A_{\mathrm{i}\leftarrow\mathrm{j}}\,(slow)$. For the following time steps, only the fast method is

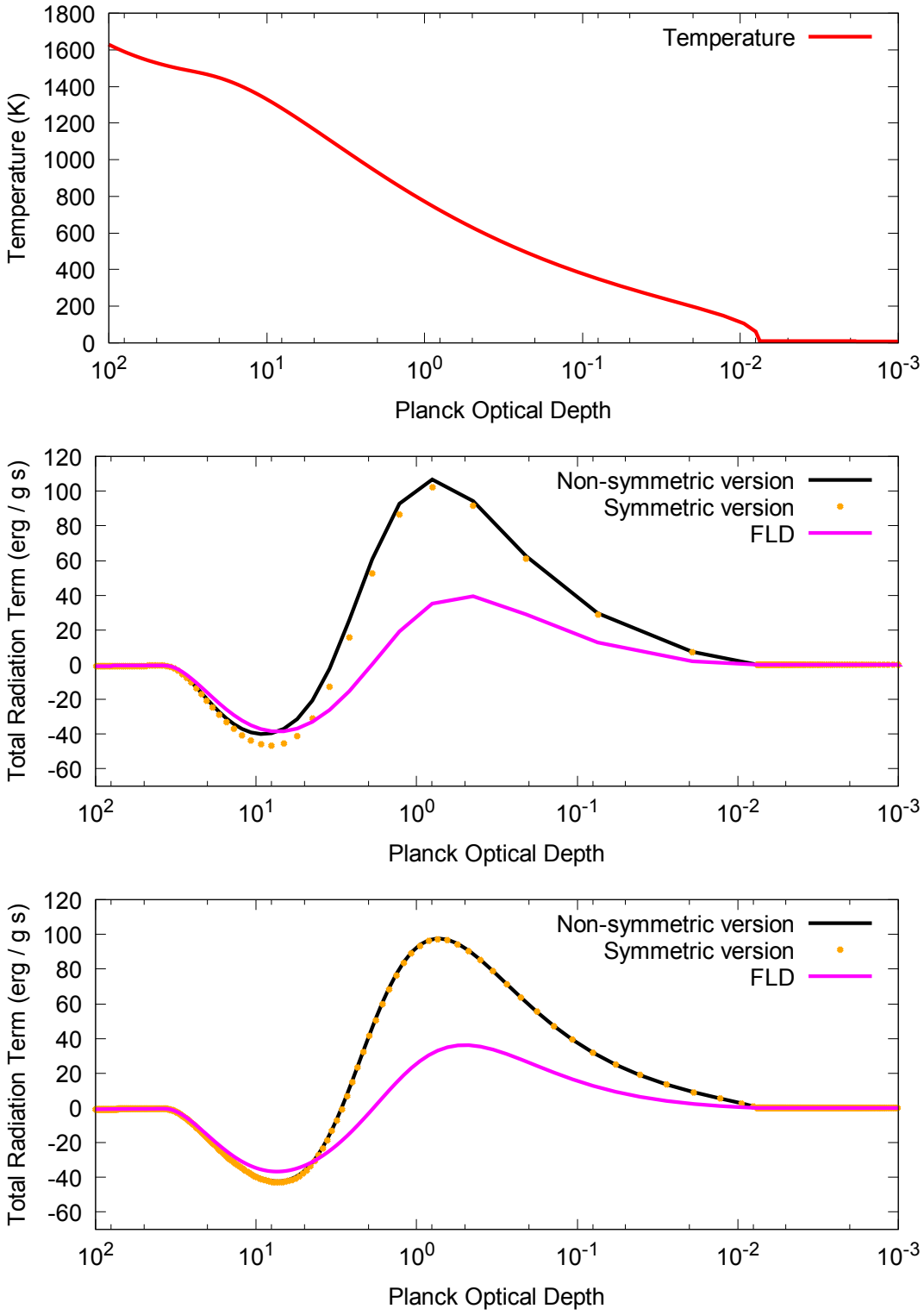

Figure 3.8: Convergence test for the symmetric and non-symmetric versions of the method. The upper panel shows the temperature profile used for this test. The number of shells in the middle panel is 250, and the optical depth per shell is close to 1 near $\tau = 10^1$ and decreases further outwards. In the lower panel, the number of shells is 1000 and the optical depth per shell at 10^1 is around 0.2, i.e. the shells are optically thin throughout the relevant region.

used, and the resulting $A_{\mathrm{i}\leftarrow\mathrm{j}}$ are divided by $C_{\mathrm{i}\leftarrow\mathrm{j}}$. After n time steps, both methods are used and the correction factors recalibrated. From Figure 3.9, we can see that after 5 steps, the results have already become quite inaccurate, so this combined method could only reduce the computational cost by a factor of a few at most. However, this is not true over the whole calculation: Figure 3.9 represents the worst case, as it is during the transition phase when the optical depth structure is changing quickly. In earlier and later stages, acceptable values of n can be much larger. Therefore, instead of being constant, n should be changed dynamically during runtime. We suggest the following method:

First, we choose a number m (for example, $m = 0$ initially) and set $n = 2^m$. Every n timesteps, we perform both slow and fast calculations as described above to obtain the radiation terms dU/dt_{fast} and dU/dt_{slow}. We then calculate the relative error in the internal energy that would result after n timesteps:

$$\delta U = \frac{|dU/dt_{\mathrm{fast}} - dU/dt_{\mathrm{slow}}|n\Delta t}{U}. \tag{3.1}$$

We evaluate this for every shell, and if it is larger than some critical value in any shell, we reduce m by 1. If it is smaller than some other critical value in every shell, we increase m by 1. In this way, the frequency of slow and accurate radiative calculations changes dynamically during the calculation. This method still risks having large errors in some timesteps when m is too large before it can adapt. We can avoid this by including a rollback function as a safety: Every time we perform a slow calculation, we also store all the basic variable arrays such as density, temperature etc. If the error in the next slow timestep (n timesteps later) is too large, in addition to reducing m, we also jump back to the stored values. This guarantees that the maximum error is always smaller than some critical value defined by the user. In practice, this method succeeds in significantly increasing the computational speed compared to the pure slow method, since numerical calculations are only very rarely needed after the first core has established itself and the optical depth structure no longer changes quickly.

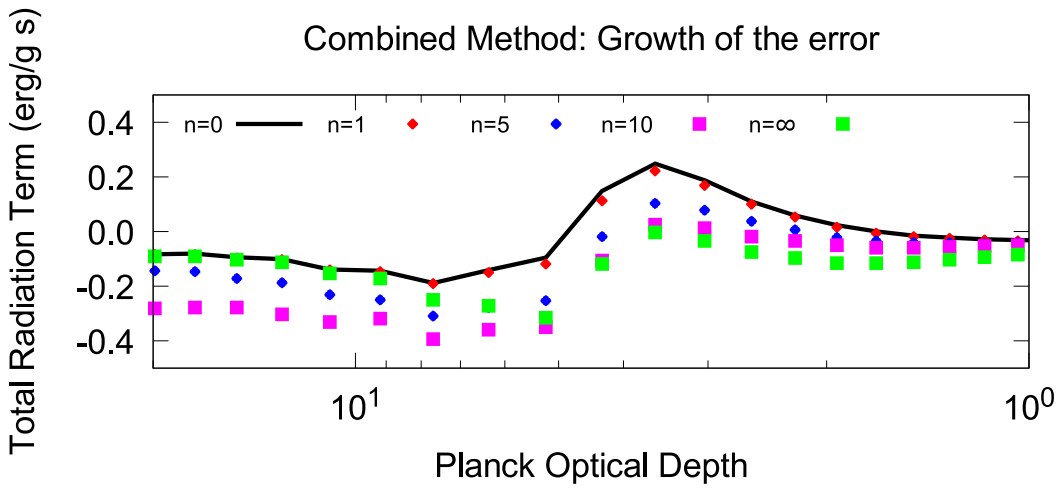

Figure 3.9: Combined method. Snapshots of the photospheric region at a time step when $\tau_{\mathrm{P}} \approx 100$, equivalent to the middle panel of Figure 3.7. n indicates the number of time steps since the correction factors $C_{\mathrm{i}\leftarrow j}$ were last calibrated.

3.2.5 Computational Speed and Optimization

Table 3.2.5 shows the wall-clock time for calculations using the pure fast or pure slow methods. In our calculation, there are three different constraints on the timestep:

Method Type	Shells	Angles	Subshells	Wall-clock time (minutes)
No rad. transfer	200	-	-	< 0.5
Fast	200	-	-	6
Fast	400	-	-	21
Slow	200	20	2	17
Slow	200	100	2	61
Slow	200	20	4	27
Slow	400	20	2	71
FLD	200	-	-	9
FLD	400	-	-	17

Table 3.1: Simplified gray collapse calculations for various shell, angle, and subshell resolutions. The tests were run on a single 3.4 GHz processor and stopped once the total optical depth reached 1500.

- The basic hydrodynamical timestep, determined by the condition that neighboring shells must not overtake each other, i.e. $\Delta t = x\Delta r/(\Delta v + c_{\rm s})$, where Δr and Δv are the differences in radius and velocity of two neighboring shells, and x is a number between 0 and 1. Here we choose x=0.1.

- The radiation timestep. Since the radiation term is very sensitive to temperature, it must be recalculated after the temperature in any shell has changed by more than a certain percentage. Here we choose 1 percent. Note that the exchange coefficients $A_{\rm ij}$ are not updated at this point.

- The opacity timestep. The $A_{\rm ij}$ depend on the optical depth structure of the system, which in turn is determined mostly by the density structure. We update these coefficients whenever the density in any shell has changed by more than 1 percent since the last update. Whenever this is done, the radiation term is also recalculated.

The purely hydrodynamical timestep requires much less computational effort than the ones related to the radiative transfer, as evidenced by the fact that the calculation without RT takes less than a minute. The radiation timestep and especially the opacity timestep are far more time-consuming, the latter even more so if numerical angle integration is used. The calculations shown in Table 3.2.5 required roughly 7500-10000 hydrodynamical timesteps (depending on the number of shells), 3000 radiation timesteps without $A_{\rm ij}$ updates, and 1500-2000 opacity timesteps. Note that the ratios of these numbers may be vastly different in other systems, depending on the time scales at play. The flux-limited diffusion method is comparable in speed to the fast method at 200 shells, but scales better with higher resolutions since it is $O(fn)$. Its speed depends on how many steps are allowed for the radiation field to converge, however.

As mentioned before, the external term is by far the slowest of the three terms in the radiative calculation. If the number of shells is n and the number of frequencies considered is f, the fast method's external term scales as $O(fn^2)$, while the numerical integration over a angles and with x subshells scales as $O(axfn^2)$, which for reasonable resolutions is two to three orders of magnitude slower. This is why optimization requires minimizing the number of numerical integrations, as we did in the previous section.

The separation of the computationally expensive external term from the other two, and the fact that it can be ignored in many regions, is of primary importance. In order to optimize speed, it is imperative to neglect the external term wherever possible, especially in the slow method. In our collapse simulations, we may ignore the external term in the far outer regions, and after first core formation also in the interior because individual shells there are optically thick. In addition, there may be regions where the external term is not negligible, but high accuracy is not required. In this case, instead of completely neglecting it, one may calculate

it using only the fast method. These optimizations can reduce the actual time required by an order of magnitude or more compared to the values seen in Table 3.2.5. In any case, the optimization strategy must be adapted according to the problem.

3.3 Conclusion and Future Development

In this work, we have developed a new method of treating the radiative transfer in a spherically symmetric fluid system. Based on the transfer equation, we derived a scheme that is reduced to the calculation of exchange coefficients $A_{\mathrm{i}\leftarrow j}$ between pairs of shells ("external term"), between a shell and the radiation coming from outside the computational domain ("boundary term"), and between the shell center and other points within the same shell ("internal term"). The external term is by far the most problematic of these, since the calculations of the other two are both much faster and produce (nearly) exact results.

Numerical integration over all angles can solve the external term to a high degree of accuracy if a sufficiently large number of angles is used, however it is quite slow. By assuming a direction-independent absorption coefficient, the speed can be increased by two to three orders of magnitude, but at the cost of reduced accuracy. The resulting error is most evident in regions that are optically thick while individual shells are still optically thin. A combined method of numerical angle integration and constant-χ-approximation can be used as a compromise between speed and accuracy.

Future improvements of the method will likely focus on speed optimization, either directly by increasing the speed of the numerical angle integration, or indirectly by increasing the accuracy of the fast method to make it more usable. Several approaches are possible:

- Flexible resolutions: In this work, we have taken the angular and subshell resolutions to be constant throughout a given test run. It may be far more effective to change them during runtime. For example, x only needs to be larger than 1 for shells in a certain optical depth range between about 0.1 and a few, and a can be smaller near the center, where there is little exchange with shells smaller than i.

- For the constant-χ-method, we use the average χ between shells i and j in direction $\tilde{\theta} = 0$. There may be better options, such as a weighted average between the $\tilde{\theta} = 0$ and $\tilde{\theta} = \pi$ directions. In addition, the effect of the optically thick core could be approximated by defining a "shadow region" in the interior and reducing $A_{\mathrm{i}\leftarrow j}$ accordingly.

- The main reason that the numerical integration is so slow is because of the high angular resolution required, which is a consequence of the fact that many rays emanating from a given shell i fail to interact with shell j if the latter is much smaller than i (case 3 in Figure 2.2). However, instead of calculating $A_{\mathrm{i}\leftarrow j}$ and $A_{\mathrm{j}\leftarrow i}$ separately, one may calculate $A_{\mathrm{i}\leftarrow j}$ only for the case of $i < j$ and reuse this value when updating shell j. Aside from the obvious decrease by a factor of 2 in the computation time, this also reduces the angular resolution required, and has the additional advantage of guaranteeing energy conservation. But this method is problematic: $A_{\mathrm{i}\leftarrow j}$ is the exchange coefficient between r_{i} and the whole of shell j. As we discussed in section 2.3.1, this is conceptually different from $A_{\mathrm{j}\leftarrow i}$, the exchange coefficient between r_{j} and the whole of shell i. If one is willing to accept this inconsistency, a significant performance increase may be possible.

In conclusion, the performance of the method will depend strongly on steps taken for optimization, and which methods of optimization are effective will depend on the optical depth and temperature structure of the system in question.

Chapter 4

On the Initial Conditions of Brown Dwarf Formation

We now apply our newly developed scheme to an actual physical problem: The formation of brown dwarfs. This chapter focuses on the creation of brown dwarfs through the turbulent compression scenario, as discussed in section 1.4. We give a detailed explanation of the simulation's setup (most of which also applies to chapter 5), followed by a discussion of our results.

4.1 Simulation Setup

The numerical simulations described in this chapter are simplified in so far that they use an ideal gas equation of state and a constant ratio of specific heats, $\gamma = 5/3$. For the present purpose, this is sufficient since we are only interested in whether or not a first core forms. The further evolution, namely the second collapse and second core formation, requires a more realistic equation of state to incorporate the effect of hydrogen dissociation. This will be done in section 5.

Our hydrodynamics module is based on Colella & Woodward (1984)), although we use a spatially second-order (piecewise linear) Godunov scheme rather than their piecewise parabolic one. The governing equations of the system in Lagrangian conservation form are as follows:

$$\frac{dV}{dt} = \frac{d(r^2 v)}{dm} \tag{4.1}$$

$$\frac{dv}{dt} = -r^2 \frac{dp}{dm} - \nabla\Phi \tag{4.2}$$

$$\frac{dU}{dt} = -\frac{d(r^2 vp)}{dm} - v\nabla\Phi + \left(\frac{dU}{dt}\right)_{\text{rad}} \tag{4.3}$$

$$\Delta\Phi = \frac{4\pi G}{V} \tag{4.4}$$

$$p = (\gamma - 1)\frac{(U - v^2/2)}{V} \tag{4.5}$$

The equations are formulated in terms of the mass coordinate $m(r)$, which is equal to the enclosed mass divided by 4π. V, v and U are the specific volume, velocity, and specific energy. The effect of radiation is included as the term $\left(\frac{dU}{dt}\right)_{\text{rad}}$ in the energy equation. This is the radiation term whose calculation we described in the method development (chapter 2). We ignore the effect of radiation pressure throughout this work.

When testing our program, we encountered a problem with the term $v\nabla\Phi$ in the energy equation. This term represents the energy gained or lost by the fluid due to gravity. Colella

& Woodward (1984) include a non-specified "external body force" g in their scheme, in which case the numerical implementation of the resulting term vg is an average of the value before the current timestep and the value after the timestep, i.e. $(v^n g^n + v^{n+1} g^{n+1})/2$. This is only an approximation and hence not perfectly conservative. In fact, we found that in our self-gravitating case this approximation caused a continuous increase in the total energy of the system. In other words, the increase in the fluid energy in each time step was larger than the corresponding decrease in gravitational potential energy, leading to an abnormally strong increase in pressure and a general "bounciness" of the collapsing core. We have solved this issue by manually calculating the gravitational energy in each shell before and after the time step, and inserting the difference in the energy equation in place of the term $-v\nabla\Phi$. This method achieves perfect energy conservation within the hydrodynamic part of the calculation.

The boundary condition at the center is $v = 0$, while the outer boundary is infalling. This infall velocity is calculated from the velocity of the outermost shell, under the assumption that v varies linearly over the shell. As for the radiative boundary condition, we take the system to be surrounded by a homogeneous, 10 K blackbody radiation which keeps the core at its initial temperature of 10 K. We will consider a less idealized boundary condition in section 5.

We use the frequency-dependent dust opacities computed by Semenov et al. (2003), sampled into 40 log-equally spaced frequency bins. At the higher temperatures encountered in later stages of the collapse, the dust grains evaporate and the opacity becomes dominated first by molecular and then by atomic absorption. These effects will be included in section 5, but at this point we only consider the dust opacity.

We envision an isothermal, brown dwarf mass cloud core which is initially in hydrostatic equilibrium and stable to gravitational collapse, i.e. a subcritical Bonnor-Ebert sphere (Bonnor (1956); Ebert (1955)). If this cloud core is overrun by a region of high turbulent pressure, it will be compressed to a higher density, and if this compression if sufficiently strong, it may be destabilized and collapse. We model this process by adding an external pressure at the outer boundary of our system:

$$P_{\rm ext} = P_{\rm ext,init} e^{-\frac{t}{t_{\rm D}}},$$

where $t_{\rm D}$ is the timescale at which this external pressure decays. This decay is to simulate the fact that the turbulent high pressure region is itself moving, so the core will only be affected by it for a certain time. Our simulation has the following parameters:

- $n_{\rm C}$ (central number density)
- $R_{\rm O}$ (initial radius)
- $P_{\rm ext,init}$ (initial external pressure)
- $t_{\rm D}$ (time scale for the external pressure to decay)

Hydrostatic equilibrium for a self-gravitating, isothermal sphere can be described by the following equation:

$$\frac{dP}{dr} = -G\frac{M(r)}{r^2}, \tag{4.6}$$

where $M(r)$ is the enclosed mass at radius r. We assume a constant temperature of 10 K and set up the system by fixing $n_{\rm C}$ and $R_{\rm O}$ and numerically integrating this equation outward from the center. The total mass is then determined, as is $P_{\rm O}$, the pressure at the outer boundary. The external pressure is then added on top of $P_{\rm O}$. An important derived parameter is the Bonnor-Ebert mass $M_{\rm BE} = 1.18 c_{\rm s}^4 P_{\rm O}^{-1/2} G^{-3/2}$, which is the critical mass above which the core would be unstable to gravitational collapse even without any external pressure. For all the calculations in this section, $M < M_{\rm BE}$.

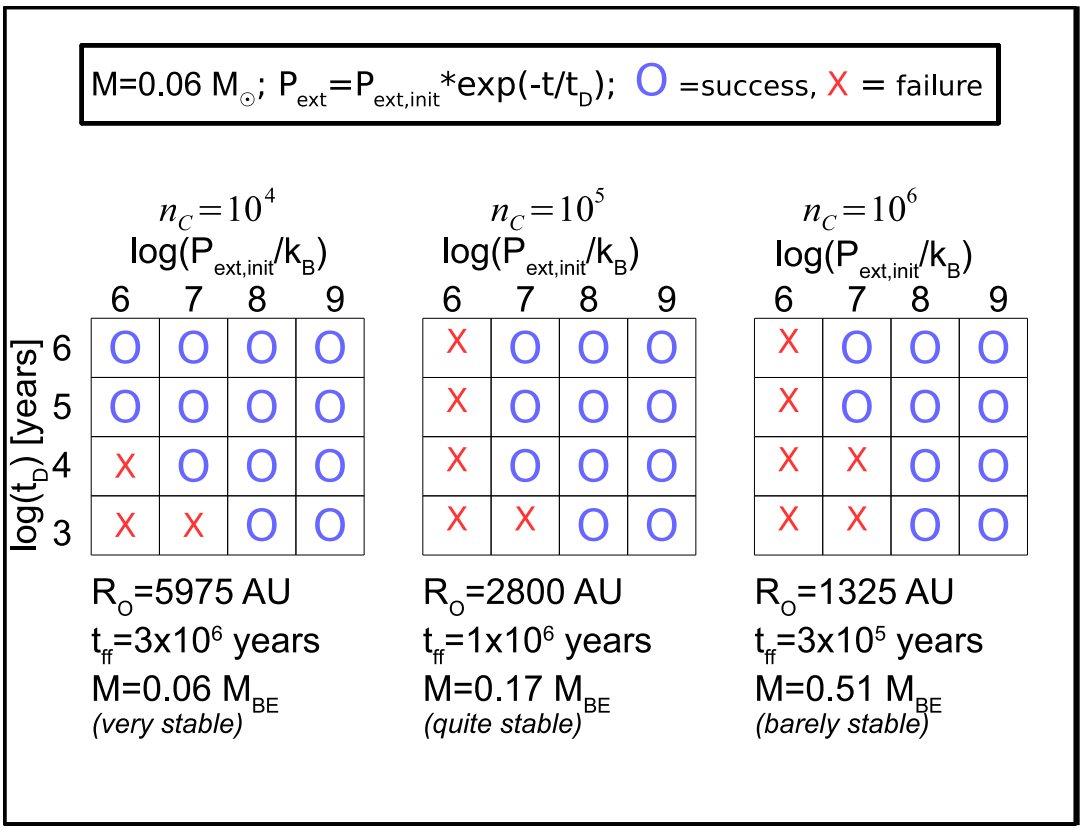

Figure 4.1: Forming brown dwarfs by turbulent compression. The initial temperature is 10K and the total core mass is $0.06 M_\odot$. The three boxes correspond to three different central densities. Within each box different columns represent different values for the initial external pressure, and different lines represent different values for the decay timescale. For each box, the initial core radius, the free-fall time and the mass in units of the Bonnor-Ebert mass are given. A blue circle for a combination of parameters signals that a collapse occured in that calculation, i.e. a proto-brown dwarf was formed. Red X-symbols mean that in this calculation, the core only oscillated without ever collapsing.

4.2 Results

We perform a number of simulations while varying the parameters described in the previous section, and check whether the collapse proceeds to form a first hydrostatic core or whether it only oscillates without collapsing. The results are shown in Figure 4.1. We notice the following patterns:

- Larger external pressures and longer decay times are more favorable in order to trigger a collapse, as should be expected.
- Setups with higher central density appear to be more resistant to collapse. This may seem unintuitive at first, but it becomes clear when one considers the thermal pressure. For example, in the case of $n_C = 10^6 \mathrm{cm}^{-3}$ and $T = 10\mathrm{K}$, the internal pressure is $10^7/k_B$. It is obvious that an additional external pressure that is much lower than this will have no significant effect on the overall evolution, no matter for how long it acts. Thus the difference between the internal and external pressure is important.
- With the previous consideration, we see that the higher-density cores, whose ratio of M to M_{BE} is larger, are actually more unstable. For example, in the case of $n_C = 10^4 \mathrm{cm}^{-3}$, an external pressure one or even two orders of magnitude larger than the internal pressure still fails to cause a collapse if the decay time is short. On the other hand, for $n_C = 10^6 \mathrm{cm}^{-3}$, even an external pressure equal to the internal pressure can cause a collapse.

In summary, then, the qualitative behavior of the above results is as expected. Next, we wish to interpret them quantitatively: Assuming typical molecular cloud conditions, how likely

is it that a turbulent high pressure region will affect a pre-brown dwarf core for long enough to cause it to collapse?

A typical number density for a molecular cloud is 10^2cm^{-3} and the typical turbulent velocity is on the order of 1 km/s, giving a turbulent pressure $P_{\text{ext,init}}/k_{\text{B}} \approx 3 \times 10^6$. Let us be generous and assume $P_{\text{ext,init}}/k_{\text{B}} = 10^7$. From our simulations, we know that this pressure must act on the core for $t_{\text{D}} = 10^3\text{yr}$ (lower boundary) in order to create a brown dwarf, for both $n_{\text{C}} = 10^4\text{cm}^{-3}$ and $n_{\text{C}} = 10^5\text{cm}^{-3}$. Using the initial core radius R_{O}, and assuming that the high-pressure region also moves at $v = 1$ km/s, we can translate the time scale requirement into a size requirement for this region. For the case $n_{\text{C}} = 10^4\text{cm}^{-3}$:

$$R_{\text{min}} = R_{\text{O}} + vt_{\text{D}} \approx 8,000\text{AU}$$

With the even more favorable $n_{\text{C}} = 10^5\text{cm}^{-3}$, the result becomes $R_{\text{min}} \approx 4900\text{AU}$ due to the smaller value of R_{O}. The required time scales are the same for both cases because of the limited amount of calculations; in practice, the higher-density core's t_{D} will be closer to the lower bound of 10^3yr which we have assumed for both cases here.

Despite our optimistic assumptions, this is a very large scale. It seems unlikely that coherent high-pressure regions of this size are common enough in molecular clouds to explain the observed number of brown dwarfs. However, if they do exist, they should be observable, so this could be used as an observational test: Unless such regions are found, we conclude that the turbulent compression scenario is not a main formation channel for brown dwarfs, although it may occur on rare occasions where conditions are especially favorable. Note also that our simulation is spherically symmetric and does not include the magnetic field, which tends to have a stabilizing effect and should make it even harder to trigger a collapse.

Chapter 5

Full Protostellar Collapse Calculations

In this chapter, we expand our code to include effects necessary to accurately simulate the second collapse phase: A realistic, non-ideal equation of state which reflects the effect of hydrogen dissociation, and molecular and gas opacities for high temperatures at which dust grains have evaporated. We then perform simulation runs of the whole protostellar collapse process for varying initial conditions, with a special focus on the brown dwarf regime.

5.1 Equation of State

In place of the ideal equation of state (equation 4.5), we use an EOS table developed by Kengo Tomida (Princeton University) and Yasunori Hori (National Astronomical Observatory of Japan), which is described in detail in Tomida et al. (2012) and Tomida, Okuzumi & Machida (2015) and whose effect is visualized in Figure 5.1. This table was calculated under the assumptions of local thermodynamical and chemical equilibrium. The latter is only valid if the timescale for chemical reactions is much shorter than the dynamical timescale, but since we are dealing with very dense gas this condition holds. Furthermore, the EOS table assumes solar abundance ($X = 0.7$, $Y = 0.3$, heavy metals are not considered), and a constant ratio of ortho- to parahydrogen of 3:1. This ratio affects the thermodynamic properties of the gas, but its actual value in molecular cloud cores is poorly constrained. We do not investigate its effect at this point. Finally, as the authors themselves note in appendix A of Tomida et al. (2012), the EOS becomes unphysical in very high density regions ($\rho > 0.1$ g cm^{-3}) since the neglected non-ideal effects are important in that region. This is not an issue for us since our calculations only reach densities about an order of magnitude lower.

5.2 Opacity

We use the monochromatic opacities by Vaytet & Haugbølle (2017), available for download at `http://starformation.hpc.ku.dk/?q=grid-of-protostars`. These are a combination of the Semenov et al. (2003) dust opacities for temperatures below 1500 K, molecular opacities calculated based on Ferguson et al. (2005) for the temperature range between 1500 and 3200 K, and atomic opacities from the Opacity Project (Badnell et al. (2005)) above 3200 K. The minimum and maximum frequencies as well as the number of frequency points differ for these three regimes, and the opacities themselves depend on temperature and density. Thus, the actual opacity data used when calculating the radiation term for a given shell in our calculation are chosen depending on that shell's temperature and density. We use 40 frequency bins for all our runs. The frequency and opacity values for each bin are obtained by averaging over several neighboring values in the original opacity data.

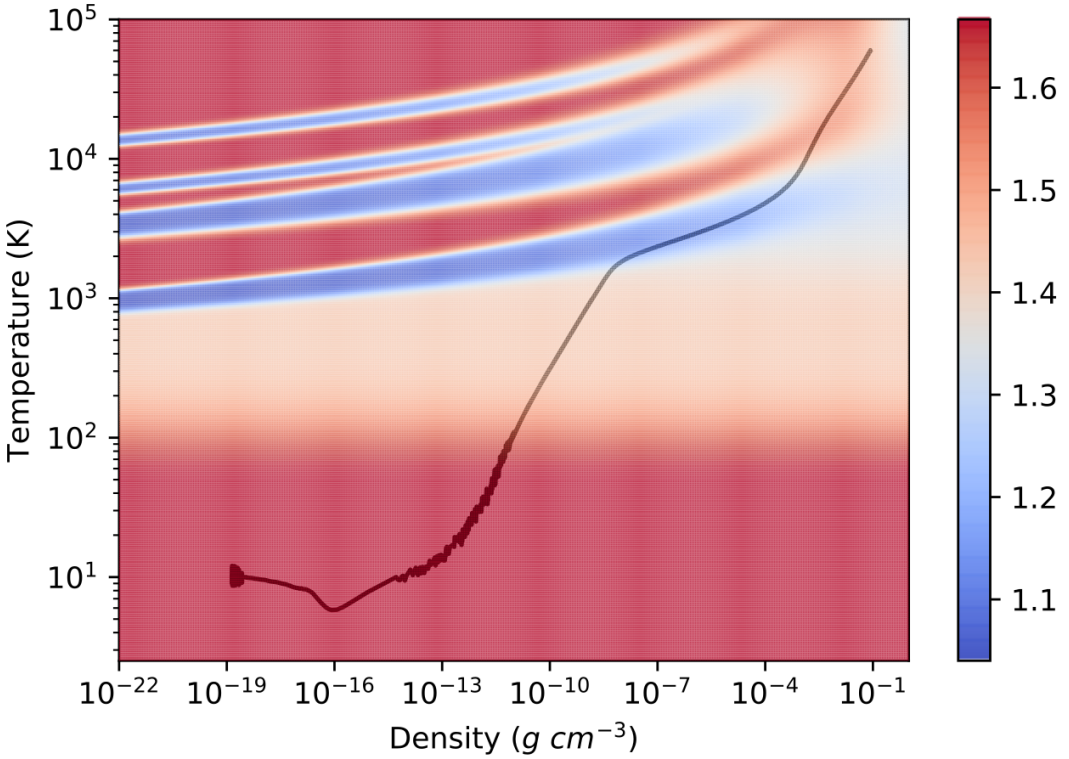

Figure 5.1: Visual representation of the realistic EOS by Tomida et al. (2012). The black line shows a typical evolutionary track in the ρ-T-plane (see also Figure 1.3), while the colored background shows the value of the adiabatic index γ at that point. Note the initial decrease in temperature caused by the attenuation of background stellar radiation, which is only captured in frequency-dependent calculations (section 5.5.1). The region below about 100K corresponds to $\gamma = 5/3$, the value for a monatomic gas, due to the hydrogen molecule's rotational degree of freedom being inactive at these temperatures. At higher temperatures, it decreases to $\gamma = 7/5$, the value expected for a diatomic gas. The four bands of lowered γ correspond, from bottom to top, to four endothermic reactions: The dissociation of H_2, the ionization of hydrogen, and the first and second ionization of helium.

5.3 Initial and Boundary Conditions

Apart from the differences discussed in the preceding two sections and the lack of an external pressure, the overall method is the same as in section 4. However, one further change concerns the radiative boundary condition: Instead of a 10 K blackbody background radiation, we now employ the more realistic setup of Masunaga & Inutsuka (2000), where the heating from the outside is a combination of three separate contributions:

- Heating due to cosmic rays, for which we adopt the value of $6.4 \times 10^{-28} n(H_2)$ erg m^{-3} s^{-1} (Goldsmith & Langer (1978)). This is implemented simply as an additional, constant term in the energy equation.
- A 2.7 K blackbody radiation representing the cosmic microwave background.
- A 6000 K blackbody radiation representing background stellar photons, diluted by a factor so as to keep the initial cloud at $\approx$ 10 K.

Following Vaytet & Haugbølle (2017), we stop each run once the density in the central shell decreases from one time step to the next for the first time after the beginning of the second collapse. There are several reasons for this: First, it allows a comparison of different runs at the same point during their evolution, namely the point where the second collapse ends and a first "hydrostatic bounce" occurs. Second, our EOS becomes invalid at densities above ≈ 0.1 g cm^{-3}, so we should stop the calculation before such densities are reached. And finally, the main accretion phase that follows the second collapse is difficult to deal with in a Lagrangian scheme because the time steps become extremely short, on the order of hours and less. For this reason, an effective treatment of the further evolution requires a change in method, such as switching to a Eulerian grid or using an implicit scheme. Finally, it should be noted that the exact density at which the hydrostatic bounce occurs depends on the resolution. We have chosen to use 500 shells for all calculations presented here.

We perform simulation runs with initial central densities between 5×10^{-17} and 5×10^{-15} g cm^{-3} and initial radii between 65 and 750 AU. These are very dense and compact objects, which is necessary for them to be gravitationally unstable. The masses are between 0.8 and 10 percent of the solar mass, covering the brown dwarf and some of the sub-brown dwarf mass regime (the deuterium burning limit, conventionally used as the lower bound for brown dwarfs, lies at $\approx$ 1.3 percent of solar mass).

We consider two different initial density structures: One is a simple homogeneous density, which makes for a very unstable setup. The labels of these runs begin with the letter A. The second setup is a hydrostatic, Bonnor-Ebert sphere profile similar to chapter 4, except that this time the mass is larger than the Bonnor-Ebert mass so that the sphere is unstable to gravitational collapse even without any external compression. The labels of these runs begin with the letter B. In addition, we include a one solar mass run with initial conditions identical to Masunaga & Inutsuka (2000) for comparison (run C0), as well as a number of runs to test for first core-less collapses (runs D0 through D3; see section 5.5.5). A complete overview of all the runs is given in Table 5.3.

5.4 Spurious Re-Expansion after Second Core Formation

When we were testing our program, we encountered an unexpected behavior: After the formation of the second core, the system expanded again to first core densities and below. Suspecting a numerical error, we analyzed the development of the total energy, shown in Figure 5.2's upper panel. In this plot, the formation of the first core takes place around timestep 5000, and that of

Run	Profile	ρ_{C} (g cm^{-3})	$R_{\mathrm{O}}(AU)$	$M(M_{\odot})$	$\frac{M}{M_{\mathrm{BE}}}$	$t_{\mathrm{ff}}(yr)$	$t_{\mathrm{FC}}(yr)$	$\tau_{\mathrm{FC}}(yr)$	ρ_{fin} (g cm^{-3})
A0	Hom	5×10^{-15}	58	7×10^{-3}	2.4	9.42×10^{2}	1.22×10^{3}	1.49×10^{4}	1.44×10^{-2}
A1	Hom	1×10^{-15}	104	8×10^{-3}	1.24	2.11×10^{3}	3.06×10^{3}	6.81×10^{3}	1.29×10^{-2}
A2	Hom	1×10^{-15}	112	1.0×10^{-2}	1.54	2.11×10^{3}	2.67×10^{3}	3.87×10^{3}	8.09×10^{-3}
A3	Hom	1×10^{-15}	119	1.2×10^{-2}	1.85	2.11×10^{3}	2.52×10^{3}	3.96×10^{3}	7.24×10^{-3}
A4	Hom	1×10^{-15}	129	1.5×10^{-2}	2.36	2.11×10^{3}	2.36×10^{3}	2.27×10^{3}	8.17×10^{-3}
A5	Hom	5×10^{-16}	181	2.1×10^{-2}	2.30	2.98×10^{3}	3.25×10^{3}	9.04×10^{2}	4.59×10^{-3}
A6	Hom	5×10^{-17}	463	3.5×10^{-2}	1.22	9.42×10^{3}	1.04×10^{4}	9.91×10^{2}	7.33×10^{-3}
A7	Hom	5×10^{-17}	548	5.8×10^{-2}	2.02	9.42×10^{3}	9.56×10^{3}	6.38×10^{2}	5.83×10^{-3}
A8	Hom	5×10^{-17}	586	7.1×10^{-2}	2.47	9.42×10^{3}	9.44×10^{3}	5.45×10^{2}	5.83×10^{-3}
A9	Hom	5×10^{-17}	622	8.5×10^{-2}	2.95	9.42×10^{3}	9.36×10^{3}	4.59×10^{2}	6.56×10^{-3}
A10	Hom	5×10^{-17}	659	1.0×10^{-1}	3.51	9.42×10^{3}	9.33×10^{3}	3.64×10^{2}	6.58×10^{-3}
B0	BE	5×10^{-15}	65	7×10^{-3}	1.93	1.10×10^{3}	1.54×10^{3}	1.09×10^{4}	1.28×10^{-2}
B1	BE	1×10^{-15}	110	8×10^{-3}	1.04	2.31×10^{3}	3.83×10^{3}	1.45×10^{4}	1.02×10^{-2}
B2	BE	1×10^{-15}	120	1.0×10^{-2}	1.28	2.35×10^{3}	3.31×10^{3}	4.78×10^{3}	9.14×10^{-3}
B3	BE	1×10^{-15}	130	1.2×10^{-2}	1.53	2.39×10^{3}	3.07×10^{3}	2.58×10^{3}	9.16×10^{-3}
B4	BE	1×10^{-15}	140	1.5×10^{-2}	1.79	2.43×10^{3}	2.93×10^{3}	2.07×10^{3}	1.15×10^{-2}
B5	BE	5×10^{-16}	200	2.1×10^{-2}	1.83	3.45×10^{3}	3.92×10^{3}	8.21×10^{2}	6.30×10^{-3}
B6	BE	5×10^{-17}	500	3.5×10^{-2}	1.08	1.04×10^{4}	1.20×10^{4}	1.06×10^{3}	8.97×10^{-3}
B7	BE	5×10^{-17}	600	5.8×10^{-2}	1.64	1.08×10^{4}	1.11×10^{4}	6.95×10^{2}	8.97×10^{-3}
B8	BE	5×10^{-17}	650	7.1×10^{-2}	1.93	1.10×10^{4}	1.10×10^{4}	6.39×10^{2}	6.59×10^{-3}
B9	BE	5×10^{-17}	700	8.5×10^{-2}	2.24	1.12×10^{4}	1.09×10^{4}	5.50×10^{2}	8.23×10^{-3}
B10	BE	5×10^{-17}	750	1.0×10^{-1}	2.55	1.15×10^{4}	1.08×10^{4}	5.67×10^{2}	9.31×10^{-3}
C0	Hom	1.42×10^{-19}	10000	1	1.85	1.77×10^{5}	1.85×10^{5}	9.01×10^{2}	1.33×10^{-2}
D0	Hom	3.28×10^{-19}	6000	0.5	1.41	1.16×10^{5}	1.28×10^{5}	8.78×10^{2}	1.57×10^{-2}
D1	Hom	3.28×10^{-19}	8000	1.18	3.34	1.16×10^{5}	1.28×10^{5}	6.20×10^{2}	1.13×10^{-2}
D2	Hom	3.28×10^{-19}	11000	3.08	8.68	1.16×10^{5}	-	-	3.77×10^{-3}
D3	Hom	3.28×10^{-19}	12000	4	11.27	1.16×10^{5}	-	-	3.80×10^{-3}

Table 5.1: Overview of our simulation runs. The values are, from left to right: Run label, density profile, central density at the beginning of the simulation, initial radius, mass, ratio of mass to Bonnor-Ebert mass, free-fall time, time until first core formation, first core lifetime, central density at the end of the run. The time of first core formation is defined as the first timestep where the density in the central shell decreases from one time step to the next. The first core lifetime is the time elapsed between that same timestep and the end of the simulation.

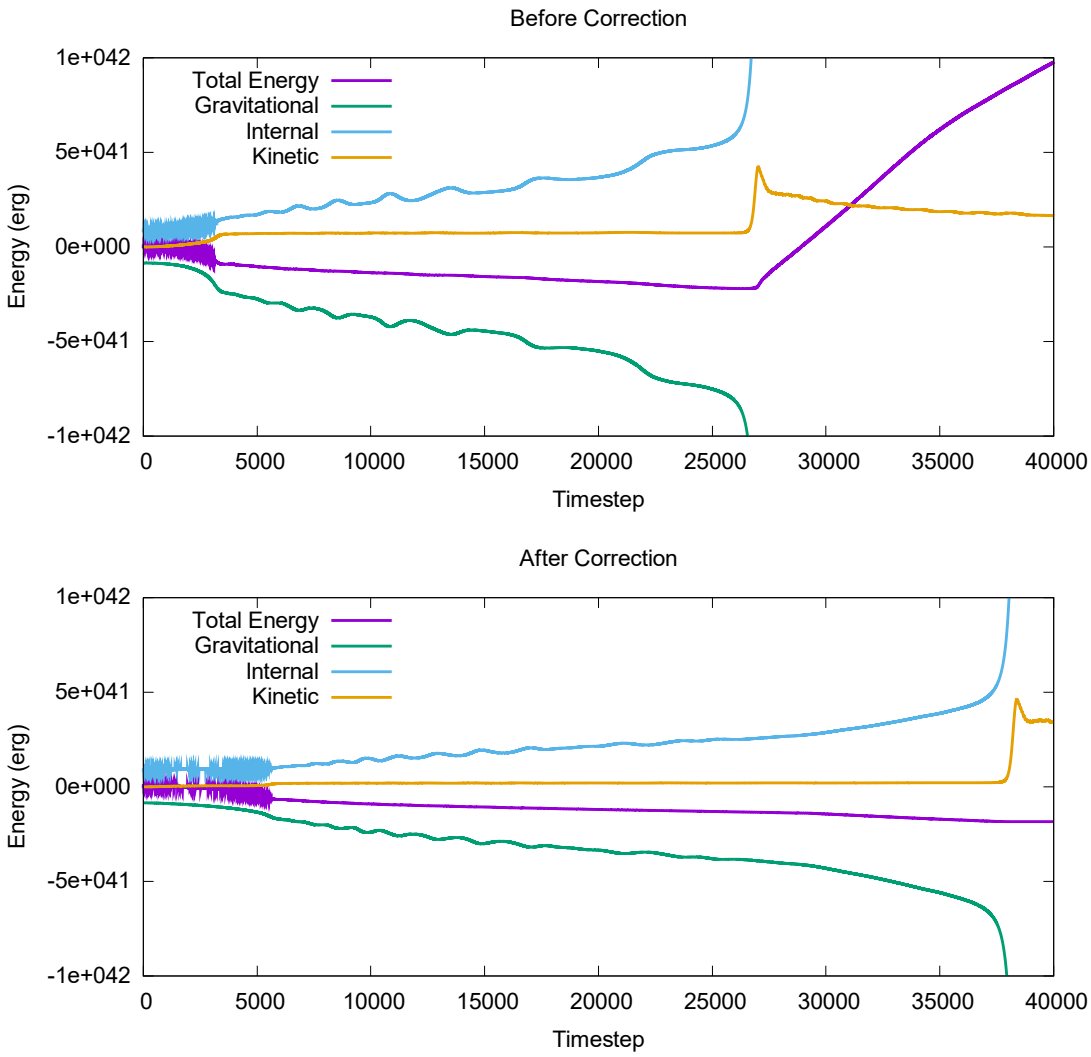

Figure 5.2: Evolution of the system's total energy and its individual constituents in the original calculation (upper panel) and in the corrected version (lower panel). See text for details.

the second core around timestep 27000. In the early phase, the internal energy oscillates rapidly as the system's energetics is dominated by the radiative exchange with the background. The magnitude of these oscillations depends on the size of the timestep. During the first core phase, we see a different kind of oscillation in the internal and gravitational energy. This is because the first core periodically expands and contracts slightly. During this time, the total energy slowly decreases due to radiation escaping from the system. The problem becomes apparent at the formation of the second core, when the total energy starts to increase steeply. This is obviously unphysical, since at this stage, radiative cooling should far exceed radiative and cosmic ray heating, and there are no other diabatic processes. In fact, this spurious increase occurred even when completely deactivating radiation and cosmic rays, implying that the cause is in the hydrodynamics module.

We found that the term $-v\nabla\Phi$ in equation 4.3 (the energy equation) was responsible for this error. This term represents the energy gained or lost by the fluid due to gravity. Colella & Woodward (1984) include a non-specified "external body force" g in their scheme, in which case the numerical implementation of the resulting term vg is an average of the value before the current timestep and the value after the timestep, i.e. $(v^n g^n + v^{n+1} g^{n+1})/2$. This is only an approximation and hence not perfectly conservative. In our self-gravitating system, where g is calculated from the enclosed mass, this inaccuracy leads to a continuous increase in the total energy of the system. In other words, the increase in the internal energy in each time step is larger than the corresponding decrease in gravitational potential energy. In the early stages of the collapse and during the first core phase, the effects of this error are too small to counteract the radiative losses, but during second core formation much more gravitational energy is converted to internal energy, and the abnormally large increase in pressure ultimately blows apart the second core.

We have solved this problem by explicitly calculating the gravitational energy in each shell before and after the time step, and inserting the difference in the energy equation in place of the term $-v\nabla\Phi$. The gravitational potential energy of any shell is given by

$$E_{\mathrm{grav}} = -4\pi G \int_{m_{\mathrm{I}}}^{m_{\mathrm{O}}} \frac{m}{r(m)} dm, \tag{5.1}$$

where m is equal to the enclosed mass divided by 4π. m_{I} and m_{O} are the values of this mass coordinate at the inner and outer boundary of the shell. Expressing the radial coordinate r as a function of m, we obtain

$$E_{\mathrm{grav}} = -4\pi G \int_{m_{\mathrm{I}}}^{m_{\mathrm{O}}} \frac{m}{\left(3\frac{m-m_{\mathrm{L}}}{\rho} + r_{\mathrm{I}}^3\right)^{1/3}} dm. \tag{5.2}$$

The integral in the above equation can be solved analytically:

$$\begin{aligned} &\int \frac{m}{\left(3\frac{m-m_{\mathrm{L}}}{\rho} + r_{\mathrm{I}}^3\right)^{1/3}} dm \\ &= \frac{1}{10}\rho\left(3m_{\mathrm{L}} - \rho r_{\mathrm{L}}^3 + 2m\right)\left(\frac{-3m_{\mathrm{L}} + \rho r_{\mathrm{L}}^3 + 3m}{\rho}\right)^{2/3} + C. \end{aligned} \tag{5.3}$$

Since all necessary values are known both before and after the timestep, the change in gravitational energy can be calculated and inserted into the energy equation.

The lower panel of Figure 5.2 shows the behavior after applying this correction. The main difference is that there is no longer any increase in total energy at the point of second core formation, which here occurs around timestep 37000. In addition, the oscillations during the first core phase are significantly smaller.

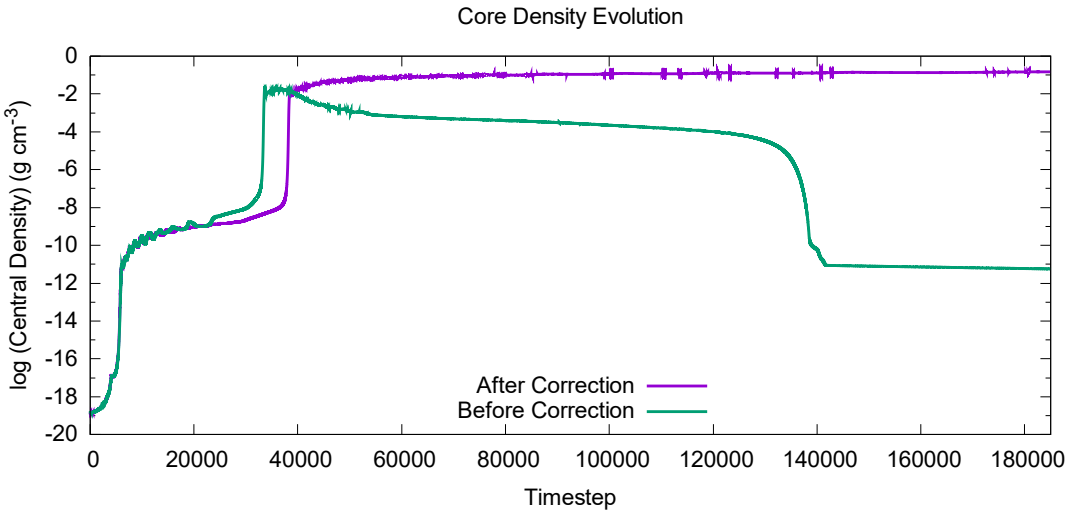

Figure 5.3: Evolution of the central density in the original calculation and in the corrected version. Only the former shows the unexpected re-expansion and destruction of the second core.

Figure 5.3 shows the evolution of the central density before and after the correction. In the improved version, the second core is stable and no unphysical re-expansion occurs.

5.5 Results

5.5.1 Core Evolution

Figure 5.4 shows the evolution in the temperature-density plane of a fluid element near the center of the system (Run C0). It generally behaves as expected (see Figures 1.3 and 5.1), with a near-isothermal phase until $\approx 10^{-12}$ g cm^{-3}, followed by an adiabatic phase until $\approx 10^{-8}$ g cm^{-3} and the second collapse until $\approx 10^{-3}$ g cm^{-3}, when hydrogen molecule dissociation is complete and the equation of state again becomes stiffer.

It is noteworthy, however, that the initial contraction is not completely isothermal. Instead, the temperature drops from the initial value of ≈ 10 K to a minimum of ≈ 6 K before increasing again. This effect is only captured in frequency-dependent radiative transfer calculations such as this work or Masunaga & Inutsuka (2000), but not in gray cases such as Vaytet & Haugbølle (2017) and Tomida et al. (2010). The cause is due to the increased opacity for radiation from the outside: As the cloud core starts to contract, its optical thickness begins to increase. Since the opacity is generally larger at higher frequencies, the system first becomes optically thick to high-frequency photons while still remaining optically thin to low frequencies. The inner regions are thus shielded from the background stellar radiation, so that heating is supplied only by cosmic rays and the CMB, but the cooling radiation emitted from the dust can still escape.

5.5.2 Radial Profiles

The evolution of run C0's radial profiles of density, temperature and velocity is plotted in Figure 5.5. The formation of the first and second cores at $\approx 10^{1}$ and $\leq 10^{-2}$ AU, respectively, is evident as a sudden increase in density and temperature and as a maximum in the infall velocity (accretion shock). Snapshot 2 also shows the initial temperature decrease mentioned in the previous section, and it can be seen that this decrease affects the whole inner region of the cloud core, but not the outermost regions.

The final radial profiles (Figure 5.6) show that the second core's properties (density, radius) are essentially independent of the initial conditions. They are all very similar irrespective of the

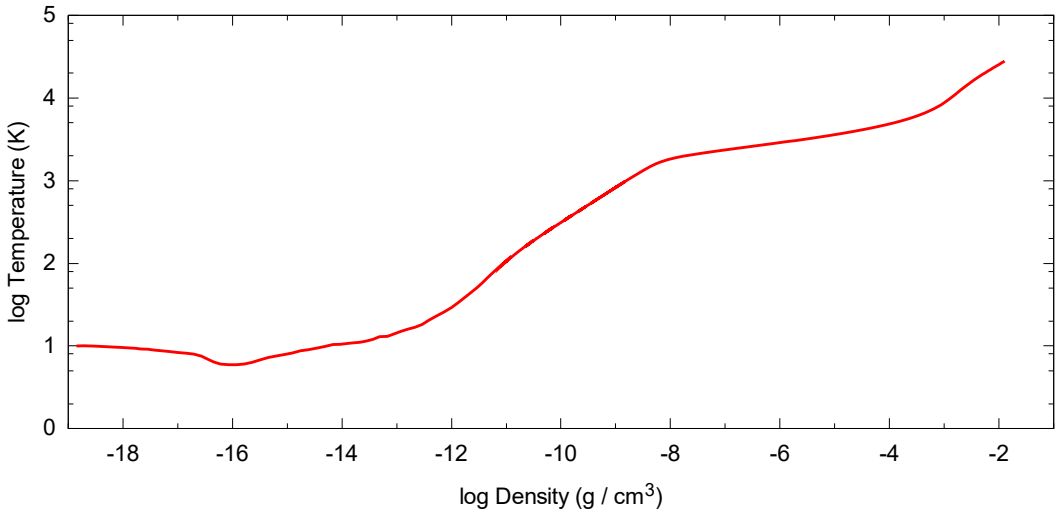

Figure 5.4: Evolution in the temperature-density plane at the center of the collapsing cloud core for run C0.

cloud core mass, initial density and density structure. This agrees with the results of Vaytet & Haugbølle (2017) for higher masses, but here we show that it holds true in the brown dwarf regime as well.

However, we do find significant differences in the first core. Specifically, the very low mass runs A0 - A4 and B0 - B4 look qualitatively different, with a very small first core (< 1 AU) which essentially makes up the whole system. The unusual behavior of these runs is closely related to the question of first core lifetime and will be discussed in the following section.

5.5.3 First Core Lifetimes

The first hydrostatic core is generally believed to be a very short-lived object, which combined with the low luminosity should make it very hard to observe. Nevertheless, in recent years a number of candidate objects have been found, for example by Pineda et al. (2011), Dunham et al. (2011), Chen et al. (2010) and Chen & Arce (2010). This may indicate that first cores are more long-lived and therefore more common than typically believed. Tomida et al. (2010) investigated first core lifetimes using 3D RHD simulations and found that for low mass cores ($< 0.1 M_\odot$), the lifetime can be in excess of 10^4 years. The reason for this is that for the second collapse to start, the first core must reach a critical temperature of about 2000 K. How quickly that temperature is reached depends on the mass accretion rate. However, in a very low-mass case the mass reservoir may essentially be used up so that the accretion onto the first core becomes very weak before the temperature has risen sufficiently. This is what we see in the radial profiles of the very low mass runs A0 - A4 and B0 - B4 (Figure 5.6): The first core basically makes up the whole system. In this situation, radiative cooling then plays a crucial role in removing entropy from the system and thus allowing further contraction and heating in a Kelvin-Helmholtz-like process on a much slower timescale.

As shown in table 5.3, our calculations confirm that the first core lifetime rises drastically for these very low-mass runs, when it becomes comparable to or even much larger than the free-fall time. However, this only becomes evident below about $0.02 M_\odot$, not $0.1 M_\odot$ as suggested by Tomida et al. (2010), and a lifetime of 10^4 years is only reached in the sub-brown dwarf regime. This is likely to be due to differences in the numerical method: As a 3-D calculation, Tomida et al. (2010) include the effect of rotation, but on the other hand they use an idealized EOS with $\gamma = 5/3$ and a much more simplified radiative transfer scheme (gray flux-limited diffusion approximation). Vaytet & Haugbølle (2017) find an anticorrelation of the first core

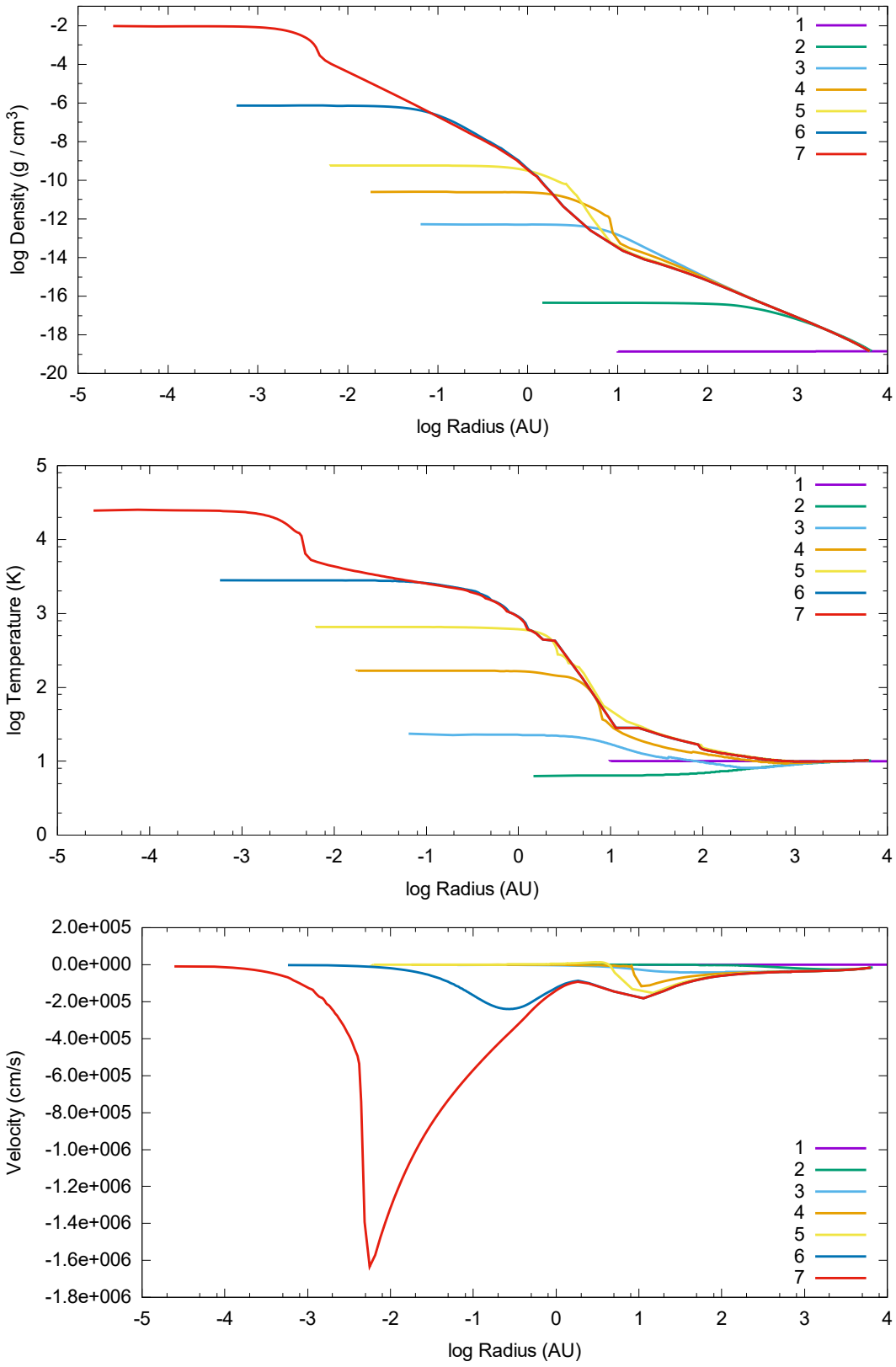

Figure 5.5: Evolution of the radial profiles of density, temperature and velocity for run C0. 7 snapshots are shown, numbered sequentially after their elapsed time.

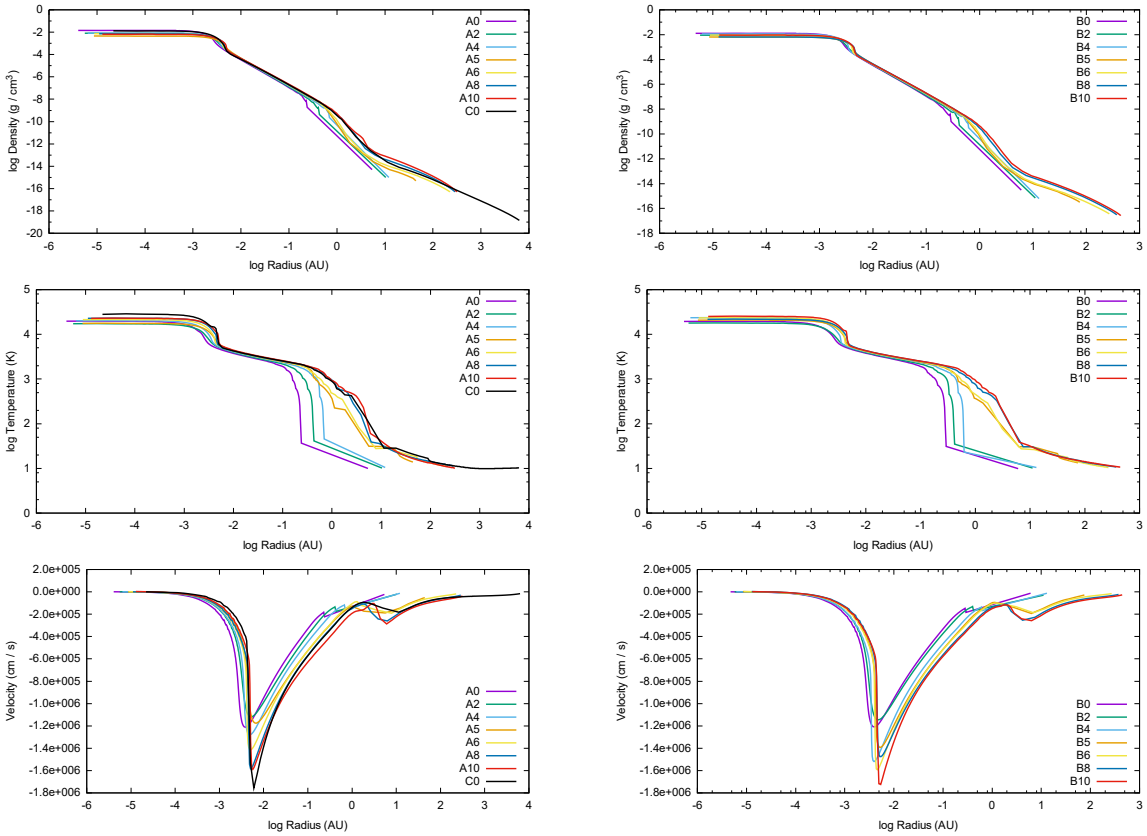

Figure 5.6: Density, temperature and velocity profiles at the end of the simulation for various runs. The left side shows runs with an initially homogeneous density profile, while the right side shows initially Bonnor-Ebert profiles.

lifetime with an instability parameter given by the ratio of mass to Bonnor-Ebert mass [1], where the lifetime drops at first slowly and then significantly for very large ratios of $M/M_{\rm BE} >\approx 5$. However, the lowest mass they consider is 0.2 $M_\odot$, so they do not probe the very low mass regime, where the behavior is different. Figure 5.7 shows that for the very low-mass end, the first core lifetime depends strongly on the mass of the cloud core rather than on the instability parameter.

In conclusion, despite the quantitative differences with Tomida et al. (2010), our results confirm their prediction that very low-mass first cores can be very long-lived due to exhaustion of the accretion reservoir, and that generally the behavior of the first core lifetime is qualitatively different from higher mass ranges. This may account for the surprisingly large number of observational candidates. Furthermore, we predict that future discoveries of first cores will show a bias towards low mass objects due to their longer lifetimes.

5.5.4 Spectral Energy Distribution

We discuss the observational signature that would be expected from a brown dwarf in the process of formation. Since our simulations allow us to calculate the radiation escaping from the system at any point in time, we may use this to compute the spectral energy distribution (SED) that would be observed (Figure 5.8). We note that for a typical case, in this case the run B10, the emission is dominated by the cold envelope at all stages, i.e. the hot core region is obscured. This is also the main reason why observation of the early phases of star formation is difficult. The situation is exacerbated in the case of brown dwarfs because of their even lower luminosity compared to solar-type stars. A smaller beamsize helps to better distinguish

[1]Note that Vaytet & Haugbølle (2017) originally define a stability parameter $\epsilon = M_{\rm BE}/M_0$ in their method section, but later write $\epsilon = M_0/M_{\rm BE}$ at various points, which requires special care in interpreting their findings.

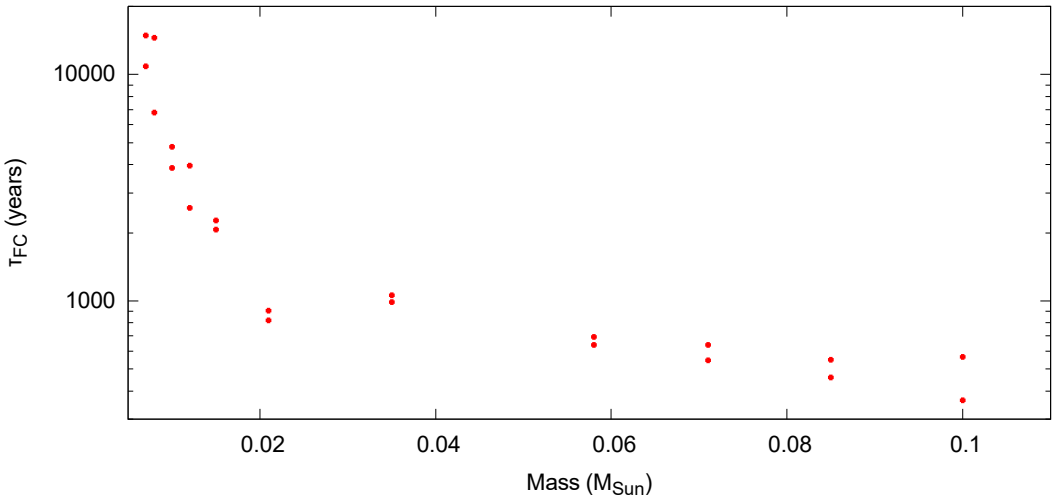

Figure 5.7: Correlation of the first core lifetime $\tau_{\rm FC}$ with the mass. While there is little effect at masses larger than about $10^{-2} M_\odot$, a very significant increase in the lifetime can be observed at extremely low masses.

different stages of the collapse, since the effect of the contribution of the envelope is reduced. These results essentially confirm those of Masunaga, Miyama, & Inutsuka (1998) and Masunaga & Inutsuka (2000), although the latter also found that the SED becomes markedly different in the following main accretion phase, which we have not considered.

The situation is somewhat different for the very low-mass cases, as seen in the lowest panel of Figure 5.8. Here, the surrounding envelope has disappeared in the later stages, allowing the observer to look deeper into the warm interior. Therefore the SED is clearly warmer than at the beginning, and this effect may make very low-mass protostars easier to observe, further increasing the observational bias towards such objects that already exists due to the longer first core lifetimes (see section 5.5.3).

5.5.5 Collapses Without First Cores

Vaytet & Haugbølle (2017) found that for certain very unstable setups ($M/M_{\rm BE} >\approx 10$), the collapse can proceed without the formation of a first core. This occurs because the vigorous collapse creates such a high ram pressure that the thermal pressure does not become strong enough to balance it before the temperature reaches 2000 K and thus directly proceeds to the second collapse.

We confirm this behavior in our runs D0 through D3 (Figure 5.9). The initial conditions of D3 are identical to the ones Vaytet & Haugbølle (2017) used to investigate this phenomenon. The other three runs differ from D3 only in that their initial radii are smaller, which also implies a smaller mass and a smaller degree of instability. Figure 5.9 shows the transition between the cases with and without the first core. The first core's signature in the density profile, clearly visible at around 10 AU in runs D0 and D1, is absent in runs D2 and D3. The lower panel of Figure 5.9 confirms the importance of the ratio between thermal and ram pressure. In the first core-less cases, this ratio is smaller than unity everywhere outside the second core. The most favorable conditions for skipping the first core phase are those in which the ram pressure is very large (high degree of instability leading to large infall velocity), while the thermal pressure is relatively low. With respect to the initial temperature of the cloud, there is one difference between our result and Vaytet & Haugbølle (2017): They report that a collapse without the first core occurs only for an initial temperature of 5 K, but not for higher values such as 10 K or above, although our calculations show that it occurs even with 10 K. The boundary condition for all of our runs is calibrated such as to keep the initial temperature at 10 K, but

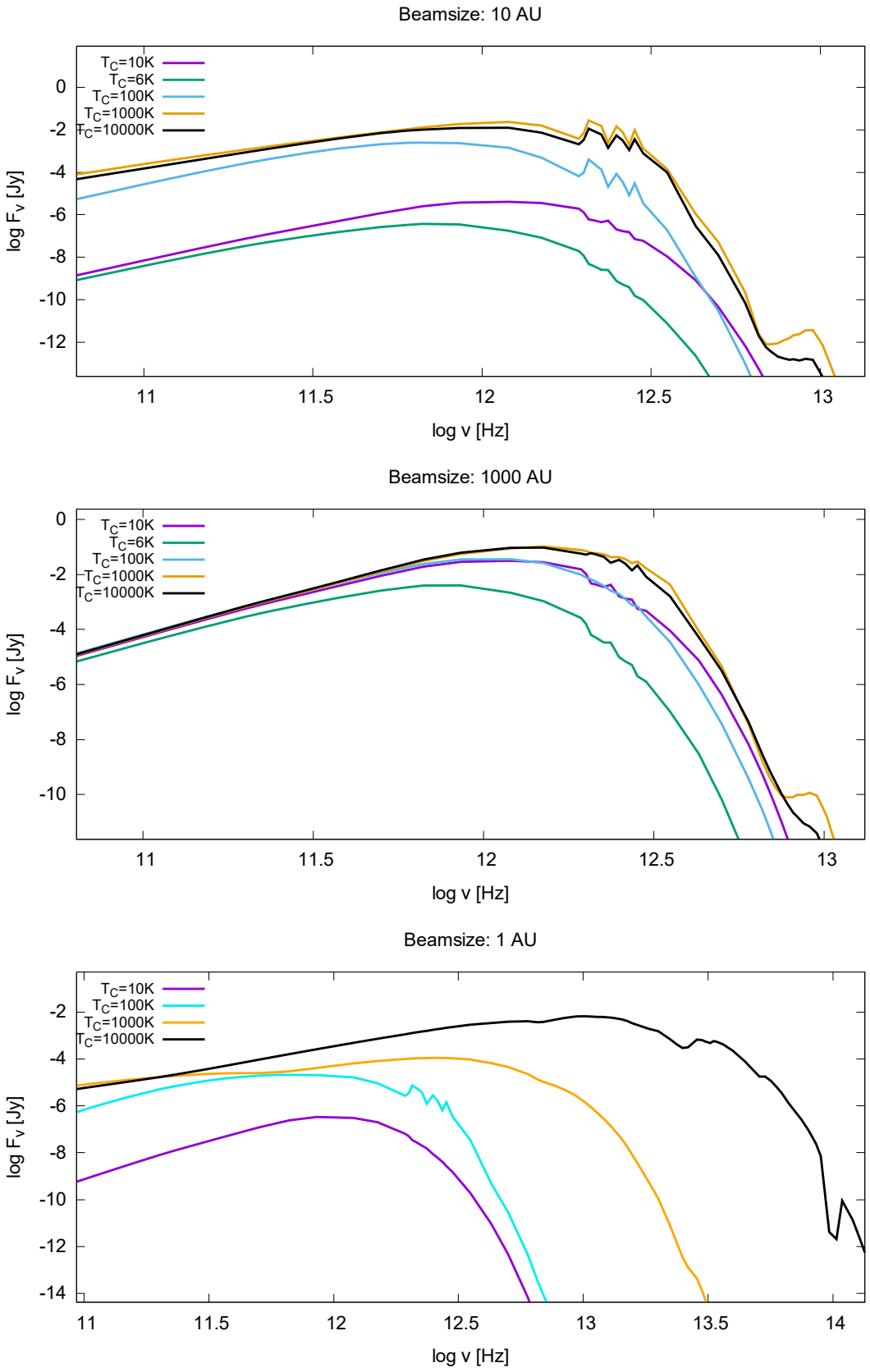

Figure 5.8: Spectral energy distribution at various timesteps for run B10 (upper two panels) and run B0 (lowest panel), at an assumed distance of 150 *pc* and with different beamsizes. The 6K-plot is missing in the lower panel since run B0 never reached such low core temperatures. The evolution becomes clearer with smaller beamsizes, and is especially visible for the very low-mass cases where the obscuring envelope has disappeared.

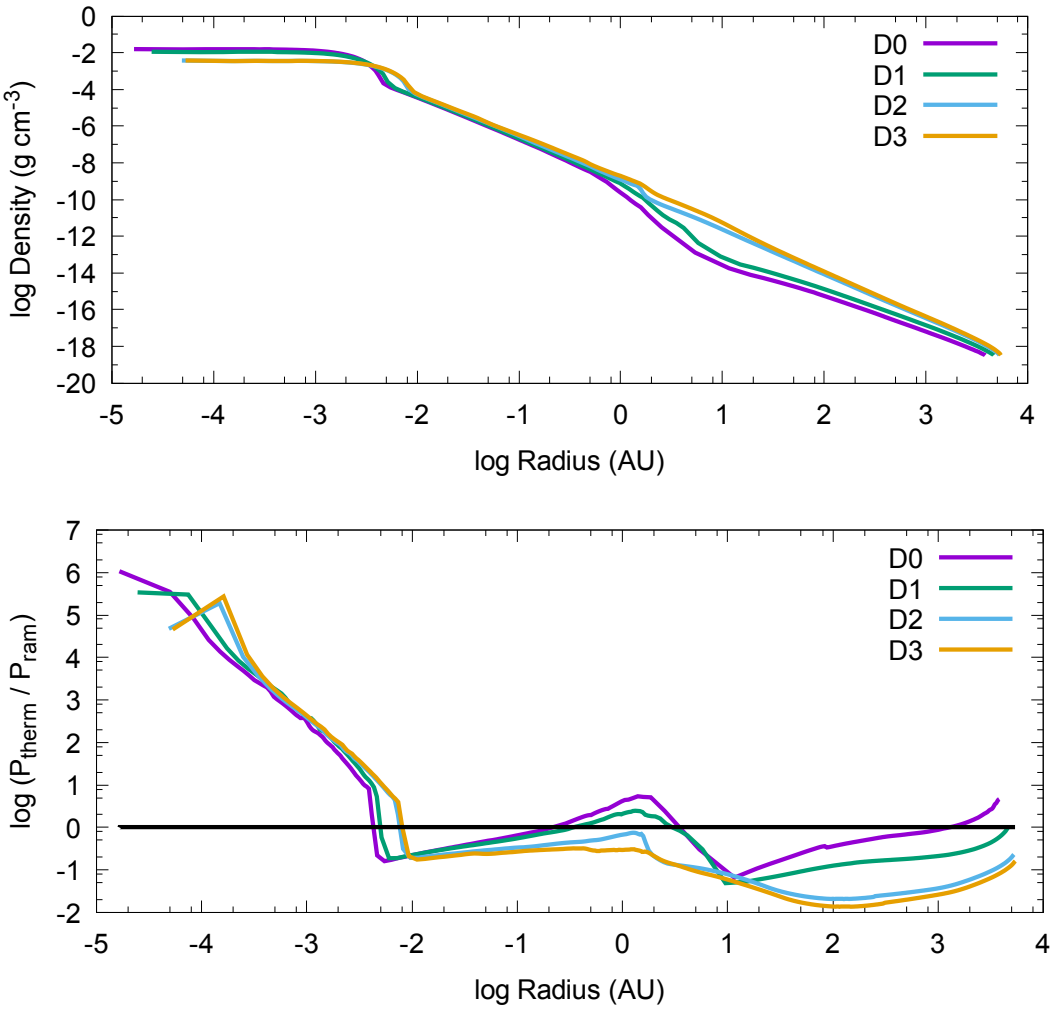

Figure 5.9: *Upper panel*: Final density profiles for runs D0 through D4, showing the transition to a collapse without the first core phase. *Lower panel*: Ratio of thermal to ram pressure at the end of the simulation for the same four runs.

the frequency-dependent radiative transfer then causes a decrease to ≈ 6 K (see section 5.5.1), so that the first core phase can be skipped despite the relatively high initial temperature. This example illustrates that, even though in most cases the overall behavior of gray and frequency-dependent calculations is similar, in certain cases such as this they may produce significantly different results. In summary, the unique condition for the formation of a protostar without the first core phase is that the initial core mass must be much larger than the Bonnor-Ebert mass.

Chapter 6

Summary and Future Work

In this thesis, we have developed a new numerical method of calculating the radiative transfer in spherically symmetric systems. This method avoids the use of any kind of diffusion approximation and is therefore applicable in optically thick, thin, and intermediate systems. It is also very fast, especially if the approximation of a homogeneous extinction coefficient is used. This method can be combined with a slower one which is also accurate for inhomogeneous cases. By determining correction factors between the results of the two methods and applying them to the fast method, a compromise between speed and accuracy can be achieved. The performance depends strongly on the system that is being investigated, particularly on the optical depth structure and its rate of change, which determines which computationally intensive terms in the equations can be neglected.

Using our newly developed numerical scheme, we performed simulations of brown dwarf formation by turbulent compression. A longstanding problem in the question of brown dwarf formation is the fact that very low mass cloud cores need very high densities in order to become gravitationally unstable according to the Jeans criterion. One possibility to achieve these densities is by compressing the cloud core with an external pressure, and the turbulence which is known to exist in molecular clouds is a possible source of such a pressure. However, the results of our simulations showed that, assuming typical molecular cloud conditions, brown dwarf formation requires very large (thousands of AU) coherent regions of high turbulent pressure. We conclude that this mechanism is unlikely to play a dominant role in brown dwarf formation, although if such large-scale high pressure regions exist, it should be possible to observe them.

In the next step, we expanded our simulation program to include a realistic equation of state to account for the effect of hydrogen dissociation, which plays a crucial role in the second collapse phase of star formation. We also included molecular and atomic opacities which become important at the higher temperatures encountered in this part of the process. We then performed simulation runs of the complete protostellar collapse process, beginning with a molecular cloud core and ending with the formation of a second core a.k.a. protostar. When we were exploring numerical results with various initial conditions, we noticed a numerical problem with the hydrodynamics code that may be relevant to other investigations of self-similar gravitational collapse processes. To our knowledge, the solution for the problem has not been mentioned in the literature. Specifically, we found that in this self-gravitating system, a violation of energy conservation occurs if the effect of gravity in the energy equation is calculated according to the method of Colella & Woodward (1984). Over time, this causes a spurious increase in the total energy, which in certain cases can blow the whole system apart due to the increased pressure. We provide a method to overcome this problem by explicitly calculating the gravitational energy in each shell before and after each timestep.

We found that for a typical case of 1 solar mass, our results agree with those of previous work, and that for brown dwarfs and sub-brown dwarfs, the mass and size of the protostar directly

after its formation are essentially independent of the initial conditions. This had already been found by previous research for higher masses, but we confirmed that it is still the case even in the very low-mass regime. We also found that for extremely low masses below about 0.02 $M_\odot$, the collapse process becomes qualitatively different. While the final result - the protostar - still shows basically the same properties as in other cases, the first core's lifetime becomes extremely long, exceeding 10,000 years. This occurs because for sufficiently low masses, the accretion reservoir becomes exhausted so that accretion onto the first core essentially stops before the temperature has reached the 2000 K necessary to trigger the second collapse. The object then slowly contracts due to radiative cooling in a Kelvin-Helmholtz process, which explains the much longer timescale. This behavior has previously been shown by other simulations, but quantitatively our results are quite different, which is probably a result of different numerical methods. These longer first core lifetimes may in part explain the surprisingly large number of first core candidates observed so far, and we also suggest that it may cause an observational bias towards very low-mass objects. We also calculated spectral energy distributions, which show that in cases where the surrounding envelope has disappeared, a warmer SED emerges from the object. This would make such objects easier to observe and thus add to this observational bias.

Finally, we investigated the phenomenon of collapses entirely without a first core phase. We confirmed that for sufficiently unstable initial conditions, the first core phase can indeed be skipped. Contrary to previous research, we found that this is not dependent on the initial cloud core being very cold. Because of our frequency-dependent radiative transfer and realistic boundary condition, the temperature near the center always becomes very cold even if the initial cloud was relatively warm. For future work, we are considering a number of possible projects:

- Further development of the radiative transfer scheme. As mentioned in section 3.3, there are still a number of possible improvements that may increase the speed and/or accuracy of the method.
- Including the main accretion phase. This phase follows the formation of the second core, at which point our simulations currently end. Numerically, it is problematic since the timesteps become extremely short. This can be solved by using an implicit scheme or by switching to a Eulerian grid at this stage.
- Larger variety of initial conditions for protostellar collapse calculations. Since our scheme is so fast, it is well suited to perform a large number of runs in order to investigate the parameter space.
- Application of the radiative transfer scheme to other physical processes. It is not limited to star formation, but can in principle be used wherever a system can be treated as spherically symmetric. Possible applications include the effect of radiation in massive stars or the formation of giant planets within a protoplanetary disk.

Bibliography

André, P., Men'shchikov, A., Bontemps, S., Könyves, V., Motte, F., Schneider, N., ... & Di Francesco, J. 2010, A&A, 518, L102

André, P., Di Francesco, J., Ward-Thompson, D., Inutsuka, S. I., Pudritz, R. E., & Pineda, J. E. 2014. Protostars and Planets VI, 27-51

Badnell, N. R., Bautista, M. A., Butler, K., Delahaye, F., Mendoza, C., Palmeri, P., ... & Seaton, M. J. (2005). MNRAS, 360(2), 458-464

Bate, M. R. 2008, MNRAS, 392(2), 590-616

Bate, M. R., Tricco, T. S., & Price, D. J., 2014, MNRAS, 437, 77

Bodenheimer, P., Yorke, H. W., Rozyczka, M., & Tohline, J. E. 1990, ApJ, 355, 651-660

Bonnor, W. B. 1956, MNRAS, 116(3), 351-359

Bontemps, S., André, P., Könyves, V., Men'Shchikov, A., Schneider, N., Maury, A., ... & Minier, V. 2010, A&A, 518, L85

Buchler, J. R. 1979, J. Quant. Spectrosc. Radiat. Transfer, 22(3), 293-300

Burgasser, A. J. (2008). Physics Today, 61(6), 70

Castor, J. I. 1972, ApJ, 178, 779-792

Chabrier, G. 2005, in The Initial Mass Function 50 Years Later, 41-50

Chen, X., Arce, H. G., Zhang, Q., Bourke, T. L., Launhardt, R., Schmalzl, M., & Henning, T. (2010). ApJ, 715(2), 1344

Chen, X., & Arce, H. G. (2010). ApJ Letters, 720(2), L169

Colella, P., & Woodward, P. R. 1984, J. Comput. Phys., 54(1), 174-201

Commerçon, B., Hennebelle, P., Audit, E., Chabrier, G., Teyssier, R. 2010, A&A,510, L3

Commerçon, B., Launhardt, R., Dullemond, C., Henning, T. 2012a, A&A, 545,A98

Dunham, M. M., Chen, X., Arce, H. G., Bourke, T. L., Schnee, S., & Enoch, M. L. (2011). ApJ, 742(1), 1

Dzyurkevich, N., Commerçon, B., Lesaffre, P., & Semenov, D. 2016, arXiv:1605.08032

Ebert, R. 1955, Zeitschrift fur Astrophysik, 37, 217

Federrath, C., Schrön, M., Banerjee, R., Klessen, R., 2014, ApJ, 790, 128

Federrath, C. 2015, MNRAS, 450, 4035

Ferguson, J. W., Alexander, D. R., Allard, F., Barman, T., Bodnarik, J. G., Hauschildt, P. H., ... & Tamanai, A. (2005). ApJ, 623(1), 585

Ford, E. B., & Rasio, F. A. (2008). ApJ, 686(1), 621

Frimann, S., Jørgensen, J., Haugbølle, T. 2016a, A&A, 587, A59

Goldsmith, P. F., & Langer, W. D. (1978). ApJ, 222, 881-895

González, M., Vaytet, N., Commerçon, B., Masson, J. 2015, A&A, 578, A12

Hennebelle, P., & Charbonnel, C. 2013, EAS Publications Series, 62

Hennebelle, P. (2013). A & A, 556, A153

Hincelin, U., Commerçon, B., Wakelam, V., et al. 2016, ApJ, 822, 12

Hopkins, P. F., & Lee, H. 2016, MNRAS, 456, 4174

Hummer, D. G., & Rybicki, G. B. 1971, MNRAS, 152(1), 1-19

Inutsuka, S. I., & Miyama, S. M. 1992, ApJ, 388, 392-399

Inutsuka, S. I., & Miyama, S. M. 1997, ApJ, 480(2), 681

Inutsuka, S. I. 2001, The Astrophysical Journal Letters, 559(2), L149

Inutsuka, S. I. 2012, Progress of Theoretical and Experimental Physics, 2012(1)

Inutsuka, S. I., Machida, M. N., & Matsumoto, T. 2010, ApJL, 718, L58

Jeffries, R. D. 2012, European Astronomical Society Publications Series, 57, 45-89

Joergens, V. 2006, A&A, 446(3), 1165-1176

Könyves, V., André, P., Men'Shchikov, A., Schneider, N., Arzoumanian, D., Bontemps, S., ... & Abergel, A. 2010, A&A, 518, L106

Kramer, C., Stutzki, J., Rohrig, R., & Corneliussen, U. 1998, A&A, 329, 249-264

Kroupa, P. 2001, MNRAS, 322(2), 231-246

Krumholz, M. R., Klein, R. I., & McKee, C. F. 2012, ApJ, 754, 71

Kunitomo, M., Guillot, T., Takeuchi, T., & Ida, S. 2017, A&A 599, A49

Kurosawa, R., Harries, T. J., & Littlefair, S. P. 2006, MNRAS, 372(4), 1879-1887

Larson, R. B. 1969, MNRAS, 145, 271

Li, S., Frank, A., & Blackman, E. G. 2014, MNRAS, 444, 2884

Li, H.-B., Yuen, K., Otto, F., et al., 2015, Nature, 520, 518

Lomax, O., Whitworth, A. P., & Hubber, D. A. 2016, MNRAS, 458(2), 1242-1252

Ma, B., & Ge, J. (2014). MNRAS, 439(3), 2781-2789

Machida, M. N., Omukai, K., Matsumoto, T., & Inutsuka, S. I. 2006, ApJL, 647, L1

Machida, M. N., Inutsuka, S. I., & Matsumoto, T. 2011, PASJ, 63, 555

Masson, J., Chabrier, G., Hennebelle, P., Vaytet, N., Commerçon, B. 2016, A&A, 587, A32

Masunaga, H., Miyama, S., Inutsuka, S. I. 1998, ApJ, 495, 346

Masunaga, H., & Inutsuka, S. I. 2000, ApJ, 531(1), 350

Matsumoto, T., Dobashi, K., & Shimoikura, T. 2015, ApJ, 801, 77

Mihalas, D., & Mihalas, B. W. 1984, Foundations of Radiation Hydrodynamics (New York: Oxford Univ. Press)

Myers, P. C. 2009, ApJ, 700(2), 1609

Myers, P. C. 2011, ApJ, 735(2), 82

Nordlund, Å., Haugbølle, T., Küffmeier, M., et al. 2014, IAU Symposium, 299, 131

Padoan, P., Juvela, M., Goodman, A. A., & Nordlund, Å. 2001, ApJ, 553(1), 227

Padoan, P., Haugbølle, T., & Nordlund, Å. 2014, ApJ, 797, 32

Pineda, J. E., Arce, H. G., Schnee, S., Goodman, A. A., Bourke, T., Foster, J. B., ... & Caselli, P. (2011). ApJ, 743(2), 201

Pudritz, R. E., & Kevlahan, N. R. 2013, Phil. Trans. R. Soc. A, 371(2003), 20120248

Reipurth, B., & Clarke, C. 2001, AJ, 122(1), 432

Roy, A., André, P., Arzoumanian, D., Peretto, N., Palmeirim, P., Könyves, V., ... & Hill, T. (2015). A&A, 584, A111

Schneider, N. E. A., Csengeri, T., Hennemann, M., Motte, F., Didelon, P., Federrath, C., ... & André, P. 2012, A&A, 540, L11

Semenov, D., Henning, T., Helling, C., Ilgner, M., & Sedlmayr, E. (2003). A&A, 410(2), 611-621

Stahler, S. W., & Palla, F. 2008. *The formation of stars*. John Wiley & Sons

Stamatellos, D., Hubber, D. A., & Whitworth, A. P. 2007, MNRAS: Letters, 382(1), L30-L34

Stamatellos, D., & Whitworth, A. P. (2008). MNRAS, 392(1), 413-427

Seifried, D., Banerjee, R., Pudritz, R. E., & Klessen, R. S. 2012, MNRAS, 423, L40

Seifried, D., Sánchez-Monge, Á.,Walch, S., & Banerjee, R. 2016, MNRAS, 459, 1892

Spiegel, E. A. 1957, ApJ, 126, 202

Stamer, T., & Inutsuka, S. I. (2018). arXiv preprint arXiv:1804.08988.

Stone, J. M., Mihalas, D., & Norman, M. L. 1992, ApJ Supplement Series, 80, 819-845

Tilley, D. A., & Pudritz, R. E. 2004, MNRAS, 353(3), 769-788

Tomida, K., Machida, M. N., Saigo, K., Tomisaka, K., & Matsumoto, T. (2010). ApJ Letters, 725(2), L239

Tomida, K., Tomisaka, K., Matsumoto, T., Hori, Y., Okuzumi, S., Machida, M. N., & Saigo, K. (2012). ApJ, 763(1), 6

Tomida, K., Okuzumi, S., & Machida, M. N. (2015). ApJ, 801(2), 117

Tomisaka, K. 2002, ApJ, 575, 306

Tscharnuter, W. M., & Winkler, K. H. 1979, Computer Physics Communications, 18(2), 171-199

Tsukamoto, Y., Iwasaki, K., Okuzumi, S., Machida, M. N., & Inutsuka, S. I. 2015, MNRAS, 452, 278

Tsukamoto, Y., Iwasaki, K., Okuzumi, S., Machida, M. N., & Inutsuka, S. (2015), ApJL, 810, L26

Vaytet, N., Audit, E., Dubroca, B., & Delahaye, F. 2011, J. Quant. Spectrosc. Radiat. Transfer, 112(8), 1323

Vaytet, N., Audit, E., Chabrier, G., Commerçon, B., & Masson, J. 2012. A&A, 543, A60

Vaytet, N., Chabrier, G., Audit, E., Commerçon, B., Masson, J., Ferguson, J., & Delahaye, F. 2013. A&A, 557, A90

Vaytet, N., & Haugbølle, T. 2017, A&A, 598, A116

Visser, R., Bergin, E., Jørgensen, J. 2015, A&A, 577, A102

Whitworth, A. P., & Zinnecker, H. 2004, A & A, 427(1), 299-306

Winkler, K.-H., & Newman, M. J. 1980, ApJ, 236, 201

Wurster, J., Price, D. J., & Bate, M. R. 2016, MNRAS, 457, 1037

Yorke, H. W., Bodenheimer, P., & Laughlin, G. 1993, ApJ, 411, 274-284